Búsqueda de materia oscura en asociación con pares de quark top en el experimento CMS

Memoria para optar al grado de doctor presentada por

Juan García Ferrero

Bajo la dirección de

Jónatan Piedra Gómez

Pablo Martínez Ruiz del Árbol

Santander, 2018

Search for dark matter in association with top quark pairs in the CMS experiment

A thesis submitted in fulfilment of the requirements for the degree of Doctor of Philosophy by

Juan García Ferrero

Under the supervision of

Jónatan Piedra Gómez

Pablo Martínez Ruiz del Árbol

Santander, 2018

factorem cæli et terræ,
visibilium ominum et invisibilium

Resumen

Ciertas observaciones y medidas comológicas y astrofísicas del último siglo nos permiten afirmar que el Universo ha de contener una componente material insensible a la interacción electromagnética, relativamente abundante, conocida como "materia oscura" ("DM", por sus siglas en inglés). A lo largo del mismo periodo, y con anterioridad, la física ha podido explicar la materia ordinaria y sus fenómenos en términos de partículas elementales, lo que nos induce a pensar que la DM esté formada por otra partícula (o partículas).

Esta tesis consiste en una búsqueda de DM producida en asociación con pares de quark top, $t\bar{t}$, usando una luminosidad integrada de 35.9 ± 0.9 fb^{-1} de colisiones protón-protón en el Gran Colisionador de Hadrones (LHC) y recogidas por el experimento "Compact Muon Solenoid" (CMS), en el Laboratorio Europeo de Partículas (CERN) de Ginebra.

Nuestro modelo de DM propone la interacción de ésta con la materia ordinaria por medio de un partícula de espín cero, similar a la partícula de Higgs, descubierta en 2012, en especial en lo que se refiere a la jerarquía de sus acoplamientos. En efecto, el mayor se daría con el quark top, lo que en parte justifica la búsqueda de DM en asociación con aquél.

El quark top, de otro lado, es el único para el que la interacción débil actúa primero que la fuerte, por lo que se desintegra antes de hadronizar. Cuando hablamos de pares de quark top podemos hacerlo de tres canales de desintegración: hadrónico, semileptónico y dileptónico. Esta búsqueda se ciñe al último de ellos. La motivación es que, pese a que tenga lugar con menor probabilidad, su signatura es relativamente limpia en un colisionador hadrónico,

por lo que los errores asociados son menos limitantes.

El método de separación de señal ($t\bar{t}$+DM) en relación al fondo se basa en primer lugar en el desarrollo de una nueva variable, inspirada en la reconstrucción cinemática de la desintegración dileptónica $t\bar{t}$. Su finalidad ha sido la obtención del momento transverso de la partícula mediadora de espín cero, lo que no es posible de modo analítico, luego debe acudirse a una estrategia numérica. Para incrementar el poder de discriminación, a continuación se efectúa un análisis multivariable basado en redes neuronales artificiales.

Finalmente, no se observa ningún exceso respecto a la predicción del modelo estándar (SM). Al mismo tiempo, establecemos límites de exclusión de la intensidad de esta señal.

La búsqueda de DM en asociación con pares de quark top es en cualquier caso una búsqueda consolidada dentro del programa del LHC. CMS llevó a cabo sendas búsquedas de $t\bar{t}$+DM a $\sqrt{s} = 8$ TeV en los canales dileptónico y semileptónico ([1, 2], respectivamente). Desde 2015, con $\sqrt{s} = 13$ TeV, la colaboración ATLAS ha publicado cuatro análisis (uno por canal más uno inclusivo [3, 4, 5, 6]); por su parte, CMS publicó una primera combinación de los canales semileptónico y hadrónico con los datos de 2015 [7], tiene en preparación la combinación de los tres canales con datos de 2016, y ha publicado una búsqueda dileptónica con los mismos [8], que integra tres estrategias, una de las cuales constituye el núcleo de esta tesis.

Acknowledgements

Although quite modest, this thesis would not have been accomplished without the involvement of a few people to whom I wish to express my gratitude here:

Jónatan Piedra has been a model supervisor who has always made my work easier, particularly in its less exciting aspects. His aesthetic sense together with his ability to detect rare "typo events" have lent a much more pleasant appearance to this dissertation.

Pablo Martínez Ruiz del Árbol undertook to be the locomotive of this analysis in its (twofold) darkest hour, and was the man who ran it from there towards victory, as a both daring and French general. It has been an immense honour to work under him.

For the last year and a half, Cedric Prieels has been a quiet, firm and loyal collaborator, and recently, a diligent proofreader. He has my sincere appreciation for that.

I am extremely thankful to Francisco Matorras, who gave me not one but two opportunities to enlist. His speed in both reasoning and cutting through water —a clipper I would say— have fascinated me; his unquestionable boost has turned out to be essential to complete this doctorate.

I am indebted to Alicia Calderón for a few reasons (books brought from Mexico included), but especially for the help she volunteered that critical week last August —the only one entirely sunny— when everybody would

have preferred to be doing something more satisfying than taking charge of the 2016 data post-processing.

I cannot forget my Ph.D. fellows during these years: Bárbara Chazin, Nicolò Trevisani and Pedro Fernández Manteca, whom I wish a quick and happy ending, nor Daniel Bilbao, who is, in addition, a book supplier of exquisite taste.

Celso Martínez Rivero has lightened my paperwork nuisances —in some cases even more obscure than dark matter itself— eagerly at all times.

I express likewise my frank appreciation to Teresa Rodrigo for her considerate backing and to Alberto Ruiz Jimeno, who submitted, in place of myself, all the documentation for the grant I was eventually awarded. I am grateful to the Ministry of Education-Universidad de Cantabria for it as well.

Lastly, I want to thank everyone from IFCA-Universidad de Oviedo HEP team, who, one way or another, have contributed to my success, especially Rocío Vilar, Luca Scodellaro and Javier Cuevas Maestro.

I wish to remember at this point our co-workers within the CMS collaboration Stanislava Sevova and Kelly Bernaert. They admitted us generously into their bilateral coalition and agreed to put in place a joint strategy for the $t\bar{t}(2\ell)+\text{DM}$ search.

Beyond physics, it has been important to me the unconditional (or conditional) support of the following people: David G. Cuadrado as well as his father, Isabel García García, Lidia Dell'Asta, Roberto Iuppa, Núria Egidos Plaja and Cate and Max Holstein.

I would also like to address a few warm words to Jack Steinberger, who in the course of a one-hour-long post-breakfast conversation at CERN, practically about his childhood and youth, sang to me —first in German, next in English— a military march that he finely remembered from his schooldays at the Republic of Weimar. It was to illustrate the atmosphere of that decade and the coming destiny of Europe and it was a lesson I will never forget.

Inés González Rodríguez is an always smiling woman who knows how to listen. Just for that, she deserves all my admiration.

Professor Miguel Moreno Mas has honoured me with his wisdom, his example and his friendship: I can only hope to feel indebted to him for many more years.

Professor J.R.G. Martínez and her wife have gifted me their unselfish advice whenever I have asked for it, and have shown an unchanging interest in the status of this thesis and, in general, of my life.

Finally, my family has constituted and constitutes my best reserve of love, dignity, courage and shame. This thesis can by no means match up to their qualities and hence it would be ridiculous to dedicate it to them.

Santander, June 2018

Contents

Acronyms

ALICE A Large Ion Collider Experiment.

ANN artificial neural network.

ATLAS A Toroidal LHC Apparatus.

BBN Big Bang nucleosynthesis.

BDT Boosted decision tree.

BSM beyond standard model.

CERN European Organization for Nuclear Research.

CHM composite Higgs model.

CMB cosmic microwave background.

CMS Compact Muon Solenoid.

CSC cathode strip chamber.

CSV combined secondary vertex.

DAQ data acquisition.

DCS detector control system.

DM dark matter.

DT drift tube chamber.

ECAL electromagnetic calorimeter.

EFT effective field theory.

EWSB electroweak symmetry breaking.

FIMP feebly interactive massive particle.

FR fake rate.

HCAL hadron calorimeter.

HLT high-level trigger.

IP interaction point.

JEC jet energy correction.

LEP Large Electron-Positron.

LHC Large Hadron Collider.

LHCb LHC beauty.

LO leading order.

LSP lightest supersymmetric particle.

MC Monte Carlo.

MET missing transverse energy.

MFV minimal flavour violation.

MOND modified Newtonian dynamics.

NLO next-to-leading order.

NNLL next-to-next-to-leading logarithm.

NNLO next-to-next-to-leading order.

PAG physics analysis group.

PDF parton distribution function.

PDG Particle Data Group.

PF particle flow.

POG physics object group.

PR prompt rate.

PU pile up.

PV primary vertex.

QCD quantum chromodynamics.

RPC resistive plate chamber.

SM standard model.

SUSY supersymmetry.

TMVA Toolkit for Multivariate Data Analysis.

WIMP weakly interactive massive particle.

Introduction

For the last ninety years, even though very sporadically at the beginning, astrophysics and cosmology have been providing well-established proofs to suspect that the Universe contains a non-luminous, abundant, and currently unknown ingredient, the so-called dark matter (DM). For the same period, and before, physics has gone unveiling the innermost nature of ordinary matter in terms of elementary particles, what drives us to think of DM as another particle (or particles) [9].

The target of this investigation, as many others today, is to discover it.

If aside from gravity, DM is non-interacting at all, our hope seems vain. But if not, it could have interacted with visible particles more often than today in the hotter, more packed early universe. In that case, current DM remnants could be explained by a candidate with mass and co-annihilation cross section typical of the electroweak scale [10]. That would be very encouraging for particle physics per se, which keeps suffering from the so far unavoidable hierarchy problem [11].

Of course, in the DM hunt different approaches are being employed. The one considered here relies on the hypothetical creation of DM particles from high energy proton-proton collisions. The Large Hadron Collider (LHC) at the European Organization for Nuclear Research (CERN) was built to explore the electroweak scale. During the first period of operation, its detectors ATLAS and CMS succeeded in discovering the Higgs particle [12, 13]. In parallel, searches for DM have been, and are being, performed, either within specific models, such as supersymmetry (SUSY) [14], or in a generic way, e.g.

1

missing energy plus something else. The search presented here is based on the latter.

Phenomenological models to orientate and support the searches were ready at once. Inspired by the Higgs and the uncharged, massive Z, they envisaged new spin-0 and spin-1 fields connecting both sectors [15]. The minimal flavour violation (MFV) hypothesis, which affirms that all the flavour hierarchy of the standard model (SM) is linked to the known structure of the Yukawa couplings [16], is always respected. This results in a clear consequence for the spin-0 case: the heavier the visible fermion, the higher the probability of leading us to the "darkness". This leads to our signal model: top-antitop quark pairs in association with DM ($t\bar{t}$+DM). Of course, first of all, it is necessary to produce so heavy fermions in our collisions.

The top quark, forty-time heavier in fact than the next one downwards, the bottom (b) possesses a unique characteristic: it decays before hadronisation. If one picks those decays which end in leptons instead of lighter quarks (one ninth of all when referring to $t\bar{t}$), he will have to deal with a minimum number of jets: the two originating from the b quarks on the tWb vertices. The motivation under this choice is simple: from an experimental point of view, leptons are much cleaner than jets. This means straighter identification, more accurate momentum computation or less associated uncertainties.

But leptonic decay is linked to the "appearance" of neutrinos, which always implies events not fully reconstructed. However, thanks to the energy-momentum conservation law plus a dose of algebra, the dileptonic $t\bar{t}$ decay chain is fully reconstructible. Unfortunately, this is no longer the case when further invisible particles arise, just like in the $t\bar{t}$+DM process.

The method developed to separate the signal from the background has attempted to distinguish which part of the missing transverse energy comes from known physics (neutrinos) from which does from hypothesized DM. Grounded in the solvability of the $t\bar{t}$ decay kinematic equations [17], it seeks to estimate how much invisible momentum is making the system unsolvable if that happens to be the case.

Furthermore, sinking into the machine learning paradigm more everyday, the separation makes an extensive use of artificial neural networks (ANNs).

At the end, we perform the statistical interpretation of our data and give exclusion limits on the strength of our signal models.

The search for DM in association with top-antitop pairs has, in any case, a worthwhile history within the LHC search program. The CMS collaboration performed two searches with 19.7 fb^{-1} of proton-proton collisions at $\sqrt{s} = 8$ TeV in the dileptonic and semileptonic channels ([1, 2], respectively) interpreting their results in the effective field theory (EFT) context. Concerning the $\sqrt{s} = 13$ TeV phase, the ATLAS collaboration carried out one search per decay channel, i.e. dileptonic [3], semileptonic [4] and all hadronic [5], with its first 13.2 fb^{-1} recorded (2015 and first half of 2016). For its part, CMS published the combination of the semileptonic and all hadronic channels with 2.2 fb^{-1} (2015) [7]. Recently, ATLAS has brought to light the $t\bar{t}$(inclusive)+DM search with 36.1 fb^{-1} (2016 complete) [6] whereas its CMS counterpart is currently in preparation. This nonetheless integrates one of the three dileptonic strategies gathered together in [8], of which the one presented in this dissertation is part.

The dissertation is structured as follows: chapter 1 presents the DM question, the main hunting strategies and the models under consideration for this investigation; chapter 2 gives the description of the collider and the detector; chapter 3 deals with the conversion of wide-ranging measurements into useful data; chapter 4 presents the data used and the event selection; chapter 5 is devoted to the signal-background discrimination; chapter 6 deals with the background prediction; finally, chapter 7 gives the results and the way they were reached as well.

Chapter 1

The dark matter case

This chapter introduces the DM case, one of the most striking enigmas which physics of the 21st century faces, and how it is being addressed by the Large Hadron Collider (LHC), one of the facilities around the world committed to shed light on it. Concisely, the DM problem has to do with the fact that there seems to be an unknown type of matter in the Universe which does not shine nor reflect light but it does show gravitational effects.

The chapter is organized as follows: section 1.1 provides a well-known account of proofs pointing to DM existence; section 1.2 briefly revisits the properties every DM candidate must meet; section 1.3 is devoted to a specific type of candidate and how it is currently being searched at the LHC.

1.1   Evidences

Several astronomical and cosmological observations, not trivially connected to each other, could be explained in terms of a single cause: dark matter.

The first evidence is velocity curves for spiral galaxies. Assuming that Newtonian dynamics keeps applying to galactic scales,[1] objects in the galaxy

---

[1]One can legitimately hypothesize that this is not longer true. Such is the starting point

should rotate according to

$$v_{\mathrm{rot}}(r) = \sqrt{\frac{G_{\mathrm{N}}\,M(r)}{r}}, \qquad\qquad (1.1)$$

where $G_{\mathrm{N}} = 6.67 \cdot 10^{-11}\,\mathrm{N\,m^2\,kg^{-2}}$ is Newton's constant and $M(r)$, the total mass confined within the radius r. One can presume spiral arms to see approximately the same amount of mass inward, that of the luminous core. In other words, for outer regions $M(r)$ does not depend any more on r. Therefore, $v_{\mathrm{rot}}(r)$ should drop off as $v_{\mathrm{rot}}(r) \propto r^{-1/2}$. However, that is not what is observed, but $v_{\mathrm{rot}}(r)$ remains nearly constant up to very large radii [20, 21]. The incongruence between predicted —based upon luminous matter alone— and observed curves leads to postulate the existence of a supplement of non-luminous matter such that $M(r) \propto r$ away from the luminous disk.

The second evidence emerges in the growing scale of galaxy clusters. From the cluster size and the average square of the velocities of its galaxies, by applying the virial theorem (see for instance [22]), one can infer the total mass of the cluster. However, when Fritz Zwicky deployed this method to the "Coma" cluster in 1932, he obtained a value which exceeded significantly the mass computed upon well-established light-mass relations [23], which, in turn, agrees with the one deduced from the temperature measurement of the X-ray emitting hot gas the cluster is mostly made of.

If one had any reservation about cluster weighting by the virial theorem, gravitational lensing comes to clear up any doubt. As general relativity predicts, light bends when it travels across a strong enough gravitational field. Thus, when observed from one side of the gravitational source, glowing objects located behind appear shifted and duplicated. By analysing the pattern of the copies, the gravitational source can be mapped regardless of its luminosity.

The most striking realisation to date is likely to be the "Bullet" cluster [24, 25]. Two galaxy clusters are colliding: the X-ray emitting hot gas com-

---

for modified Newtonian dynamics (MOND) theory: it does not need DM intervention at all [18, 19].

ponents interact with each other powerfully whereas the non-luminous components, gravitationally dominant, interpenetrate with no apparent effort.

The next evidence comes from large-scale structure of the Universe. Observations indicate that matter started to collapse into structure prior to the recombination epoch. This could be only initiated by non-relativistic (cold), non-baryonic matter, i.e. DM [26]. Shortly after recombination, baryons decoupled from photons and fell into the DM potential wells, enlarging their perturbations up to the structure observed today.

And last but not least, is the evidence from the cosmic microwave background (CMB). Impressively squeezed, the mere temperature anisotropies of the eldest light in the Universe have allowed to estimate the contribution to the whole energy density of baryonic matter and DM, Ω_b and Ω_χ, respectively. Full-sky "Planck" data, treated in the framework of six-parameter ΛCDM model,[2] have led to:

$$\Omega_\chi h^2 = 0.1186 \pm 0.0020\,, \qquad \Omega_b h^2 = 0.02226 \pm 0.00023\,,$$

where h is the Hubble constant in units of 100 km s^{-1} Mpc^{-1} [27]. Moreover $\Omega_b h^2$ is in agreement with but much more precise than the determination from the Big Bang nucleosynthesis (BBN) [28]. In plain words: matter from which stars and ourselves are made of accounts for no more than one fifth of the total matter in the Universe.

1.2   Properties

Provided the success of physics in giving the most reductionistic explanation of nature in terms of particles, one tends to assume that DM is a particle [9]. This section outlines which requisites, apart from being gravitationally interactive, any DM candidate must fulfil.

First of all, it must be chargeless. Otherwise, it would interact electromag-

---

[2]Also called "concordance cosmology" or "standard cosmological model".

netically, thus, for example, it would scatter light, revealing itself.

It has to be non-baryonic because baryonic matter density, estimated from BBN and CMB in independent and compatible ways, turns out to be insufficient to account for DM density, determined from CMB too as described above.

DM needs to be cold, i.e. non-relativistic, long before the matter domination era, so that it served as structure seeds. Otherwise, it would have erased density perturbations up to scales which match the observed structure today.

All these conditions exclude any particle within the SM of particle physics, therefore DM has to be ascribed to the sphere of beyond standard model (BSM) theories.

Apart from gravity, DM particles could interact with each other via some other type of exclusive interaction. Although strong self-interactions are dismissed, DM is not required to be entirely collisionless [29].

Finally, whatever the DM candidate, one needs to equip it with a production mechanism which brings it to the observed relic density, Ω_χ. Amongst the most renowned, is the "thermal freeze-out" (see for instance [10]). "Thermal" means that, in the early universe, DM particles were in thermal equilibrium with other species of the cosmic soup, that is, DM co-annihilated to SM particles and vice versa at even rates. However, because of the Universe expansion, encounters became more unlikely as well as less energetic. As a consequence, massive particles decoupled from the thermal bath and started a kind of secluded life. This is the "freeze-out".

The thermal freeze-out mechanism allows to express the relic density in terms of the strength of the interaction between the visible and the dark sectors, g, and the DM mass, m_χ, in the following way:

$$\Omega_\chi \propto \frac{m_\chi^2}{g^4}. \tag{1.2}$$

What makes the mechanism so esteemed is the fact that if one assumes

g of the order of the Fermi constant ($G_{\mathrm{F}} \sim 10^{-5}$ GeV^{-2}), the observed relic density is achieved for DM masses typical of the electroweak scale: 10 GeV - 1 TeV. Triggered by this simple argument, the generic DM candidate associated to the thermal freeze-out is the so-called weakly interactive massive particle (WIMP). It should be noted, however, that equation (1.2) does not necessarily imply WIMP DM: one can assume another strength, thus another DM mass scale [30].

1.3 WIMP searches

DM candidates, either thermally or non-thermally produced, are nonetheless assorted. In spite of the fact that the search presented in this thesis aims at WIMP DM, many well-motivated proposals are also on the market: axions [31, 32], sterile neutrinos [33], SuperWIMPs [34], feebly interactive massive particles (FIMPs) [35], WIMPless DM [30], etc. So why are WIMPs so desired? The answer is simple: because they would serve to another major purpose: the long-pursued stabilization of the electroweak scale against the Planck scale or the "hierarchy problem" [11].

WIMPs themselves could be as varied as theories addressing the hierarchy problem: SUSY [14],[3] extra dimensions [36, 37], little Higgs [38], composite Higgs model (CHM) [39], mirror model [40, 41], etc.

WIMP searches have been deployed in three main fronts: direct and indirect detection as well as collider production —and detection, of course.

Not exclusive to WIMPs, indirect detection is founded on the search of known particles, such as gamma-rays, energetic neutrinos or antimatter, which could be potential debris from DM co-annihilation occurring far away from Earth [42]. Three representative "observers" are the Large Area Telescope on the Fermi Gamma-ray Space Telescope [43], the IceCube Neutrino Observatory [44] and the Alpha Magnetic Spectrometer on the International

---

[3]The lightest supersymmetric particle (LSP), in the context of (R-parity conserving) SUSY models, has been arguably the canonical WIMP candidate for the last three decades.

Space Station [45].

Direct detection, in turn, is based on hypothetical collisions between galactic DM and nuclear targets placed on purpose, usually under the shielding of several hundred meters of rock to reject undesired projectiles. The recoils of the nuclei would produce a detectable signal. Current most sensitive experiments within this class are XENON1T [46], PandaX-II [47], LUX [48], DarkSide-50 [49, 50] and Deap-3600 [51].

Leaving SUSY exploration aside, WIMPs in hadronic colliders are basically searched through the missing energy$+X$ signature. This hunt dates back to the Tevatron days [52]; the LHC Run-1 took up the torch, see [1, 53, 54]. One as much as the other based their searches on EFT framework for which a contact interaction was assumed between SM and DM particles, much like 4-Fermi theory. The kinematics of the signal was influenced by the type and mass of the DM particle and the Lorentz structure of the interaction. This approach exhibited the advantage of straightforward comparison with direct detection results [55], but the disadvantage of a limited regime of validity. In effect, as long as one deals with low transfer momenta with respect to the masses of the underlying theory, the EFT ansatz works with no trouble. But LHC Run-2 incoming particle momenta could be comparable to SM-DM mediator masses, corrupting EFT-based results [56, 57].

The natural way out have lied in the so-called "simplified models", intended to capture hints of new physics but avoiding excessive model dependency and number of free parameters [58, 15, 59]. In this way, mediators are explicitly characterized by their mass and spin. To be specific, this thesis deals with the model shown in figure 1.1, which belongs to a wider class characterized by the fact that the communication between the visible and the dark sectors occurs via a spin-0 mediator, much like the SM Higgs particle [60, 61], coupling both sides with same parities —either scalar (S) or pseudoscalar (P)—, but not necessarily with identical strengths. The following Lagrangian terms condensate the interactions just described:

$$\mathcal{L}_{\mathrm{S}} = g_\chi \phi \bar{\chi}\chi + \frac{\phi}{\sqrt{2}} \sum_i \left(g_u y_i^u \bar{u}_i u_i + g_d y_i^d \bar{d}_i d_i + g_\ell y_i^\ell \bar{\ell}_i \ell_i \right), \tag{1.3}$$

$$\mathcal{L}_{\mathrm{P}} = g_\chi \phi \bar{\chi}\gamma^5\chi + \frac{i\phi}{\sqrt{2}} \sum_i \left(g_u y_i^u \bar{u}_i \gamma^5 u_i + g_d y_i^d \bar{d}_i \gamma^5 d_i + g_\ell y_i^\ell \bar{\ell}_i \gamma^5 \ell_i \right), \tag{1.4}$$

where it has been supposed that DM is a single particle, Dirac fermion,[4] pair-produced, and the MFV hypothesis rules the couplings to the SM part [16].[5] In the interest of simplicity, their coupling strengths are unified into a single universal parameter: $g_q \equiv g_u = g_d = g_\ell$. Thus, the minimal set of parameters under consideration is composed of the mass of the DM candidate, m_χ; the mass of the mediator, m_ϕ; the coupling strength between the mediator and the dark sector, g_χ; and between the mediator and the visible sector, g_q: $\{m_\chi, m_\phi, g_\chi, g_q\}$.
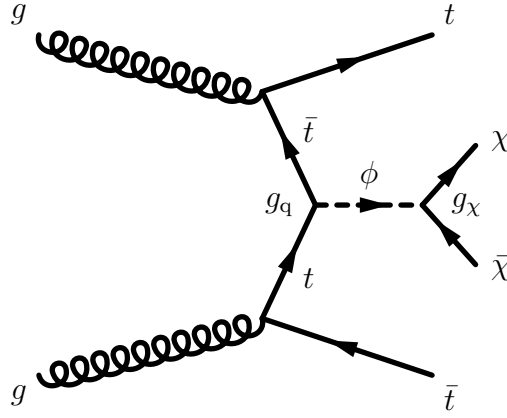

Figure 1.1: Feynman diagram of DM production in association with $t\bar{t}$.

Very much like the Higgs production in hadronic collisions, the prevailing way of the above-described DM production at the LHC would occur via

---

[4]Roughly speaking, different spins of DM particle lead to similar kinematic distributions and it is expected to have a residual impact on cut-and-count analyses [62].

[5]MFV requires that any flavour interaction follows the same structure as the SM Yukawa interaction. As a consequence, spin-0 couplings to fermions are proportional to fermion masses: $y_i^f = \sqrt{2}/v\, m_i^f$, being v the Higgs vacuum expectation value.

gluon fusion, through the loop-induced $gg\phi$ coupling, see figure 1.2, since tree-level Yukawa coupling to lighter quarks are suppressed [63]. However, when the mediator is produced in association with heavy quarks, the case this thesis will deal with, tree-level terms dominate.
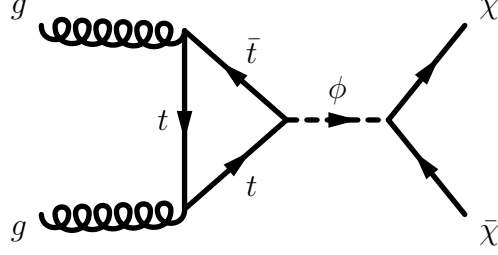

Figure 1.2: DM production via gluon fusion through a (top) quark loop.

The minimal mediator width,[6] neglecting the small contributions from quarks other than top in the loop, is given by:

$$
\Gamma_{S,P} = \sum_f N_c \frac{y_f^2 g_q m_\phi}{16\pi} \left(1 - \frac{4m_f^2}{m_\phi^2} \right)^{n/2} + \frac{g_\chi^2 m_\phi}{8\pi} \left(1 - \frac{4m_f^2}{m_\phi^2} \right)^{n/2} \\
+ \frac{\alpha_s^2 y_t^2 g_q m_\phi^3}{32\pi^3 v^2} \left| \Psi_{S,P} \left(\frac{4m_t^2}{m_\phi^2} \right) \right|^2 .
\tag{1.5}
$$

where $n = 3$ for scalars and $n = 1$ for pseudoscalars. The loop integrals, with Ψ as complex functions, are

$$
\Psi_S(z) = z \left[1 + (1-z)\arctan^2 \left(\frac{1}{\sqrt{z-1}} \right) \right] ,
\tag{1.6}
$$

$$
\Psi_P(z) = z \arctan^2 \left(\frac{1}{\sqrt{z-1}} \right) .
\tag{1.7}
$$

The minimal widths for scalar and pseudoscalar interactions with $g_q = g_\chi = 1$ are shown in figure 1.3, illustrating the effect of choosing the

---

[6] "Minimal" because couplings no other than strictly those described by equation (1.3) or equation (1.4) are considered.

mediator coupling to fermions exactly equal to that of the SM Higgs. It is worth noting that for the mediator mass above twice the top quark mass, $m_t = 172.5$ GeV, the minimal width receives the dominant contribution from the top quark. For lighter mediator masses, the DM dominates as the couplings to light quarks are Yukawa suppressed.

During the first half of 2015, the DM working group constituted at CERN performed dedicated studies to determine the most appropriate parameter scan for the $t\bar{t}$(inclusive)+DM searches with a view to an integrated luminosity of some tens of inverse femtobarns.[7] Choices of $\{m_\chi, m_\phi, g_\chi, g_q\}$ were assessed in terms of the spectrum of the missing transverse energy[8] (represented by "E_T^{miss}"), the key observable for invisible hunts in hadronic colliders. It was concluded that a) kinematics mostly depends on the masses m_χ and m_ϕ, figure 1.4; b) g_χ and g_q feebly affect it; c) the E_T^{miss} spectrum broadens with larger m_ϕ, figure 1.4; d) differences in E_T^{miss} spectrum between scalar and pseudoscalar interactions are larger for light mediators with respect to heavier mediators. Differences were also observed between $m_\phi \lesssim 2m_\chi$ regimes, but provided this thesis is restricted to $m_\phi > 2m_\chi$ models because of sensitivity, they will not be considered.

---

[7]Plain "luminosity" is defined like a particle flux, in our case the flux of protons. "Integrated" means to integrate over time. The higher the integrated luminosity, the higher the chance of a reaction or process to occur. Integrated luminosity is represented by $\mathcal{L}$ and it has dimension of $[\mathrm{area}]^{-1}$

[8]A complete description of the missing transverse energy observable will be given in chapter 3.
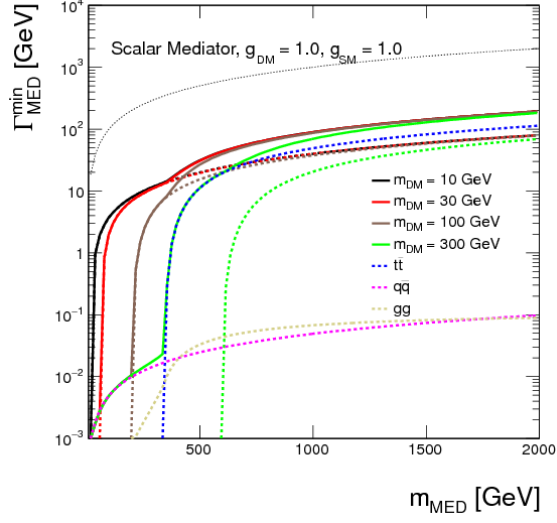
(a)
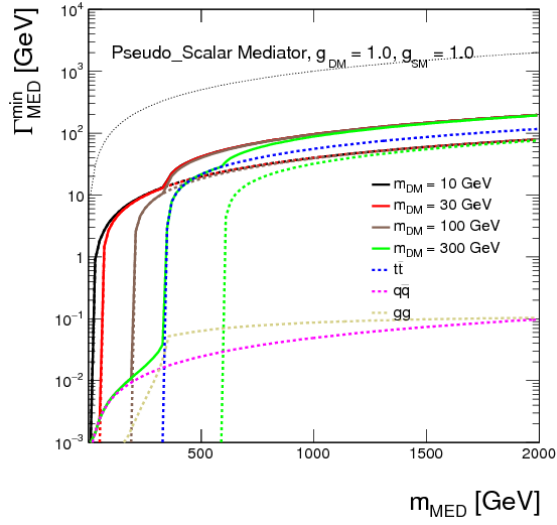
(b)

Figure 1.3: Minimal width as a function of mediator mass for (a) scalar and (b) pseudoscalar interactions, assuming $g_q = g_\chi = 1$. The total width is shown as solid lines for DM masses of $m_\chi = 10$ GeV, 30 GeV, 100 GeV and 300 GeV in black, red, brown and green, respectively. The individual contributions from DM are indicated by dotted lines with the same colors. The contribution from all quarks but top is shown as magenta dotted line and the contribution from top quarks only is illustrated by the dotted blue line. The dotted beige shows the contribution from the loop-induced coupling to gluons. The dotted black line shows the extreme case $\Gamma_{min} = m_\phi$. (Figure borrowed from [62].)
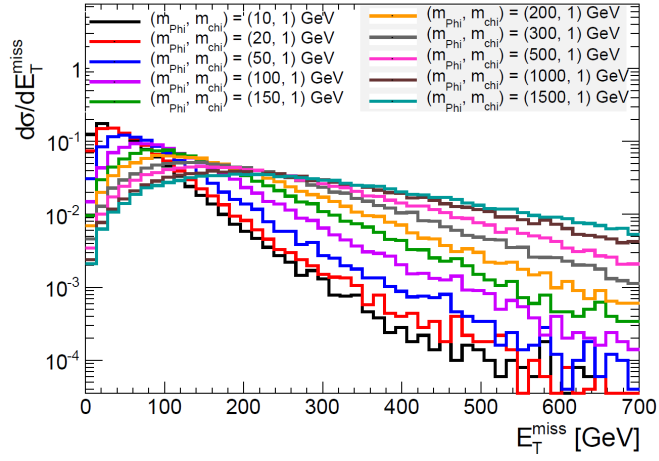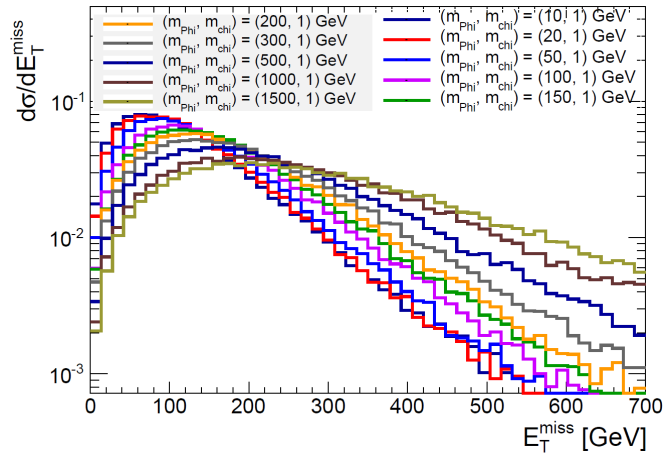
Figure 1.4: Dependence of the kinematics on the (a) scalar, (b) pseudoscalar mediator mass in the $t\bar{t}$+DM signature. The DM mass is fixed at $m_\chi = 1$ GeV. (Figure borrowed from [62].)

Chapter 2

The collider and the detector

Science requires data. To obtain them, mounting an experiment is often indispensable; in any case, it always requires appropriate measurement instrumentation. This chapter deals with the experimental setup used to generate and collect our data: the Large Hadron Collider (LHC) and the Compact Muon Solenoid (CMS) detector, respectively. It is worth remarking that taken as a whole, it is the biggest experiment ever: conceived from the 1970s, expected to be still standing until 2035-2040, served by crews of thousands of people, a cost of several thousands of millions of euros, etc.

The chapter is divided in two parts. Section 2.1 gives an account of how physics has gradually uncovered the structure of matter, the key role of accelerators on it, and the characteristics and parameters of interest of the LHC. Section 2.2 is devoted to the detector. Firstly, its design criteria are linked to the challenges of current physics, especially the electroweak symmetry breaking (EWSB) by the Higgs particle; next, the five subdetectors making it up are outlined one by one; finally, a few words are given about the trigger and the data acquisition system.

2.1   The LHC

Far from obvious, discontinuous nature of matter was proved indubitably as late as 1908 by Perrin, and awarded the Nobel Prize in 1926, the same year Schrödinger published the wave mechanics. Nonetheless, great geniuses such as Maxwell, Boltzmann or Einstein had founded their successful theories based on this assumption since fifty years before.

To trace back the steps of modern atomic hypothesis, one must go back to the days of the French Revolution. Investigations by Lavoisier and Joseph Louis Proust —the latter working under Spanish crown sponsorship—, condensed in their famous laws, led the English schoolteacher John Dalton to propose that matter is made from discrete, definite entities. "Atomic weight" was coined to mean the weight of each element combining with a reference weight of a reference element —differences between atoms and molecules had not arisen yet—. The number of units in one atomic weight is the so-called "Avogadro's number", N_{A}.

The systematic study of electrolysis by Faraday in the 1830s brought to light that electrical and material phenomena were more closely related than it might have seemed in the beginning. Remarkably, Faraday observed that it was required a fixed amount of *electrical current* × *time* to collect one atomic weight of (monovalent) element at the electrodes. He named that amount F. It was tantalising to associate the quotient of F/N_{A} to a preliminary concept of "unit of charge".

In 1897, J. J. Thomson was the first who observed it, measured its mass-to-charge ratio and published that it constituted an unknown form of matter [64]. The instrument he used to evidence their nature was a Crookes tube, a primitive accelerator. This event marked the starting point of particle physics.

But ejection of particles can also take place without human intervention at all. That was what Henri Becquerel had noticed just some months before, when he left accidentally a uranium salt together with a photographic plate

inside an opaque drawer for a few hours. Once he developed the plate, he realised that the salt had left an impression on it [65].

Not many years later, the Austro-Hungarian physicist Victor Hess, equipped with an electroscope, boarded a balloon, rose five kilometres over the domes and roofs of Vienna and measured that ionising radiation was not lower than on the ground, but higher [66]. His conclusion was that Earth was being continuously bombed by an unknown type of radiation from outer space, the so-called "cosmic rays".

Artificially accelerated or naturally fired, energetic particles have proved to be instrumental in our increasingly deeper understanding of the structure of matter. The electron was just the overture. Without being exhaustive, it was followed by the discovery of the nucleus (1909), the photon (1916), the positron (1931), the neutron (1932), the muon (1936), the pion (1947), the kaon (1947), the antiproton (1955), the electron neutrino (1956), the J/ψ meson (1974), the tau lepton (1975), the Υ meson (1977), the the W and Z bosons (1983) and the top quark (1995). Incredibly, all this zoo fitted into the so-called standard model (SM) of particle physics with relative ease if just one particle more was found. To capture it the biggest machine in the world was built.

Planned from 1984, constructed from 1994, operated since 2008, the LHC was already envisaged as far as 1975 [67]. Housed in the same 27-kilometre-long underground tunnel of the Large Electron-Positron (LEP) [68], able to provide each one of the two counter-rotating beams of protons with an energy of 7 TeV and to circulate a peak luminosity of $2 \cdot 10^{34}$ cm^{-2} s^{-1}, its primary purpose was to elucidate the nature of the EWSB, occurring at the 100 GeV - 1 TeV regime, for which the Higgs mechanism [69, 70, 71] was presumed to be responsible. This hit was achieved within its first years of operation, and by the 4th July 2012, the discovery of a SM-compatible Higgs boson with a mass of 125 GeV was announced urbi et orbi [13, 12].

But the LHC (and their detectors) were conceived not only to put the cherry on top of the SM, but also to explore physics beyond. Provided its available

energy in addition to its luminosity, two routes are opened in this sense:

On one hand, the LHC is a raw factory of particles as heavy as the W and Z bosons, the top quark, and the Higgs particle themselves. Precision measurements of their properties will prove consistency of the SM; otherwise, they will reveal subtle discrepancies guiding researchers somewhere else.

On the other hand, there is a broad program of searches aiming at clear signatures of new physics (mass resonances, missing energy, etc.), which are constraining extensions of the SM like SUSY more everyday.

In a more detailed way, the shaping of the beams and the transfer of momentum are realised as follows: Streaming out of a tank similar to a diving cylinder, hydrogen molecules are firstly dissociated and ionised to become protons. From this point forward, they will undergo a series of speed-up steps throughout veteran CERN accelerators, as shown in figure 2.1. The injection chain starts in the Linac 2, which confers them momentum up to 50 MeV; the Proton Synchrotron Booster, up to 1.4 GeV; the Proton Synchrotron, up to 25 GeV; the Super Proton Synchrotron, up to 450 GeV; and finally, they enter the LHC in two separate, counter-rotating beams.

Once there, radiofrequency cavities (eight per beam) deliver momentum in successive turns up to the top energy, 6.5 TeV at present, as well as quadrupole magnets focus the beams so that protons do not repel themselves in a non-functional way. Around a thousand of superconducting dipole magnets distributed along the 27 kilometres circumference bend the beams appropriately.

The beam is indeed a series of bunches, nominally spaced 25 ns apart from each other, implying that the entire ring fills with three thousand of them approximately. Every bunch contains in the order of 10^{11} protons, of which just a tiny amount (some tens) gives rise to head-on collisions at the four interaction points (IPs), where the detectors —ALICE, ATLAS, CMS and LHCb— lie in wait.
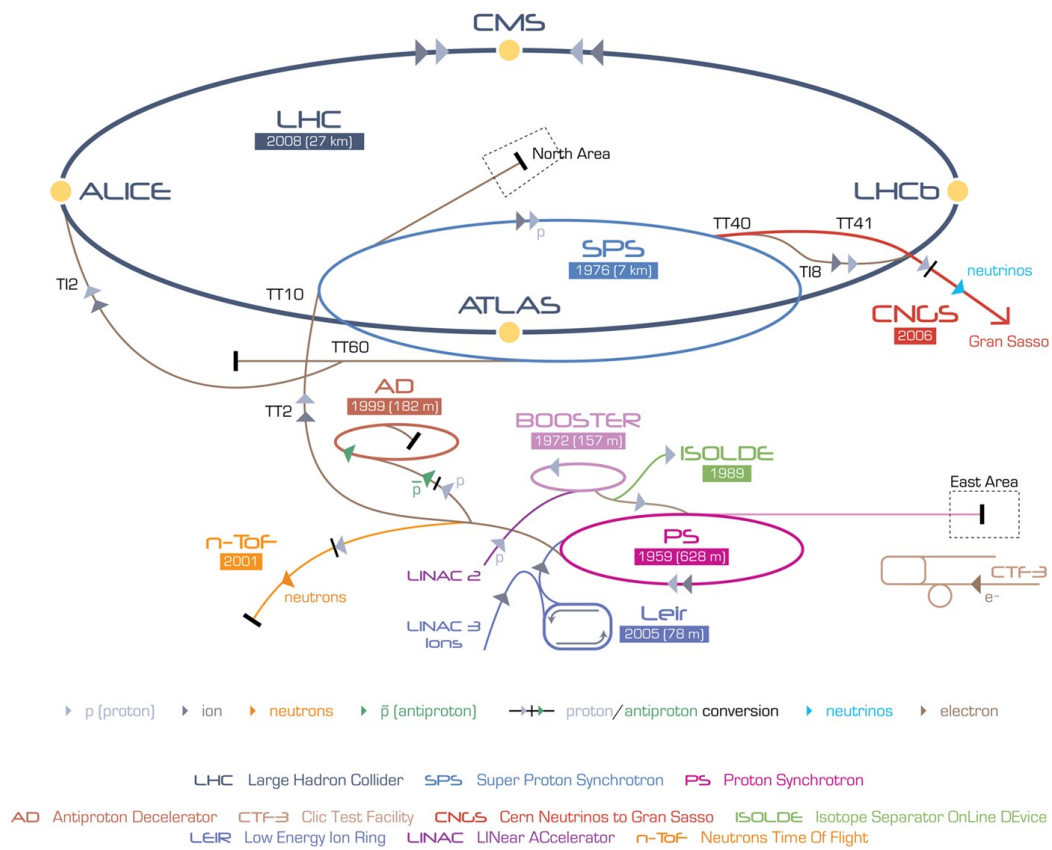
Figure 2.1: LHC injection chain.

Luminosity in the IPs is given by:

$$L = \frac{\gamma f k_B N_p^2}{4\pi\varepsilon_n\beta^*}F,$$
(2.1)

where

- γ is the Lorentz factor,

- f is the revolution frequency,

- k_B is the above-mentioned number of bunches,

- N_p is the above-mentioned number of protons per bunch,

- ε_n is the normalised transverse emittance,

- β^* is the betatron function at the IP, and

- F is the reduction factor due to the crossing angle.

Figure 2.2 shows the production cross section for different SM final states from proton-proton collisions, such as those occurring at the LHC as a function of the centre-of-mass energy.

The complexity of such an astonishing performance would be nonsensical if it was not for the "eyes" of the LHC, that is, its detectors.

2.2   The CMS experiment

Exactly half a century ago, Steven Weinberg proposed one Yang-Mills theory for the unification of the weak and electromagnetic interactions in which the Higgs mechanism —developed three years before— was put to good use to give mass to the short-range hypothesised weak bosons whereas the gauge invariance was kept intact [72]. The work did not draw much attention until four years later, when Gerard't Hooft, just a graduate student, proved that
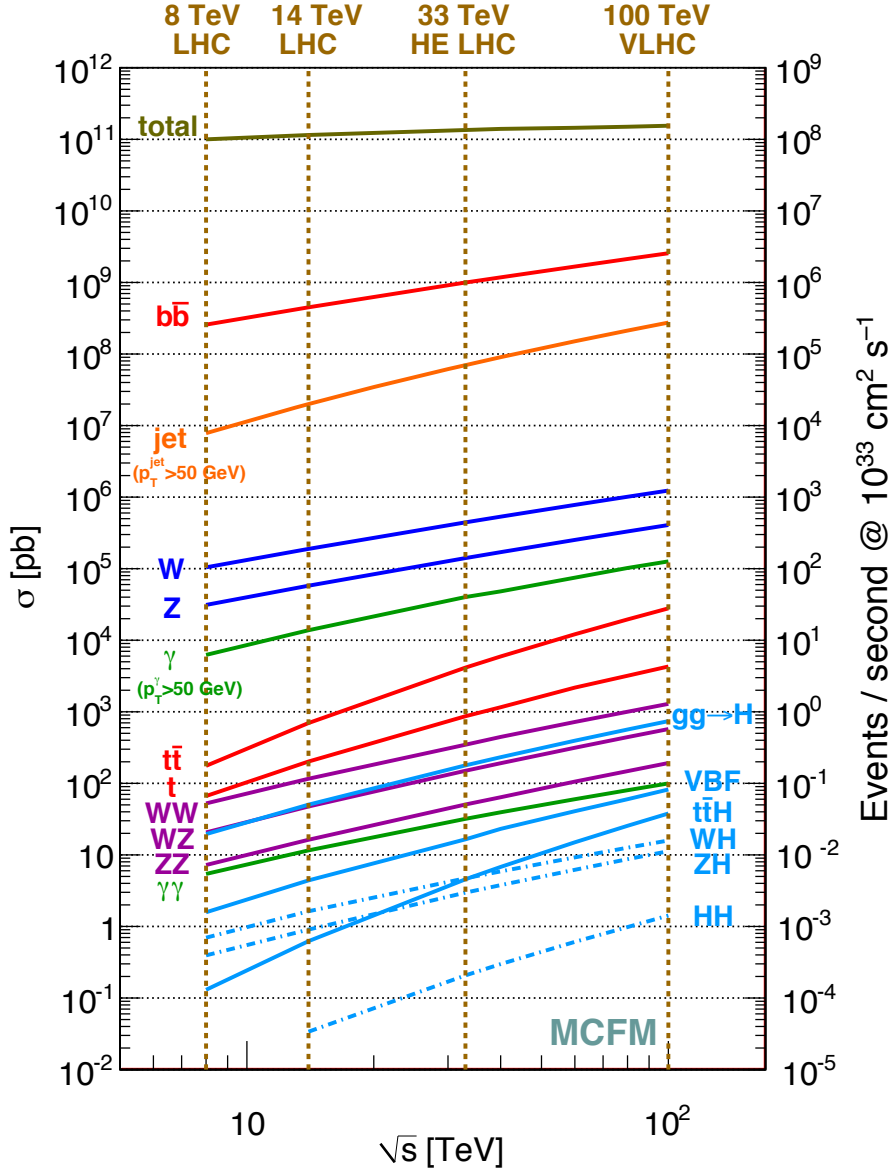
Figure 2.2: Production rates of SM final states from proton-proton collisions, such as those at the LHC, as a function of the centre-of-mass energy, $\sqrt{s}$. Figure taken from `https://mcfm.fnal.gov`.

spontaneously broken Yang-Mills theories were renormalisable [73]. Two decades of stunning discoveries, from the neutral currents to the top quark, followed. By the end of the twentieth century, only the Higgs particle was missing.

If the electroweak interaction looses its single nature at the 100 GeV scale through the dynamics of an elementary complex doublet of scalar fields, as dictated by the SM, one by-product is a physical scalar particle, i.e. the Higgs, whose mass was known to be greater than 114.4 GeV by 2010 [74]. Coupled to weak bosons, fermions as well as to itself, the relative rates of the different Higgs decay modes as a function of its (unknown by then) mass are showed in figure 2.3. One can deduce the following information:
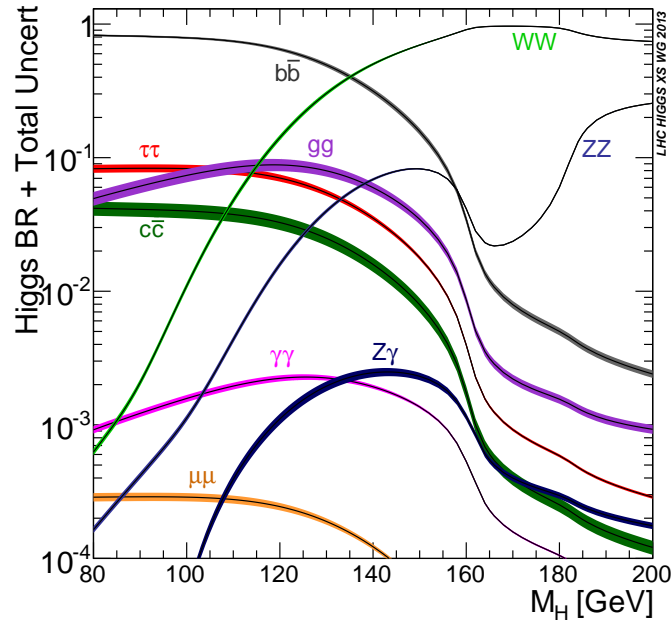

Figure 2.3: Relative decay rates for the SM Higgs as a function of its mass, unknown until 2012.

- For $m_H \lesssim 135$ GeV, the prevailing mode is $b\bar{b}$. However, being the collider hadronic, quantum chromodynamics (QCD) backgrounds degrades the significance of the signal, while the mass resolution obtain-

able with jets is limited.[1] Similar considerations affect gg, $c\bar{c}$ and $\tau\bar{\tau}$.

- For $m_H < 2m_Z$, the Higgs resonance is only a few MeV narrow, meaning that the discovery would have been dominated by the instrumental mass resolution.

- The WW mode, with the W bosons decaying in one electron or muon plus their corresponding invisible neutrino does not allow to reconstruct the Higgs mass.

The stated above, together with other considerations concerning BSM searches, led to demand:

- Good muon identification and momentum resolution over a wide range of momenta, good dimuon mass resolution ($\approx 1\%$ at 100 GeV), and the ability to determine unambiguously the charge of muons with $p < 1$ TeV.

- Good electromagnetic energy resolution, good diphoton and dielectron mass resolution ($\approx 1\%$ at 100 GeV), wide geometric coverage, measurement of the direction of photons and correct localisation of the primary interaction vertex, π^0 rejection and efficient photon and lepton isolation at high luminosities.

- Good missing transverse energy and dijet mass resolution, requiring hadron calorimeters with a large hermetic geometric coverage and with fine lateral segmentation.

Particles can be directly measured only if they live long enough to reach the detector and are able to interact with it.[2] Just a handful of them meet both requirements: electrons, protons, photons, neutrons, muons, charged pions and kaons. On the other hand, interaction with matter determines the range of penetration.

---

[1]Indeed, knowing the Higgs mass is 125 GeV (2012), it has not been until recently (2017) that this decay has been observed [75, 76].

[2]Being long-lived, neutrino does not interact, neither does potential DM.

As a general rule, any high energy physics detector is composed of different subdetectors, nested inside each other, like a matrioshka doll, in the following order (from the IP outwards): vertex detector, tracking detector, electromagnetic calorimeter, hadron calorimeter and muon detector. The whole setup is usually immersed within a magnetic field, in order to deflect charged particles via the Lorentz force and, in this way, measure their momenta from their bending.

The defining feature of the Compact Muon Solenoid (CMS) experiment is an uniform 4 T magnetic field created by a 25-m-long, 6 m inner diameter, superconducting solenoid [77], as the acronym itself stands for. Likewise, it is "compact" because of the tightly packed arrangement of the different subdetectors alternated with the magnet system, and "muon" for its unequalled performance in muon recording.

In order to increase the magnetic flux density, iron is added (indeed several thousand tonnes of it). It must be noted that, unlike the common case, here the coil is not wrapped around any iron core, but the iron yoke, distributed in different layers, does coat the coil. The motivation is that one vitally needs to preserve the inner volume as free as possible from undesired target material.

A schematic 3D view of the subdetectors and the solenoid can be seen on figure 2.4. Leaving from the IP, one can find: the vertex detector, the tracking detector, the electromagnetic calorimeter (ECAL), the hadron calorimeter (HCAL), the coil, and the muon system sandwiched between the different layers of the return-flux yoke, which also serves as load-bearing structure of the apparatus.

Before extending the description of each subdetector, a few words about the two reference systems used by the experiment:

A right-handed Cartesian coordinate system is defined with the origin over the nominal IP; the x axis points to the centre of the ring; the y axis does upwards; and the z, westwards, to France.[3]

---

[3]CMS is practically located in the northernmost point of the LHC.

CMS DETECTOR

Total weight : 14,000 tonnes
Overall diameter : 15.0 m
Overall length : 28.7 m
Magnetic field : 3.8 T

STEEL RETURN YOKE
12,500 tonnes

SILICON TRACKERS
Pixel (100x150 μm²) ~16m² ~66M channels
Microstrips (80x180 μm) ~200m² ~9.6M channels

SUPERCONDUCTING SOLENOID
Niobium titanium coil carrying ~18,000A

MUON CHAMBERS
Barrel: 250 Drift Tube, 480 Resistive Plate Chambers
Endcaps: 468 Cathode Strip, 432 Resistive Plate Chambers

PRESHOWER
Silicon strips ~16m² ~137,000 channels

FORWARD CALORIMETER
Steel + Quartz fibres ~2,000 Channels

**CRYSTAL
ELECTROMAGNETIC
CALORIMETER (ECAL)**
~76,000 scintillating PbWO₄ crystals

HADRON CALORIMETER (HCAL)
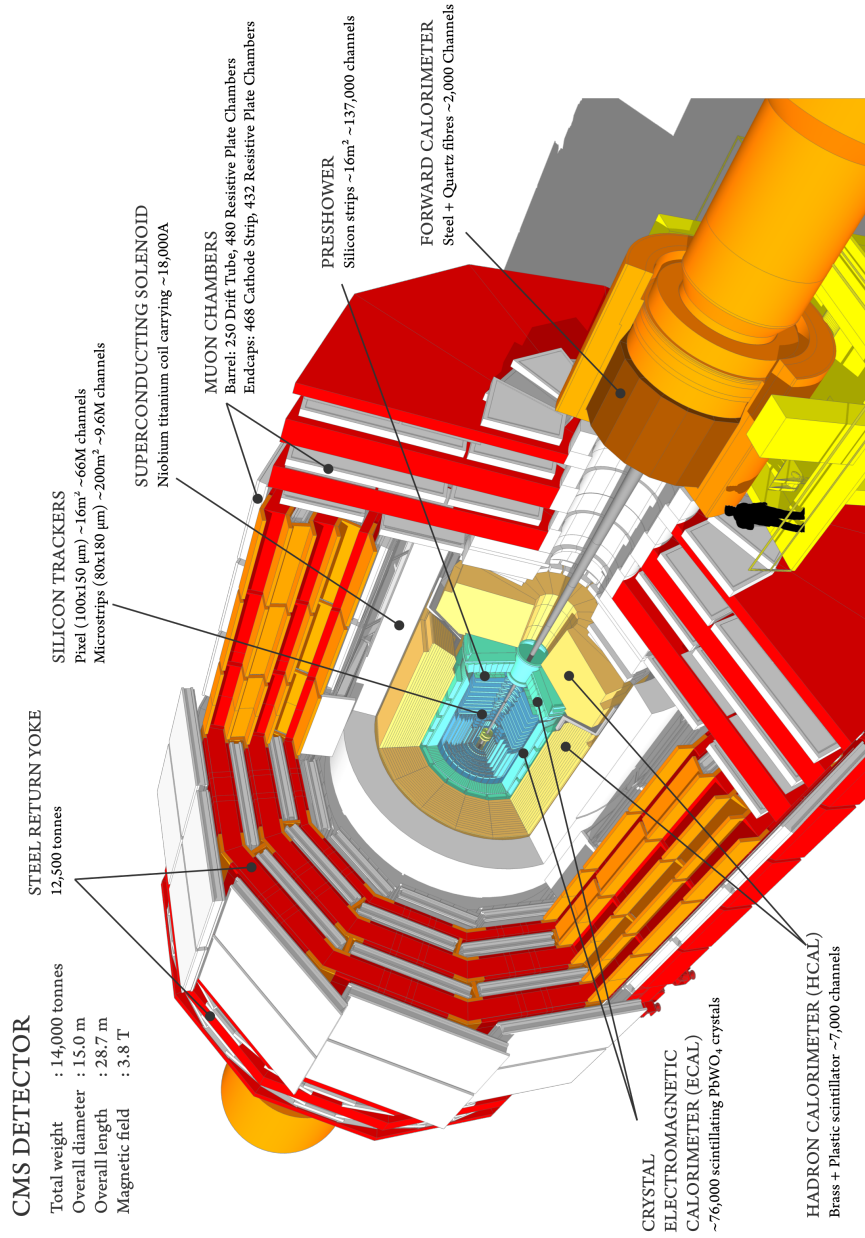Brass + Plastic scintillator ~7,000 channels

Figure 2.4: CMS isometric view, showing the layout of the different subsystems surrounding the IP.

The spherical coordinate system is defined in the usual way from the former: the polar angle, θ, is measured from the positive z axis, and the azimuthal angle, ϕ, from the x axis in the xy plane. For convenience, it is introduced the so-called pseudorapidity, defined as $\eta \equiv -\ln\left[\tan\left(\frac{\theta}{2}\right)\right]$, for which the particle flux of hadron colliders is approximately constant.

2.2.1   Muon system

Detection of charged particles occurs mainly via electromagnetic interaction. On the other hand, the electron and the muon, so similar in a few substantial aspects, differ in their masses and lifetimes. This leads to the fact that in our regime of interest, ($\sim$1 GeV, $\sim$1 TeV), each one leaves its traces through different electromagnetic "variations": the lighter electron looses energy primarily by bremsstrahlung (more in the ECAL subsection), whereas the heavier muon does so by a set of phenomena —ionisation, excitation, etc.— well described by the Bethe-Bloch formula.[4]

Bending of a charged particle in motion by a static magnetic field is proportional to the intensity of the field itself and inversely proportional to momentum of the particle. On the other hand, the lower the bending, the more relatively inaccurate the determination of the momentum.

The purpose of the muon system is to contribute to increase this momentum resolution for muons, as well as their identification, by a joint work with the tracker. As shown in figure 2.5, where momentum resolution defined like $\dfrac{\Delta p}{p}$ is drawn against p, as long as p is under $\simeq$ 200 GeV, the muon system barely improves the performance of the inner tracker by itself in this sense. However, beyond this threshold, its impact is evident: when measurements from both subdetectors are combined, the resolution doubles the one obtained from the inner tracker only.

---

[4]Bethe-Bloch formula works excellently in the range of $0.1 < \gamma\beta < 100$, which means 10 MeV $\lesssim p \lesssim$ 10 GeV in the case of the muon. Hence, radiative losses become not negligible for high-momentum muons.
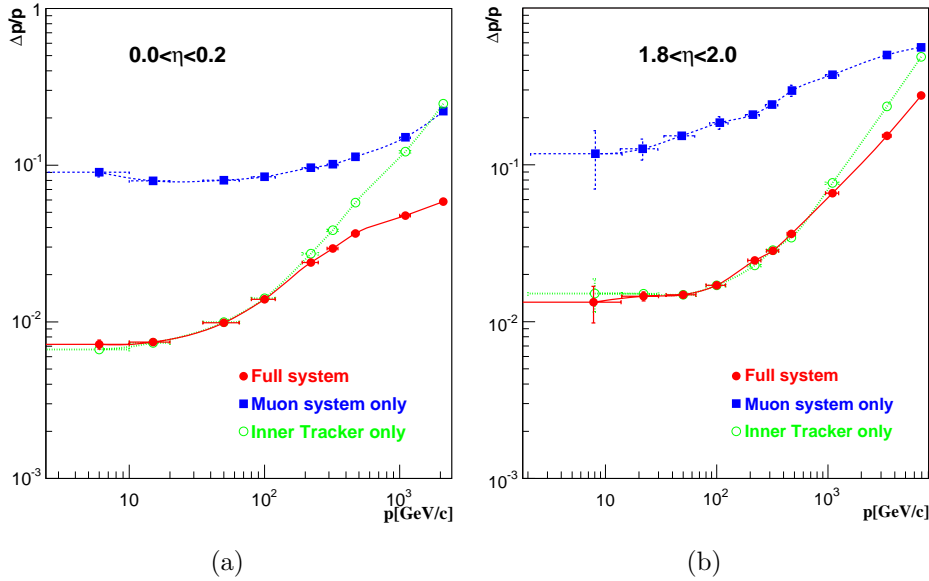
Figure 2.5: The muon momentum resolution, $\Delta p/p$, versus p using the muon system only (blue), the inner tracker only (green), or both (red). (a) central region, $0.0 < |\eta| < 0.2$ and (b), side region, $1.8 < |\eta| < 2.0$. From [77].

Such a significant contribution by the muon system can be attained thanks to the behaviour of the magnetic bath outside the coil. As figure 2.6 illustrates, the crucial role of the return-flux yoke is to allow field lines to be more packed within the whole volume of the detector [78]. Otherwise, they would be infinitely more spread, resulting in relatively poor magnetic intensities, therefore an insufficient bending of muons.

Three types of gaseous detectors, interspersed among the layers of the return-flux yoke, make up the muon system: drift tube chambers (DTs), cathode strip chambers (CSCs), and resistive plate chambers (RPCs). Due to the intensity of the magnetic field around them, spatial resolution is not a stringent requirement they must fulfil.

The DTs are finely segmented in drift cells: the position of the muon is determined by measuring the drift time to an anode wire of a cell with carefully shaped electric field.

The CSCs operate as standard multi-wire proportional counters but use a

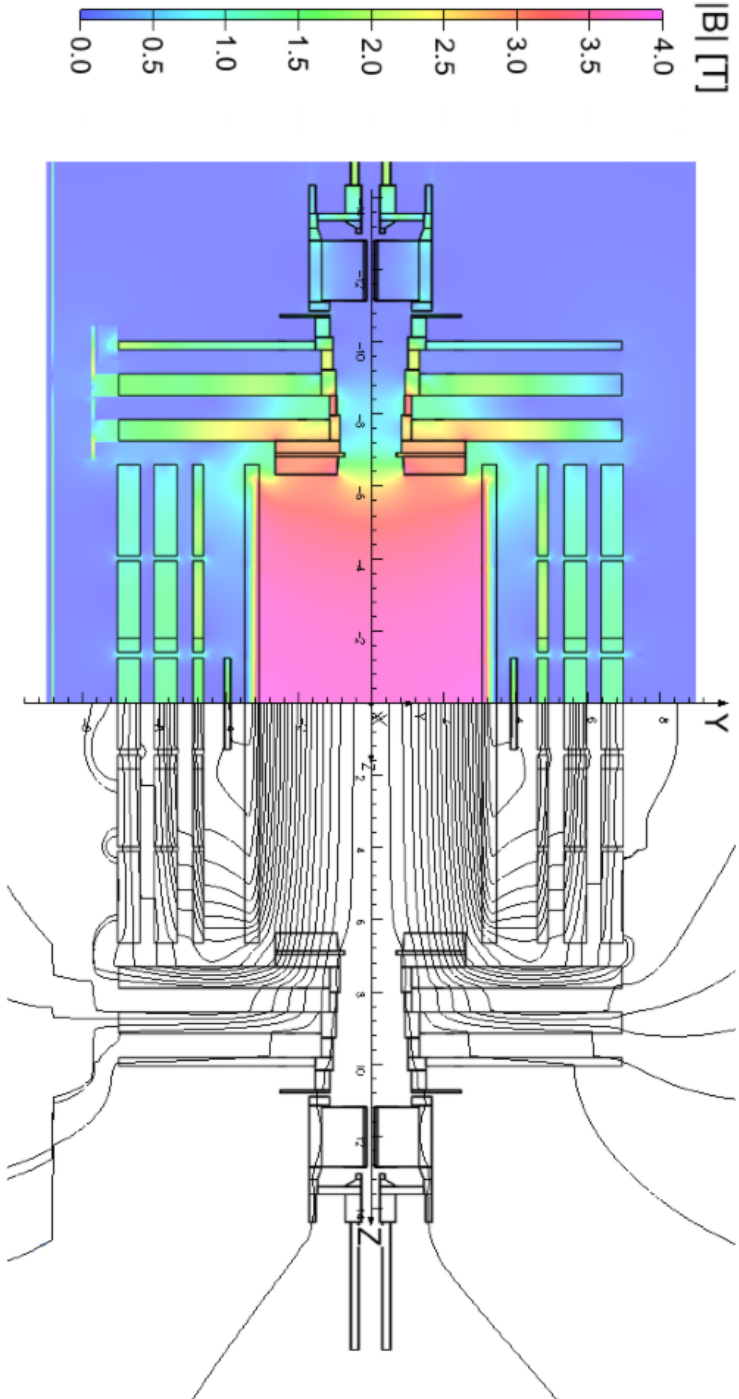Figure 2.6: Map of the $|\vec{B}|$ field (left) and field lines (right) predicted for a longitudinal section of the CMS detector by a magnetic field model at a central magnetic flux density of 3.8 T. Each field line represents a magnetic flux increment of 6 Wb. Rectangles in turquoise (left), where the field lines appear strongly packed (right) correspond to the different layers/modules of the return-flux iron yoke. From [79].

finely segmented cathode strip readout, which yields an accurate measurement of the position at which the muon crosses the gas volume.

The RPCs are operated in avalanche mode to ensure good operation at high rates (up to 10 kHz/cm^2) and have double gaps with a gas gap of 2 mm. RPCs provide a fast response with good time resolution ($\sim$ 1 ns) but with a coarser position resolution than the DTs or CSCs. RPCs can therefore identify unambiguously the correct bunch crossing.

DTs and CSCs are located in the pseudorapidity regions $|\eta| < 1.2$ and $0.9 < |\eta| < 2.4$, respectively, and are complemented by RPCs in the range $|\eta| < 1.9$, see figure 2.7. The three regions naturally defined by the cylindrical geometry of CMS are referred to as the "barrel" ($|\eta| < 0.9$), the "overlap" ($0.9 < |\eta| < 1.2$), and the "endcap" ($1.2 < |\eta| < 2.4$) regions. The chambers have been arranged to form the muon detection system by appropriate placement and overlapping.

2.2.2   Hadron calorimeter

Hadrons, either charged or neutral, interact via the strong force with nuclei of ordinary matter, usually a heavy metal forming the "absorber" in a dedicated detector. In addition to other debris, inelastic collisions will generate new hadrons, which will experience the same process, the following generation likewise, and so on for quite a few cycles, until progeny is not energetic enough to trigger further nuclear activity, all of this giving rise to hadronic cascades. Hadrons from successive generations loose energy when in flying to their target nucleus, they ionise or excite the atoms in between, according to the Bethe-Bloch formula. The subsequent emitted light is what scintillators collect: the signal.

The CMS hadron calorimeters are particularly important for the measurement of hadron jets and neutrinos or exotic particles resulting in apparent missing transverse energy. The hadron calorimeter barrel is radially restricted between the outer extent of the electromagnetic calorimeter ($R = 1.77$ m)
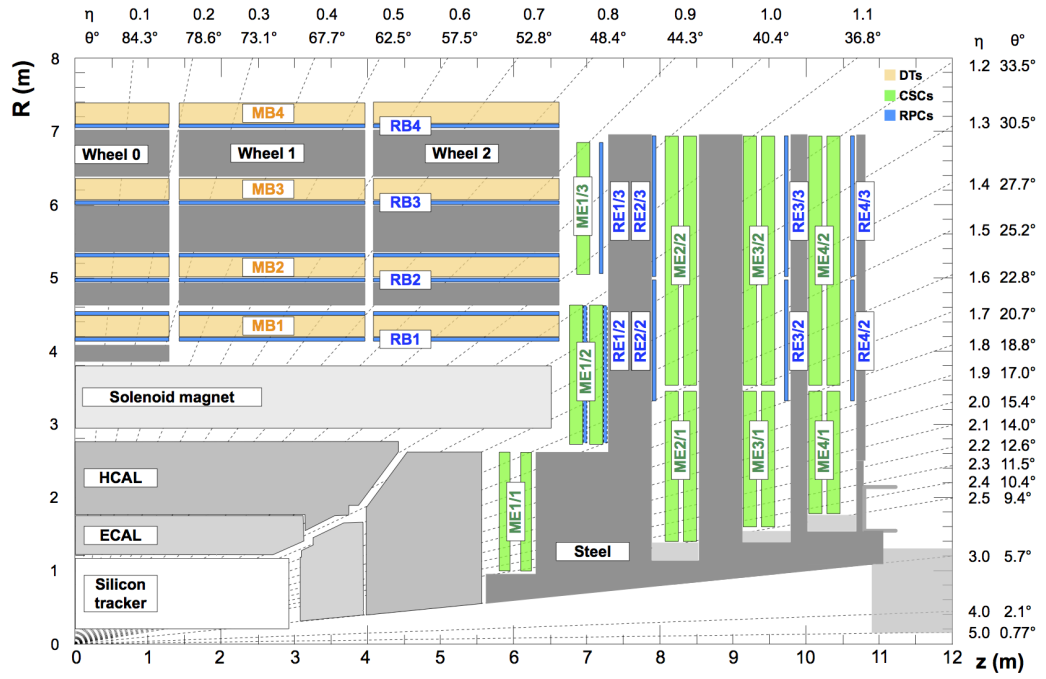
Figure 2.7: An *R-z* cross section of a quadrant of the CMS detector with the axis parallel to the beam (*z*) running horizontally and the radius (*R*) increasing upward. The IP is at the lower left corner. The locations of the various muon stations and the steel disks (dark grey areas) are shown. The DTs stations, in light orange, are labeled "MB" (muon barrel) and the CSCs, in green, are labeled "ME" (muon endcap). RPCs, in blue, are mounted in both the barrel and the endcaps of CMS, where they are labeled "RB" and "RE", respectively.

and the inner extent of the magnet coil ($R = 2.95$ m). This constrains the total amount of material which can be put in to absorb the hadronic shower. Therefore, an outer hadron calorimeter is placed outside the solenoid complementing the barrel calorimeter. Beyond $|\eta| = 3$, the forward hadron calorimeters placed at 11.2 m from the IP extend the pseudorapidity coverage down to $|\eta| = 5.2$.

The hadron barrel (HB) part of HCAL consists of thirty-two towers covering the pseudorapidity region $-1.4 < |\eta| < 1.4$. The HB is constructed in two half barrels.

The hadron outer (HO) detector contains scintillators with a thickness of 10 mm, which line the outside of the outer vacuum tank of the coil and cover the region $-1.26 < |\eta| < 1.26$. They increase the effective thickness of the hadron calorimetry to over ten interaction lengths, thus reducing the tails in the energy resolution function. The HO is physically located inside the barrel muon system and is hence constrained by the geometry and construction of that system.

Each hadron endcap (HE) of HCAL consists of fourteen η towers, covering the pseudorapidity region $1.3 < |\eta| < 3.0$.

Coverage between pseudorapidities of $3.0 < |\eta| < 5.0$ is provided by the steel/quartz fibre hadron forward (HF) calorimeter. Because the neutral component of the hadron shower is preferentially sampled in the HF technology, this design leads to narrower and shorter hadronic showers and hence is ideally suited for the congested environment in the forward region. The front face is located at 11.2 m from the IP. The depth of the absorber is 1.65 m. The signal originates from Cerenkov light emitted in the quartz fibres, which is then channelled by the fibres to photomultipliers.

2.2.3 ECAL

It is well-known that accelerated charges radiate, thus lose, energy. On the other hand, sensitivity to acceleration is inversely proportional to the inertial

mass of bodies. Electrons are the lightest free charged particles: when they penetrate the intense electric fields keeping nuclei and (orbital) electrons tightly bounded in matter, they start undergoing "pushes" which deflect them from rectilinear trajectories and as a result they radiate energy and slow down. This emitted radiation is named "bremsstrahlung". As observed in figure 2.8, from certain speed on —the high energy physics regime included—, this constitutes the main mechanism of energy loss for electrons (the same applies to positrons).
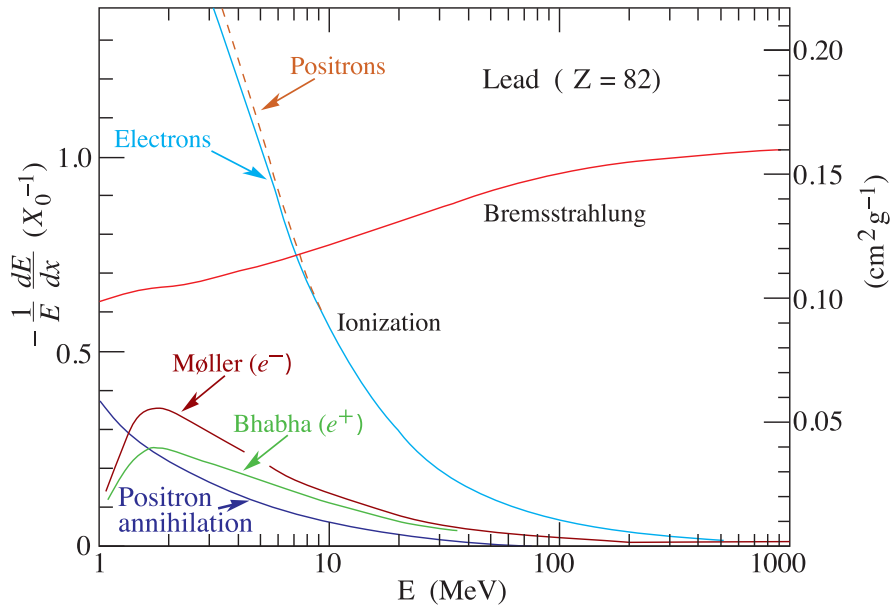
Figure 2.8: Fractional energy loss per radiation length in lead as a function of electron or positron energy. Electron (positron) scattering is considered as ionisation when the energy loss per collision is below 0.255 MeV, and as Møller (Bhabha) scattering when it is above. Ionisation losses decrease logarithmically with E whereas bremsstrahlung increases linearly. From [28].

When matter and antimatter encounter each other, they annihilate into light. The other way around is also true: 1-MeV-above photons can give rise to electron-positron pairs, but only if they travel through atoms.[5] This is indeed the leading mechanism for which high energy photons truly interact with

_____

[5]Pair production in free space, i.e. $\gamma \rightarrow e^+ e^-$, cannot satisfy energy-momentum conservation.

matter, figure 2.9.

Figure 2.9: Photon total cross sections as a function of energy in lead, showing the contributions of different processe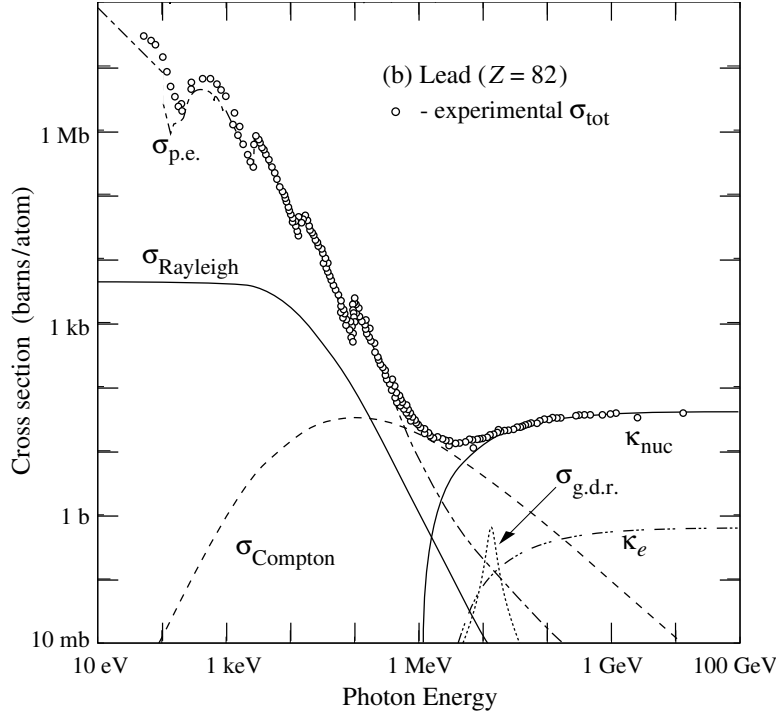s: $\sigma_{\text{p.e.}}$: atomic photoelectric effect; σ_{Rayleigh}: elastic scattering; σ_{Compton}: inelastic scattering; κ_{nuc}: pair production, nuclear field; κ_{e}, pair production, electron field; $\sigma_{\text{g.d.r.}}$: photonuclear interactions, most notably the giant dipole resonance. From [28].

When either an energetic electron or photon enters a relatively thick absorber, it initiates an electromagnetic cascade insomuch as bremsstrahlung and pair production create more photons and electrons/positrons with lower energy. Electron energies fall below the critical energy —the one for which ionisation and bremsstrahlung are equally likely— and they exhaust the remaining by ionisation and excitation rather than by the generation of more shower particles. Light arising from this relatively mild interactions is what is eventually recorded.

The ECAL is an hermetic, homogeneous calorimeter comprising almost seventy thousand lead wolframate ($PbWO_4$) crystals mounted in the central

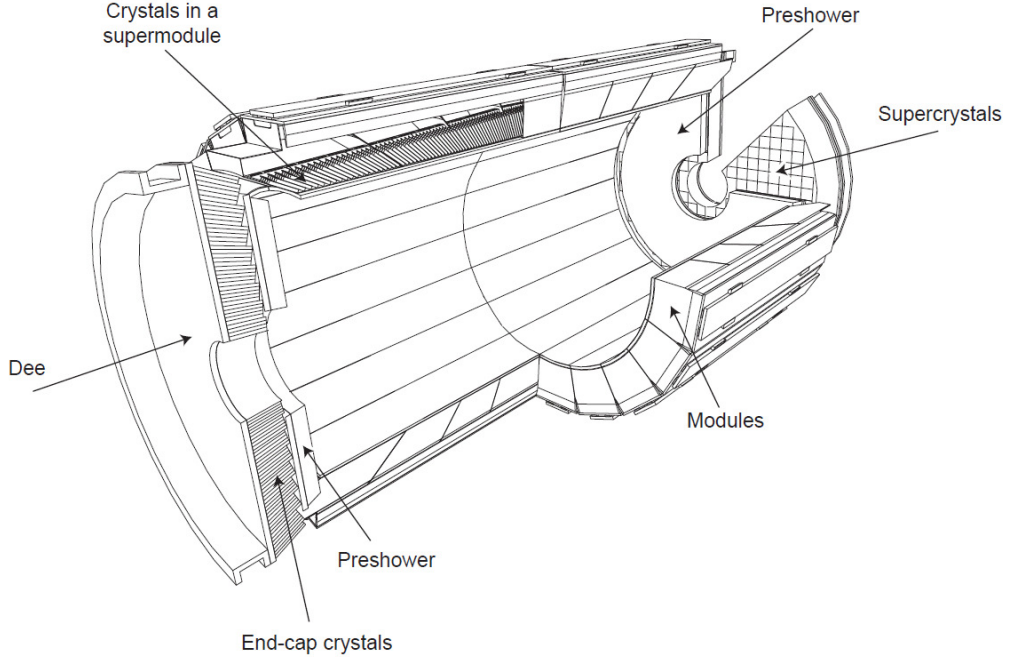barrel part and in each of the two endcaps, see figure 2.10.

Figure 2.10: Schematic view of the ECAL subdetector.

The PbWO$_4$ scintillating crystals have short radiation[6] and Molière lengths[7] ($X_0 = 0.89$ cm and $R_{\mathrm{M}} = 2.2$ cm, respectively), are fast (80% of the light is emitted within 25 ns) and radiation hard (up to 10 Mrad). However, the relatively low light yield (30 γ/MeV) requires the use of photodetectors with intrinsic gain that can operate in a magnetic field. Silicon avalanche photodiodes (APDs) are used as photodetectors in the barrel and vacuum phototriodes (VPTs) in the endcaps. In addition, the sensitivity of both the

_____

[6]Radiation length is defined as the distance in which the energy of an electron is reduced by a factor of $\frac{1}{e}$ due to bremsstrahlung. This definition is only meaningful for energies above that one at which the loss through ionisation equals the loss through bremsstrahlung. It is a characteristic constant of a material. It is also defined as $\frac{7}{9}$ of the mean free path for pair production by a high-energy photon.

[7]Molière radius is a measure of the transversal deviation of an electron with the critical energy (loss through ionisation equals the loss through bremsstrahlung) after traversing one radiation length. It is a characteristic constant of a material. It gives the scale of the transverse dimension of the fully contained electromagnetic shower initiated by an incident high energy electron or photon.

crystals and the APD response to temperature changes requires a temperature stability (~ 0.1 °C). In conclusion, the use of $PbWO_4$ crystals allowed the design of a compact calorimeter inside the solenoid that is fast, has fine granularity, and is radiation resistant.

2.2.4   Tracker

The inner tracking system of CMS is designed to provide a precise and efficient measurement of the trajectories of charged particles emerging from the LHC collisions as well as a precise reconstruction of secondary vertices. It surrounds the IP and has a length of 5.8 m and a diameter of 2.5 m, see figure 2.11. The CMS solenoid provides an homogeneous magnetic field of 4 T over the full volume of the tracker.

At the LHC design luminosity of 10^{34} cm^2 s^{-1} there will be about a thousand particles from more than twenty overlapping proton-proton interactions traversing the tracker for each bunch crossing, i.e. every 25 ns. Therefore a detector technology featuring high granularity and fast response is required, so that the trajectories can be identified reliably and attributed to the correct bunch crossing. However, these features imply a high power density of the on-detector electronics which in turn requires efficient cooling. This is in direct conflict with the aim of keeping to the minimum the amount of material in order to limit multiple scattering, bremsstrahlung, photon conversion and nuclear interactions. A compromise had to be found in this respect. The intense particle flux is expected to cause severe radiation damage to the tracking system. The main challenge in the design of the tracking system was to develop detector components able to operate in this harsh environment for an expected lifetime of ten years.

These requirements on granularity, speed and radiation hardness lead to a tracker design entirely based on silicon detector technology. The CMS tracker is composed of a pixel detector with three barrel layers at radii between 4.4 cm and 10.2 cm and a silicon strip tracker with ten barrel detection layers extending outwards to a radius of 1.1 m, see figure 2.11. Each system is

completed by endcaps which consist of two disks in the pixel detector and three plus nine disks in the strip tracker on each side of the barrel, extending the acceptance of the tracker up to a pseudorapidity of $|\eta| < 2.5$. With about 200 m^2 of active silicon area, the CMS tracker is the largest silicon tracker ever built.
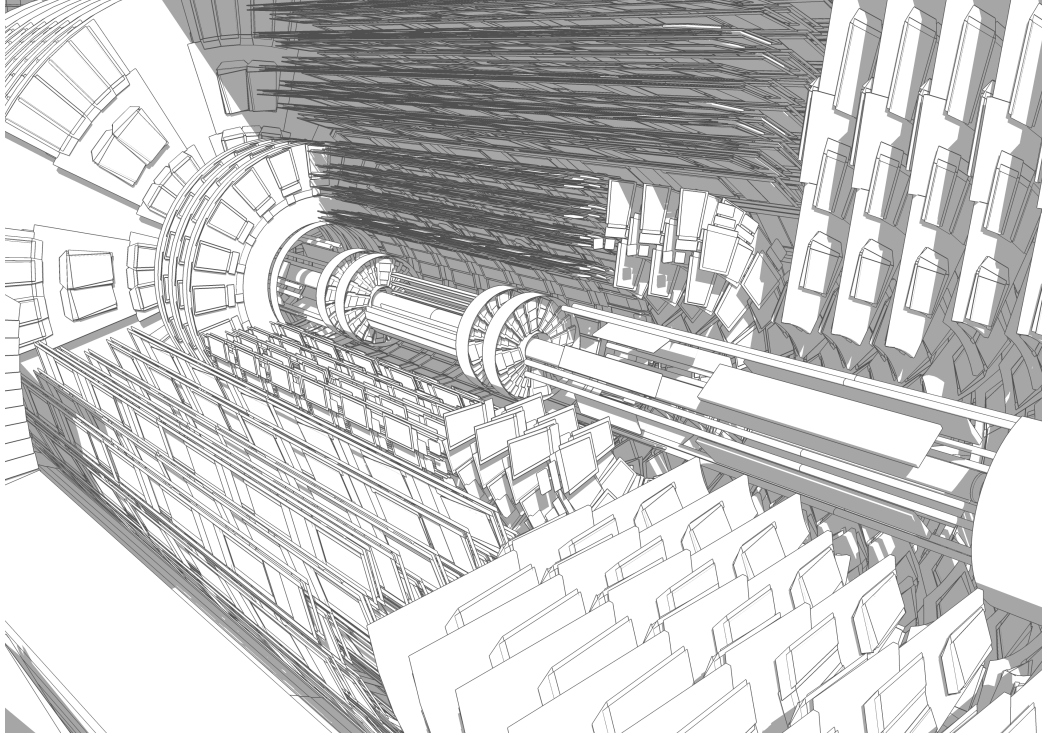
Figure 2.11: Schematic view of the tracker.

2.2.5   Trigger

The LHC provides proton-proton and heavy-ion collisions at high interaction rates. For protons the beam crossing interval is 25 ns, corresponding to a crossing frequency of 40 MHz. Depending on the luminosity, several collisions occur at each crossing of the proton bunches (approximately 20 simultaneous proton-proton collisions at the nominal design luminosity of 10^{34} cm^2 s^{-1}). Since it is impossible to store and process the large amount of data associated with the resulting high number of events, a drastic rate reduction has

to be achieved. This task is performed by the trigger system, which is the start of the physics event selection process. The rate is reduced in two steps called level-1 (L1) trigger [80] and high-level trigger (HLT) [81], respectively. The L1 trigger consists of custom-designed, largely programmable electronics, whereas the HLT is a software system implemented in a filter farm of about one thousand commercial processors. The rate reduction capability is designed to be at least a factor of 10^6 for the combined L1 trigger and HLT. The design output rate limit of the L1 trigger is 100 kHz, which translates in practice to a calculated maximal output rate of 30 kHz, assuming an approximate safety factor of three. The L1 trigger uses coarsely segmented data from the calorimeters and the muon system, while holding the high-resolution data in pipelined memories in the front-end electronics. The HLT has access to the complete read-out data and can therefore perform complex calculations similar to those made in the the analysis off-line software if required for specially interesting events.

The L1 trigger has local, regional and global components. At the bottom end, the local triggers, also called trigger primitive generators (TPG), are based on energy deposits in calorimeter trigger towers and track segments or hit patterns in muon chambers, respectively. Regional triggers combine their information and use pattern logic to determine ranked and sorted trigger objects such as electron or muon candidates in limited spatial regions. The rank is determined as a function of energy or momentum and quality, which reflects the level of confidence attributed to the L1 parameter measurements, based on detailed knowledge of the detectors and trigger electronics and on the amount of information available. The global calorimeter and global muon triggers determine the highest-rank calorimeter and muon objects across the entire experiment and transfer them to the global trigger, the top entity of the L1 hierarchy. The latter takes the decision to reject an event or to accept it for further evaluation by the HLT. The decision is based on algorithm calculations and on the readiness of the subdetectors and the data acquisition (DAQ), which is determined by the trigger control system (TCS). The level-1 accept (L1A) decision is communicated to the subdetectors through the timing, trigger and control (TTC) system. The architecture of the L1 trigger

is depicted in figure 2.12. The L1 trigger has to analyse every bunch crossing. The allowed L1 trigger latency, between a given bunch crossing and the distribution of the trigger decision to the detector front-end electronics, is 3.2 ms. The processing must therefore be pipelined in order to enable a quasi-deadtime-free operation. The L1 trigger electronics is housed partly on the detectors, partly in the underground control room located at a distance of approximately 90 m from the experimental cavern.
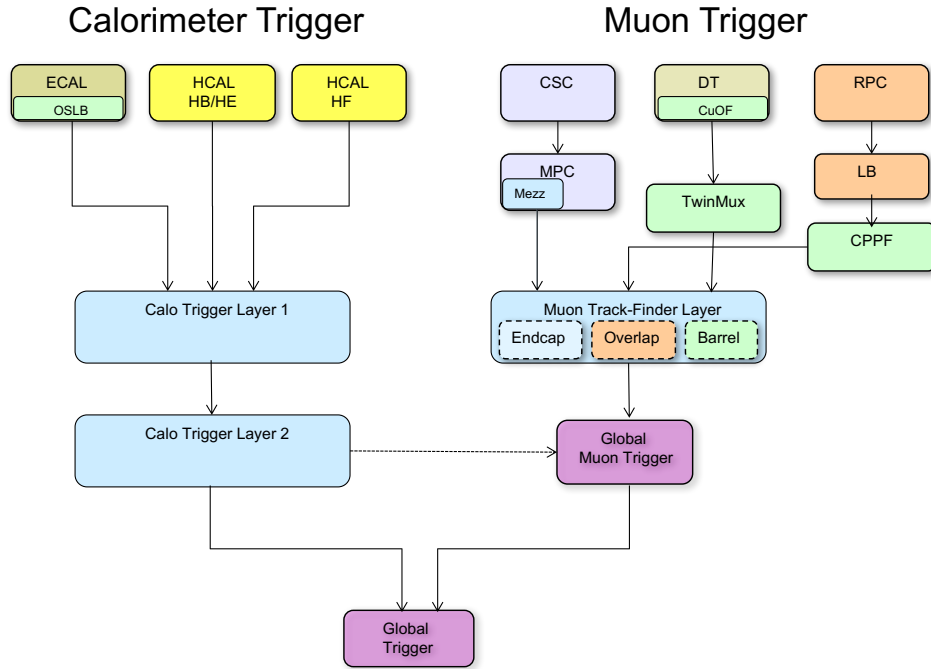

Figure 2.12: Architecture of the Level-1 trigger.

2.2.6 Data aquisition

As stated in the first paragraph of the previous section, the L1 trigger is designed to reduce the incoming average data rate to a maximum of 100 kHz. Therefore, the DAQ system must sustain a maximum input rate of 100 kHz, for a data flow of $\approx$ 100 GByte/s coming from approximately 650 data

sources, and must provide enough computing power for a software filter system, the HLT, to reduce the rate of stored events by a factor of 10^3.

The functionality of the CMS DAQ/HLT system is three-fold:

- perform the readout of the front-end electronics after a L1 trigger accept;

- execute physics selection algorithms on the events read out, in order to accept the ones with the most interesting physics content;

- forward these accepted events, as well as a small sample of the rejected events, to the online services which monitor the performance of the detector and also provide the means of archiving the events in mass storage.

Another crucial function of the DAQ system is the operation of a detector control system (DCS) for the operation and supervision of all detector components and the general infrastructure of the experiment. The DCS is a key element for the operation of CMS, and guarantees its safe operation to obtain high-quality physics data.

The architecture of the CMS DAQ system is shown schematically in figure 2.13.
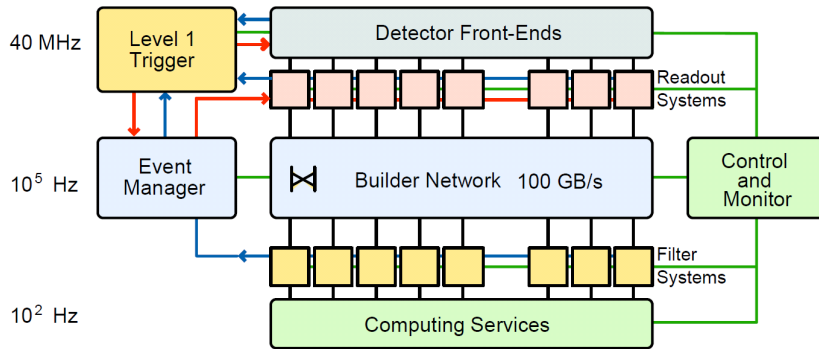
Figure 2.13: Architecture of the DAQ system.

Chapter 3

Object reconstruction

Notwithstanding that just one out of 10^6 bunch crossings is saved, this includes some tens of proton-proton collisions, phenomenon known as "pile-up", see figure 3.1. It is extremely unlikely for more than one of these to
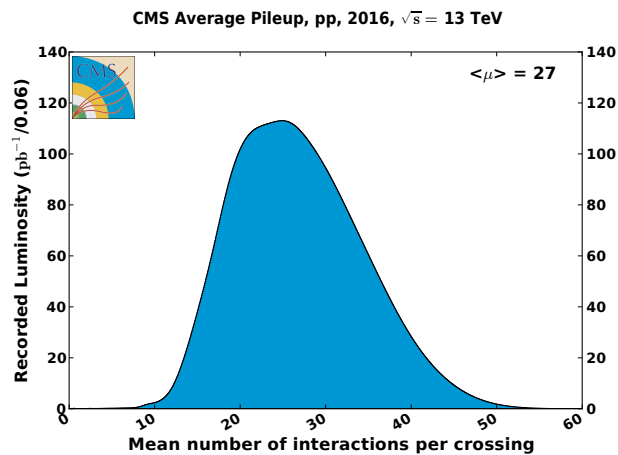
Figure 3.1: Mean number of interactions per bunch crossing for the 2016 proton-proton run at 13 TeV. From [82].

be interesting; however, every CMS snapshot brings an overwhelmingly enmeshed collection of tracks. Thus, firstly, one needs to assemble tracks to reconstruct vertices; secondly, choose the most interesting one, named "primary vertex" (PV); and thirdly, reconstruct all the objects originating from

it in a faithful way to describe the event. The first two steps are thoroughly documented in [83]. This chapter is principally devoted to explain the third one.

3.1 The Particle Flow technique

For the first time in hadron colliders, the CMS experiment makes use of a "particle flow" (PF) algorithm to reconstruct all particles coming from a proton-proton collision [84]. The distinctive characteristic of the PF technique lies in combining information from the different subdetectors, instead of dealing with each independently. In the CMS case, this is essentially doable thanks to the high-grade performance of the tracker and the ECAL in terms of spatial resolution.

Ingredients going into the PF are "tracks", fitted from hits in the tracker and the muon system, and "clusters", gathered from energy deposits in the calorimeters by dedicated algorithms. The core of the PF consists in linking nearby tracks and clusters to obtain the most comprehensive record of one of the following objects: muon, electron, photon, proton, charged pion, charged kaon, long-lived neutral kaon and neutron.

A more detailed description of the procedure is given below for the relevant objects used by this search, namely, muons, electrons, jets (mainly b-jets) and missing transverse energy, the latter two derived from those enumerated in the previous paragraph as it will be explained.

3.1.1 Muons

As pointed out in the previous chapter, whereas the muon system grants a highly efficient identification of muons, the inner tracker allows a high-resolution measurement of their momentum. A muon object may be reconstructed in some of the following modes [79]:

- standalone muon: track formed just from hits in the muon system,

- global muon: the track above matches with another one in the inner tracker,

- tracker muon: conversely, an inner track seeks to match its counterpart in the muon system.

A PF muon itself is defined from the second category, adding an advanced casuistic which must be verified:

Isolated global muons are first selected by considering additional inner tracks and calorimeter energy deposits within a distance $\Delta R = \sqrt{(\Delta\eta)^2 + (\Delta\phi)^2}$ to the muon lower than 0.3. The sum of the p_{T} of the tracks plus the E_{T} of the deposits must not exceed 10% of the muon p_{T}. This isolation criterion alone is sufficient to adequately reject hadrons that would be misidentified as muons, hence no further selection is applied to these muon candidates.

For non-isolated global muons, a stricter selection, whose specifications are listed in table 3.1, is applied. In addition, it is required either that at least three matching track segments are found in the muon system or that the calorimeter deposits associated with the track to be compatible with the muon hypothesis.

The muon momentum is chosen to be that of the inner track if its p_{T} is smaller than 200 GeV. Above this value, the momentum is assigned according to the lowest χ^2 probability from different track fits, i.e. going outwards, inwards, disregarding some layer of the muon system, etc.

The PF elements which make up these identified muons are masked against further processing, that is, they are discarded as ingredients for subsequent particles.

---

[1]Defined as the distance of closest approach of the track to the PV in the xy plane.

3.1.2 Electrons

Electron reconstruction exploits the fact that any energetic-enough candidate: a) extinguishes through an electromagnetic shower in the ECAL, b) if kicked off by the tracker material, it emits bremsstrahlung photons which also terminate in the ECAL, and c) is bent by the solenoid magnetic field, while leaving marks of its passage in the tracker.

With all of this, PF constructs clusters and tracks, links ones to others ensuring compatibility, and assesses the quality of the candidate by looking through the following groups of variables [85]:

- Observables that compare measurements obtained from the ECAL and the tracker (track-cluster matching, including both geometrical and cluster energy-track momentum matching).

- Purely calorimetric observables used to separate genuine electrons from misidentified electrons. They are based on the transverse shape of electromagnetic showers in the ECAL and take advantage of the fact that electromagnetic showers are narrower than hadronic showers:

  - $\dfrac{E_{\mathrm{HCAL}}}{E_{\mathrm{ECAL}}}$: ratio of energy deposited in the HCAL versus the ECAL;

  - $\dfrac{1}{E_{\mathrm{SC}}} - \dfrac{1}{p}$: E_{SC} is the supercluster (main concentration of clusters) energy and p is the track momentum at the point of closest approach to the PV;

variable	requirement
normalised χ^2 of the track fit	< 10
muon chamber hits included in the fit	≥ 1
is it also a "tracker muon"?	yes
tracker hits	≥ 10
pixel hits	≥ 1
transverse impact parameter[1]	< 2 mm

Table 3.1: Muon "tight" selection as defined in [79].

○ $\sigma_{\eta\eta}$: the root mean square of the energy deposited within the supercluster along η;

○ $\Delta\eta$: difference in η between the supercluster position and the inner track extrapolated from the PV; and

○ $\Delta\phi$: difference in ϕ between the supercluster position and the inner track extrapolated from the PV.

• Tracking observables employed to improve the separation between electrons and charged hadrons, exploiting the information obtained from the fitted tracks.

All tracks and clusters used to reconstruct electrons are masked against further processing.

3.1.3   Jets

Quarks are gregarious. When one of them, energetic enough, tries to emancipate, it is promptly surrounded by new fellows created at the expense of its energy, which in turn try to emancipate as well. The chain continues until quarks have sufficiently low energy to associate themselves in colour-neutral objects: hadrons. The entire process is referred to as "hadronization" or "fragmentation". Hadrons decay to stable individuals if they are not,[2] travel collimated —hence the name of "jets"—, and are seen by detectors and reconstructed by the PF.

A dedicated tool, the anti-k_t algorithm [86], clusters these hadrons, either charged or neutral, together with possible non-isolated photons as well as unmasked muons or electrons, to compute the energy and direction of the original quark as carefully as possible, see figure 3.2. To do that, any of the above-mentioned candidates, with transverse momentum $p_{\mathrm{T}\,i}$, is merged to another one or to an incipient jet with transverse momentum $p_{\mathrm{T}\,j}$ if it verifies

---

[2]All the stable hadrons are: the proton, the neutron, the $\pi^{\pm}$, the $K^{\pm}$ and the K^0_{S}.

the condition:

$$\min\left(\frac{1}{p_{\mathrm{T}i}^2}, \frac{1}{p_{\mathrm{T}j}^2}\right)\frac{\Delta R}{R} < \frac{1}{p_{\mathrm{T}i}^2}, \tag{3.1}$$

where $\Delta R = \sqrt{(\eta_i - \eta_j)^2 + (\phi_i - \phi_j)^2}$, and R, indicating the size of the jet, is chosen to be 0.4. On average, 65% of the jet energy is carried by charged hadrons, 25% by photons, and 10% by neutral hadrons.
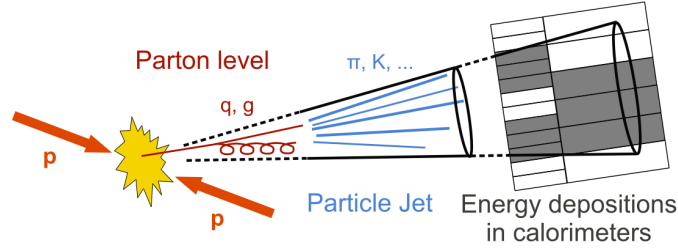
Figure 3.2: Sketch of a proton-proton collision and the development of a jet.

b-tagging

Jets arising from b quarks are fairly interesting per se: they could be rests from top quarks —as it happens in this search—, from Higgs bosons, or from unknown particles. Thus, being able to identify b-jets is tremendously helpful for dealing with certain processes.

The algorithm to do this is based on long lifetimes of b-hadrons, which give rise to displaced tracks from which a secondary vertex may be reconstructed, as shown in figure 3.3.

In addition, b quarks have a larger mass and harder fragmentation compared to the light quarks. As a result, the decay products of the b-hadrons have, on average, a larger p_{T} relative to the jet axis than the other jet constituents. Furthermore, in approximately 20% of the cases, a muon or electron is present in the decay chain. Thus, apart from the properties of the reconstructed secondary vertex or displaced tracks, the presence of charged leptons is also exploited for b-tagging techniques [87].
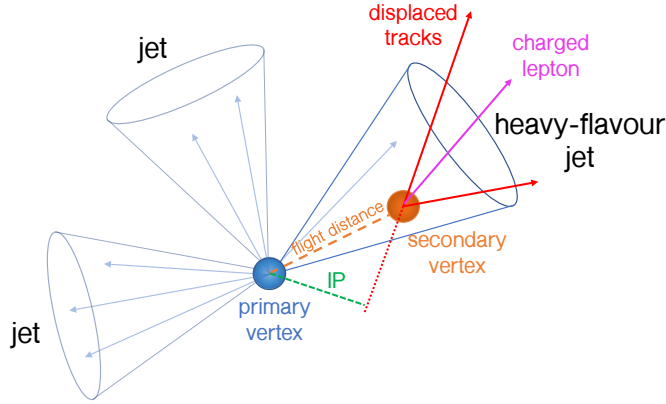
Figure 3.3: b-jet with a secondary vertex from the decay of a b-hadron resulting in charged-particle tracks (including possibly a soft lepton) that are displaced with respect to the primary interaction vertex, and hence with a large impact parameter value. From [87].

3.1.4 MET

Interactions between particles and detectors occur via electromagnetic and strong forces. This means that neutrinos, only sensitive to the weak force, escape unseen. The same behaviour is expected for quite a few theory-driven, not evidenced yet particles, DM candidates among them. Inferring their presence is however realisable up to some grade in experiments performed with accelerators. Since initial conditions are under control —momentum in the transverse plane to the beam is null—, by applying momentum conservation one can account for the joint, transverse momentum of all undetectable particles produced in the collision, $\vec{p}_{\mathrm{T}}^{\mathrm{undetect}}$:

$$\vec{0} = \sum_{i}^{\mathrm{detectable}} \vec{p}_{\mathrm{T}\,i} + \vec{p}_{\mathrm{T}}^{\mathrm{undetect}}, \tag{3.2}$$

The vector $\vec{p}_{\mathrm{T}}^{\mathrm{undetect}}$, most commonly represented by $\vec{E}_{\mathrm{T}}^{\mathrm{miss}}$, is called the missing transverse energy (MET) .

Unfortunately, detection is not perfect. Objects entering the first term of the right-hand side of equation (3.2), namely, muons, electrons, taus, pho-

tons and jets, are reconstructed not hundred per cent accurately; their energy is measured with limited resolution; some of them may be due to pile-up collisions, adulterating the calculation; etc. A significant improvement comes when taking into account the energy corrections applied to jets and recomputing the MET as:

$$\vec{E}_{\mathrm{T}}^{\mathrm{miss\ corr}} = \vec{E}_{\mathrm{T}}^{\mathrm{miss}} - \sum_{\mathrm{jet}} \left(\vec{p}_{\mathrm{T\,jet}}^{\mathrm{\,corr}} - \vec{p}_{\mathrm{T\,jet}} \right) , \qquad (3.3)$$

where the superscript "corr" refers to corrected quantities. $\vec{E}_{\mathrm{T}}^{\mathrm{miss\ corr}}$ is known as "Type-1-corrected" $E_{\mathrm{T}}^{\mathrm{miss}}$.

Apart from the uncertainties associated to the ingredients entering in $\sum_i^{\mathrm{detectable}} \vec{p}_{\mathrm{T}\,i}$, propagated to the MET object accordingly, another important source of uncertainty is that coming from the energy deposits not assigned to any object, the so-called "unclustered energy".

Chapter 4

Data and event selection

This chapter starts the $t\bar{t} + \mathrm{DM}$ search itself. It might be convenient to remember its signature again: every dileptonic $t\bar{t}+\mathrm{DM}$ event is characterised by two opposite-charge leptons (electrons and/or muons), two b-jets as well as a significant amount of $E_\mathrm{T}^\mathrm{miss}$. First, section 4.1 presents the data together with the Monte Carlo (MC) simulations and their generation parameters. Second, section 4.2 explains the preliminary selection, which aims at reducing the most evident background processes. The specific work carried out here has been the gathering and organisation of all the data and MC simulations; the care on applying the opportune corrections to the latter; and, above all, the verification of the appropriateness of the event selection, decidedly $t\bar{t}$ oriented.

4.1   Data and simulated samples

The search has been performed by using the CMS event data model [88] and the official software framework, denoted as "CMSSW", version 8.0, for event generation, simulation and reconstruction. As many other analyses within the CMS collaboration, this one uses the "Mini-AOD" analysis object format [89], from which an analysis software have been developed in order to operate

in a more targeted way. In effect, imported samples in Mini-AOD format have been privately reduced in two stages: first, medium-size ntuples were processed at our supercomputing center from which lighter ones were slimmed thanks to C++ dedicated scripts working within the ROOT package [90]. I have taken the whole responsibility for the latter step; furthermore, I have importantly contributed to the former.

This search has followed a blinding procedure in which signal regions were defined and frozen before having a look at the whole data. The background prediction methods have been applied and tested however on the full 2016 luminosity from the very beginning.

Data and simulated samples are described in the following.

4.1.1   Description of data samples

The data sets collected during the full LHC 2016 run at $\sqrt{s} = 13$ TeV are listed in table 4.1. They were gathered by combining a series of single and double lepton triggers according to certain logic rules. More will be said in section 4.2. From these, certified runs[1] are selected by applying the certified good-run lists as given in [91]. The total integrated luminosity corresponds to $\mathcal{L} = 35.9 \pm 0.9$ fb^{-1} [92].

4.1.2   Description of MC samples

The background processes considered in this search are: $t\bar{t}$, $t\bar{t}$ in association with W, $t\bar{t}$ plus Z, single top (tW), $Z/\gamma^\star$ (also known as Drell-Yan, abbreviated "DY"), dibosons (WW, WZ, ZZ), and tribosons (WWW, WWZ, WZZ and ZZZ). The list of their MC samples used is given in table 4.2.

The default POWHEG (v2) [93] setup with the damping parameter turned on (hdamp = 172.5 GeV) is used to simulate the main background, $t\bar{t}$, its model

---

[1] "Certified" means that data were taken in suited conditions in respect of detector and trigger performance as well as object reconstruction.

data set	no. of events	$\mathcal{L}$ [fb^{-1}]
/SingleMuon/Run2016B-03Feb2017_ver2-v2/MINIAOD	158145722	
/SingleElectron/Run2016B-03Feb2017_ver2-v2/MINIAOD	246440440	
/MuonEG/Run2016B-03Feb2017_ver2-v2/MINIAOD	32727796	5.78
/DoubleMuon/Run2016B-03Feb2017_ver2-v2/MINIAOD	82535526	
/DoubleEG/Run2016B-03Feb2017_ver2-v2/MINIAOD	143073268	
/SingleMuon/Run2016C-03Feb2017-v1/MINIAOD	67441308	
/SingleElectron/Run2016C-03Feb2017-v1/MINIAOD	97259854	
/MuonEG/Run2016C-03Feb2017-v1/MINIAOD	15405678	2.56
/DoubleMuon/Run2016C-03Feb2017-v1/MINIAOD	27934629	
/DoubleEG/Run2016C-03Feb2017-v1/MINIAOD	47677856	
/SingleMuon/Run2016D-03Feb2017-v1/MINIAOD	98017996	
/SingleElectron/Run2016D-03Feb2017-v1/MINIAOD	148167727	
/MuonEG/Run2016D-03Feb2017-v1/MINIAOD	23482352	4.25
/DoubleMuon/Run2016D-03Feb2017-v1/MINIAOD	33861745	
/DoubleEG/Run2016D-03Feb2017-v1/MINIAOD	53324960	
/SingleMuon/Run2016E-03Feb2017-v1/MINIAOD	90963495	
/SingleElectron/Run2016E-03Feb2017-v1/MINIAOD	117321545	
/MuonEG/Run2016E-03Feb2017-v1/MINIAOD	22519303	4.01
/DoubleMuon/Run2016E-03Feb2017-v1/MINIAOD	28246946	
/DoubleEG/Run2016E-03Feb2017-v1/MINIAOD	49877710	
/SingleMuon/Run2016F-03Feb2017-v1/MINIAOD	65489554	
/SingleElectron/Run2016F-03Feb2017-v1/MINIAOD	70593532	
/MuonEG/Run2016F-03Feb2017-v1/MINIAOD	16002165	3.10
/DoubleMuon/Run2016F-03Feb2017-v1/MINIAOD	20329921	
/DoubleEG/Run2016F-03Feb2017-v1/MINIAOD	34577629	
/SingleMuon/Run2016G-03Feb2017-v1/MINIAOD	149916849	
/SingleElectron/Run2016G-03Feb2017-v1/MINIAOD	153330123	
/MuonEG/Run2016G-03Feb2017-v1/MINIAOD	33854612	7.54
/DoubleMuon/Run2016G-03Feb2017-v1/MINIAOD	45235604	
/DoubleEG/Run2016G-03Feb2017-v1/MINIAOD	78764716	
/SingleMuon/Run2016H-03Feb2017_ver2-v1/MINIAOD	169642135	
/SingleElectron/Run2016H-03Feb2017_ver2-v1/MINIAOD	125826667	
/MuonEG/Run2016H-03Feb2017_ver2-v1/MINIAOD	28466022	8.39
/DoubleMuon/Run2016H-03Feb2017_ver2-v1/MINIAOD	47693168	
/DoubleEG/Run2016H-03Feb2017_ver2-v1/MINIAOD	83361083	
/SingleMuon/Run2016H-03Feb2017_ver3-v1/MINIAOD	4393029	
/SingleElectron/Run2016H-03Feb2017_ver3-v1/MINIAOD	3191585	
/MuonEG/Run2016H-03Feb2017_ver3-v1/MINIAOD	770494	0.22
/DoubleMuon/Run2016H-03Feb2017_ver3-v1/MINIAOD	1219644	
/DoubleEG/Run2016H-03Feb2017_ver3-v1/MINIAOD	2027651	

Table 4.1: Collision data samples used in the search.

sample	cross section [pb]	no. of events
TTTo2L2Nu_13TeV-powheg	87.31	4995600
ST_tW_top_5f_inclusiveDecays_13TeV-powheg-pythia8_TuneCUETP8M1	35.6	1000000
ST_tW_antitop_5f_inclusiveDecays_13TeV-powheg-pythia8_TuneCUETP8M1	35.6	999400
WWTo2L2Nu_13TeV-powheg	12.178	1979988
WZTo3LNu_TuneCUETP8M1_13TeV-powheg-pythia8	4.42965	2000000
ZZTo4L_13TeV_powheg_pythia8	1.212	6669188
ZZTo2L2Nu_13TeV_powheg_pythia8	0.564	8785050
ZZTo2L2Q_13TeV_amcatnloFXFX_madspin_pythia8	3.22	15301695
WWW_4F_TuneCUETP8M1_13TeV-amcatnlo-pythia8	0.18331	240000
WWZ_TuneCUETP8M1_13TeV-amcatnlo-pythia8	0.16510	250000
WZZ_TuneCUETP8M1_13TeV-amcatnlo-pythia8	0.01398	246800
ZZZ_TuneCUETP8M1_13TeV-amcatnlo-pythia8	0.05565	249237
DYJetsToLL_M-10to50_TuneCUETP8M1_13TeV-amcatnloFXFX-pythia8	18610	30899063
DYJetsToLL_M-50_TuneCUETP8M1_13TeV-amcatnloFXFX-pythia8	6025.2	28751199
TTWJetsToLNu_TuneCUETP8M1_13TeV-amcatnloFXFX-pythia8	0.2043	252673
TTWJetsToQQ_TuneCUETP8M1_13TeV-amcatnloFXFX-pythia8	0.4062	833298
TTZToLLNuNu_M-10_TuneCUETP8M1_13TeV-amcatnlo-pythia8	0.2529	398600
TTZToQQ_TuneCUETP8M1_13TeV-amcatnlo-pythia8	0.5297	749400

Table 4.2: SM background samples, their production cross sections and number of generated events.

dependencies on the top quark mass, the renormalisation and factorisation scale, Q^2, and the parton distribution functions (PDFs). NNPDF3.0 [94] is used as default PDF. The $t\bar{t}$ events were showered using PYTHIA 8.2 [95, 96] with the CUETP8M2 tune [97].

Besides the $t\bar{t}$ process, other background contributions such as the single top and diboson events (WW, WZ, and ZZ) with multiple jets are directly taken from MC simulations. The single top process is simulated using POWHEG (v1) [98] with NNPDF3.0 and PYTHIA 8.2 with the CUETP8M1 tune [99, 100]. The WW, WZ, and ZZ diboson samples are produced using PYTHIA 8.2 with the CUETP8M1 tune.

The DY background samples are generated with MG5_AMC@NLO 2.2.2 [101] with NNPDF3.0 and interfaced to PYTHIA 8.2 with the CUETP8M1 tune for hadronisation. Z bosons are simulated with up to two additional partons and the FxFx [102] scheme is used for merging. The generation is then split into two distinct Z invariant mass ranges: 10-50 GeV and > 50 GeV.

It is also worth noting that in the following discussion both the $t\bar{t}+W$ and the $t\bar{t}+Z$ backgrounds will be grouped under the same general name: $t\bar{t}+$V.

Two backgrounds have been estimated using data-driven methods: the non-prompt background is estimated using a general tight-to-loose method [103], while the contribution given by the DY process is estimated thanks to the usual $R_{\text{in-out}}$ method. Both methods will be detailed in chapter 6.

For comparison with the measured distributions, the event yields in the simulated samples are normalised to the corresponding integrated luminosity and to their theoretical cross sections. These are taken from next-to-next-to-leading order (NNLO) (Z+jets), next-to-leading order (NLO) plus next-to-next-to-leading logarithm (NNLL) (single top-tW channels [104]) or NLO diboson [105]) calculations. For the simulated $t\bar{t}$ sample, the full NNLO+NNLL calculation, performed with the TOP++ 2.0 program [106], is used. The PDF and α_S uncertainties are estimated using the PDF4LHC prescription [107, 108] with the MSTW2008nnlo68cl [109], CT10 NNLO [110, 111], and NNPDF2.3 5f FFN [112] PDF sets, and added in quadrature to the

scale uncertainty to obtain a $t\bar{t}$ production cross section of 832 GeV assuming a top-quark mass value of 172.5 GeV.

Simulated events are then interfaced with a realistic model of the CMS detector using GEANT4 [113] and are reconstructed using the official CMS reconstruction algorithms.

Two simplified DM production models are considered. One where the mediator is a scalar and a second one where it is considered to be a pseudoscalar particle instead. To generate samples for these scenarios, different benchmark points are selected to represent the different kinematic features that can be obtained varying the minimal set of parameters, i.e. $\{m_\chi, m_\phi, g_\chi, g_q\}$. The simulated samples for the simplified models are generated based on the grid points listed on table 4.3 [62]. For the sample generation, the couplings of the mediator with the SM, g_q, and the DM particle, g_χ, have been considered equal to one.

4.1.3   Weights and corrections to MC samples

MC simulated events are corrected for different effects in order to improve the modelling of the data.

The samples are reweighted to match the distribution of true interactions observed in data due to multiple collisions in the same bunch crossing (pile-up). The target pile-up distribution for data is generated using the instantaneous luminosity per bunch crossing for each luminosity section, stored in the "LumiDB" database, and the total proton-proton inelastic cross section. A Poisson smearing is applied to model statistical fluctuations. The source distribution is taken from the "PileupInfo" collection which stores the true number of pile-up events mixed with the particular hard interaction process in each MC event. A variation of $\pm 5\%$ on the minimum bias cross section is used to estimate the uncertainties due to pile-up modeling [114].

Corrections to account for data-MC differences in the trigger and reconstruction of the leptons are also applied. These corrections were derived in [115]

sample	cross section [pb]	no. of events
TTbarDMJets_DiLept_scalar_Mchi-1_Mphi-10_TuneCUETP8M1_v2_13TeV-madgraphMLM-pythia8	19.590	240379
TTbarDMJets_DiLept_scalar_Mchi-1_Mphi-20_TuneCUETP8M1_v2_13TeV-madgraphMLM-pythia8	10.480	251225
TTbarDMJets_DiLept_scalar_Mchi-1_Mphi-50_TuneCUETP8M1_v2_13TeV-madgraphMLM-pythia8	2.941	253308
TTbarDMJets_DiLept_scalar_Mchi-1_Mphi-100_TuneCUETP8M1_v2_13TeV-madgraphMLM-pythia8	0.6723	257761
TTbarDMJets_DiLept_scalar_Mchi-1_Mphi-200_TuneCUETP8M1_v2_13TeV-madgraphMLM-pythia8	0.009	254295
TTbarDMJets_DiLept_scalar_Mchi-1_Mphi-300_TuneCUETP8M1_v2_13TeV-madgraphMLM-pythia8	0.0295	254030
TTbarDMJets_DiLept_scalar_Mchi-1_Mphi-500_TuneCUETP8M1_v2_13TeV-madgraphMLM-pythia8	0.005	250524
TTbarDMJets_DiLept_pseudoscalar_Mchi-1_Mphi-10_TuneCUETP8M1_v2_13TeV-madgraphMLM-pythia8	0.441	252054
TTbarDMJets_DiLept_pseudoscalar_Mchi-1_Mphi-20_TuneCUETP8M1_v2_13TeV-madgraphMLM-pythia8	0.399	249253
TTbarDMJets_DiLept_pseudoscalar_Mchi-1_Mphi-50_TuneCUETP8M1_v2_13TeV-madgraphMLM-pythia8	0.303	255516
TTbarDMJets_DiLept_pseudoscalar_Mchi-1_Mphi-100_TuneCUETP8M1_v2_13TeV-madgraphMLM-pythia8	0.1909	249971
TTbarDMJets_DiLept_pseudoscalar_Mchi-1_Mphi-200_TuneCUETP8M1_v2_13TeV-madgraphMLM-pythia8	0.0836	240536
TTbarDMJets_DiLept_pseudoscalar_Mchi-1_Mphi-300_TuneCUETP8M1_v2_13TeV-madgraphMLM-pythia8	0.0400	250250
TTbarDMJets_DiLept_pseudoscalar_Mchi-1_Mphi-500_TuneCUETP8M1_v2_13TeV-madgraphMLM-pythia8	0.0054	241952

Table 4.3: Simplified model signal samples at several grid points, their corresponding production cross sections from MADGRAPH at leading order (LO) for scalar and pseudoscalar mediator models, and number of generated events.

and account for the efficiency deviations found in the trigger, the tracking, the identification and the isolation of both muons and electrons. All of them make use of the so-called "tag and probe" method, briefly described in the next lines:

The tag and probe method makes use of a well-established mass resonance e.g. J/ψ, ϵ, or Z, to select particles of the desired type, and probe the efficiency of a particular selection criterion on them. Usually, the "tag" is an object that passes a set of very tight selection criteria designed to isolate the required particle type. A generic set of the desired particle type (i.e. with potentially very loose selection criteria) known as "probes" is selected by pairing them with tags such that the invariant mass of the combination is consistent with the mass of the resonance. The simple expression to get the efficiency is:

$$\varepsilon = \frac{N_{\text{pass}}^{\text{probe}}}{N_{\text{pass}}^{\text{probe}} + N_{\text{fail}}^{\text{probe}}} \tag{4.1}$$

The identical computation is done for both data and MC. The scale factors are the ratios of their efficiencies.

Scale factors on the lepton identification and isolation efficiencies account for around 5% for lower $|\eta|$ (barrel region) and 10% or bigger for higher $|\eta|$ [115]. Trigger efficiencies will be commented in section 4.2.

The same procedure is used to correct for differences in the b-tagging performance. The officially recommended data-to-MC scale factors [116] are applied to the simulation.

Jets are also corrected using the recommended jet energy corrections (JECs) [117]. These corrections are propagated to quantities such as $E_{\text{T}}^{\text{miss}}$.

The POWHEG top pair production sample is also reweighted to correct for a known mismodelling of the momentum of the top quark. This reweighting is carried out following the official recipe from the "Top" group [118].The effect and suitability of this correction can be appreciated in figure 4.1 in which the p_{T} spectrum of the most energetic lepton in the event is shown before and after applying the reweighting.
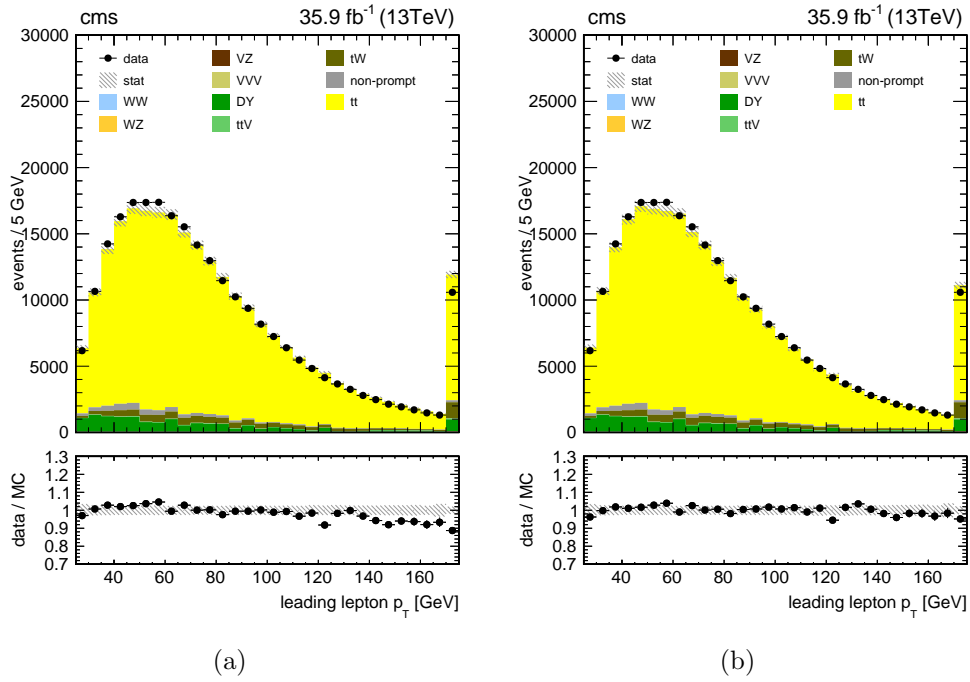
Figure 4.1: Distribution of the p_T of the most energetic lepton in the event, from 25 GeV, (a) before and (b) after applying the top p_T reweighting. The last bin includes overflow events.

4.2   Event selection

As declared in section 4.1.1, the data selection chain for this search is initiated
by the two- and one-lepton high level trigger paths merged with a logical "or"
to gain efficiency while it avoids the double counting of some events. Every
path involves lepton identification together with p_T calculation algorithms,
supplied with information from the muon system, the calorimeters and the
tracker.

Different thresholds on the p_T of the leptons are used, their values determined
by the instantaneous luminosity provided by the LHC, as well as the demands
from other trigger paths in the joint list or "menu".

Data events are required to have been accepted by one of the following double
or single lepton triggers. (The "DZ" label in the trigger names indicates the
introduction of an additional online requirement on the longitudinal distance
between the lepton and the primary vertex. It was used when the LHC
instantaneous luminosity started to grow to keep the trigger rates under the
allocated rate budget.)

- **Single Muon**

  - HLT_IsoTkMu22_v*
  - HLT_IsoMu22_v*

- **Single Electron**

  - HLT_Ele27_eta2p1_WPLoose_Gsf_v*
  - HLT_Ele45_WPLoose_Gsf_v*

- **Double EG**

  - HLT_Ele23_Ele12_CaloIdL_TrackIdL_IsoVL_DZ_v*

- **Double Muon**

  - HLT_Mu17_TrkIsoVVL_Mu8_TrkIsoVVL_v*

  ○ HLT_Mu17_TrkIsoVVL_TkMu8_TrkIsoVVL_v*

- **Muon EG**

  ○ HLT_Mu8_TrkIsoVVL_Ele23_CaloIdL_TrackIdL_IsoVL_v*

  ○ HLT_Mu23_TrkIsoVVL_Ele12_CaloIdL_TrackIdL_IsoVL_v*

As indicated in subsection 4.1.3, trigger efficiencies have been calculated with the tag and probe method in bins of p_T and η for the single lepton triggers and for each leg of the double lepton ones.

For illustrative purposes, figure 4.2 shows the efficiencies for each leg of the HLT_Ele23_Ele12_CaloIdL_TrackIdL_IsoVL_v* trigger: one can appreciate how the turn-on is shifted between both. In the end, one must combine all the individuals to get an overall efficiency by means of probability theory [115]. Typical values are greater than 97%.

This analysis uses the recommended lepton objects from the CMS-official "EGamma" and "Muon" physics object groups (POGs) ([119] and [120], respectively). In particular, muons should pass the "Muon Tight ID" criteria and electrons should pass the "Electron Tight Cut-Based ID" criteria, both of them designed to keep the amount of non-prompt leptons low.[2]

The "Muon Tight-ID" definition is constructed upon the class of PF muon (see section 3.1.1 of the previous chapter) by adding more stringent requirements, gathered in table 4.4.[3]

The "Electron Tight Cut-Based ID" definition is detailed in table 4.5. Most of the variables from the first column fit within the three categories described in section 3.1.2 of the previous chapter. Thresholds in the second and the third columns refer to the barrel ($|\eta| < 1.479$) and the endcaps ($|\eta| > 1.479$), respectively.

A significant fraction of background to isolated primary electrons is due to

---

[2] "Non-prompt" refers to those leptons which are recognised as such wrongly or come from quark hadronisation.

[3] As one can appreciate, table 4.4 is an extension of table 3.1 of chapter 3.
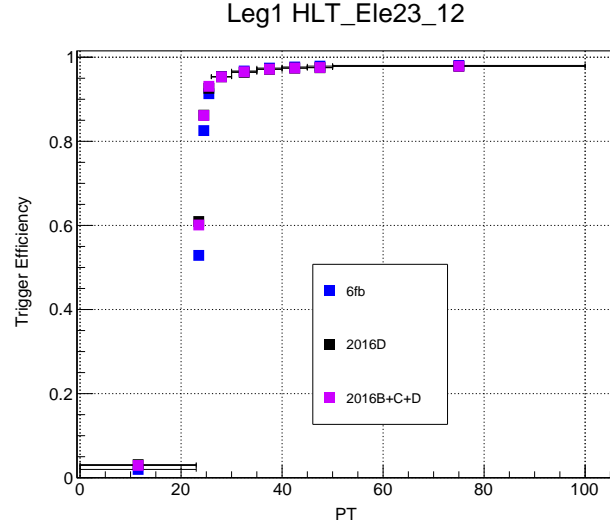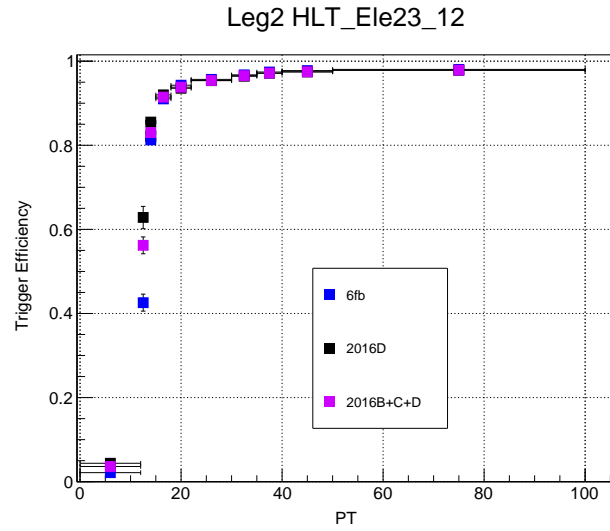
Figure 4.2: Trigger efficiencies for HLT_Ele23_Ele12_CaloIdL_TrackIdL_IsoVL_v*
triggers in bins of p_T for (a) the first leg (23 GeV part) (b) the second leg
(12 GeV part). From [115].

variable	requirement
normalised χ^2 of the track fit	< 10
muon chamber hits included in the fit	≥ 1
is it also a "tracker muon"?	yes
tracker hits	≥ 10
pixel hits	≥ 1
transverse impact parameter	< 2 mm
z distance of the track w.r.t. the PV	< 5 mm
tracker layers with hits	> 5

Table 4.4: "Muon Tight-ID" selection as defined in [119].

misidentified jets or to genuine electrons within a jet resulting from semileptonic decays of b or c quarks. In both cases, the electron candidates have significant energy flow near their trajectories, and requiring electrons to be isolated from such nearby activity greatly reduces these sources of background. That is done by considering additional inner tracks and calorimeter energy deposits within a distance $\Delta R = \sqrt{(\Delta\eta)^2 + (\Delta\phi)^2}$ to the electron lower than 0.3. The sum of the p_{T} of the tracks plus the E_{T} of the deposits must not exceed the corresponding values on table 4.5 with respect to the electron p_{T}.

variable	requirement	
$\dfrac{E_{\mathrm{HCAL}}}{E_{\mathrm{ECAL}}}$	< 0.0414	< 0.0641
$\left\| \dfrac{1}{E_{\mathrm{SC}}} - \dfrac{1}{p} \right\|$	< 0.0129	< 0.0129
$\sigma_{\eta\eta}$	< 0.00998	< 0.0292
$\|\Delta\eta\|$	< 0.00308	< 0.00605
$\|\Delta\phi\|$	< 0.0816	< 0.0394
relative isolation ($\Delta R < 0.3$)	< 0.0588	< 0.0571
expected missing inner hits	≤ 1	≤ 1
conversion veto	yes	yes
transverse impact parameter	< 0.5 mm	< 1 mm
z distance of the track w.r.t. the PV	< 1 mm	< 2 mm

Table 4.5: "Electron Tight Cut-Based ID" as defined in [120]. The middle and the right columns refer to the barrel ($|\eta| < 1.479$) and the endcaps ($|\eta| > 1.479$), respectively.

Jets are considered if they have a $p_\mathrm{T} > 30$ GeV, $|\eta| < 2.4$, and pass the "Loose Jet ID" requirement provided in table 4.6.

variable	requirement
neutral hadron fraction	< 0.99
neutral electromagnetic fraction	< 0.99
charged hadron fraction	> 0
charged multiplicity	> 0
charged electromagnetic fraction	< 0.99
number of constituents	> 1

Table 4.6: "Loose Jet ID" selection as defined in [121].

Type-1-corrected $E_\mathrm{T}^\mathrm{miss}$, defined in the previous chapter, is used applying all the recommended filters, intended to reject spurious $E_\mathrm{T}^\mathrm{miss}$ detections, from the corresponding POG [122].

An initial set of cuts is applied to remove the largest part of the background, leaving mostly those processes with similar topologies to the one expected for our signal:

Exactly two opposite-charge reconstructed tight leptons, electron or muon, are required, with p_T above 25 and 20 GeV, according to the trigger capabilities.[4] Events with additional loose leptons with $p_\mathrm{T} > 10$ GeV are rejected, which targets backgrounds such as WZ.

The invariant mass of the lepton pair, $m_{\ell\ell}$, is required to be greater than 20 GeV, in order to reject possible low-mass resonances which are not taken into account by the simulated samples. In addition, a mass veto of ± 15 GeV around the Z boson mass is applied for dimuon and dielectron events; it removes a large fraction of DY.

The event must moreover contain at least two jets, with at least one of them identified as a medium b-jet. This decidedly favours $t\bar{t}$-like topologies.

Finally, the transverse missing energy, $E_\mathrm{T}^\mathrm{miss}$, is required to be larger than

---

[4]The use of the tight identification aims to avoid non-prompt leptons. More on this will be explained in chapter 6.

50 GeV for the same flavour (ee and $\mu\mu$) channels, to assure DY removal, which, when in absence of neutrinos, suffers from instrumental E_T^miss.

These requirements are summarized in table 4.7, while the expected yields at this stage are presented in table 4.8. Figure 4.3 shows the distributions for some of the main variables after the preselection. They deserve some comments: In general, the data-MC agreement is quite good (one should keep in mind that plotted uncertainties are statistical only). However, the E_T^miss spectrum —figure 4.3(a)— shows a clear shift for lower values as well as a data/MC pothole around 250 GeV. Actually, this issue has been largely investigated within the CMS collaboration, unfortunately without reaching a definite answer. Nonetheless, the subsequent analysis procedure, together with the consideration of our systematic effects will soften this concern as the agreement in our searching variable is recovered.

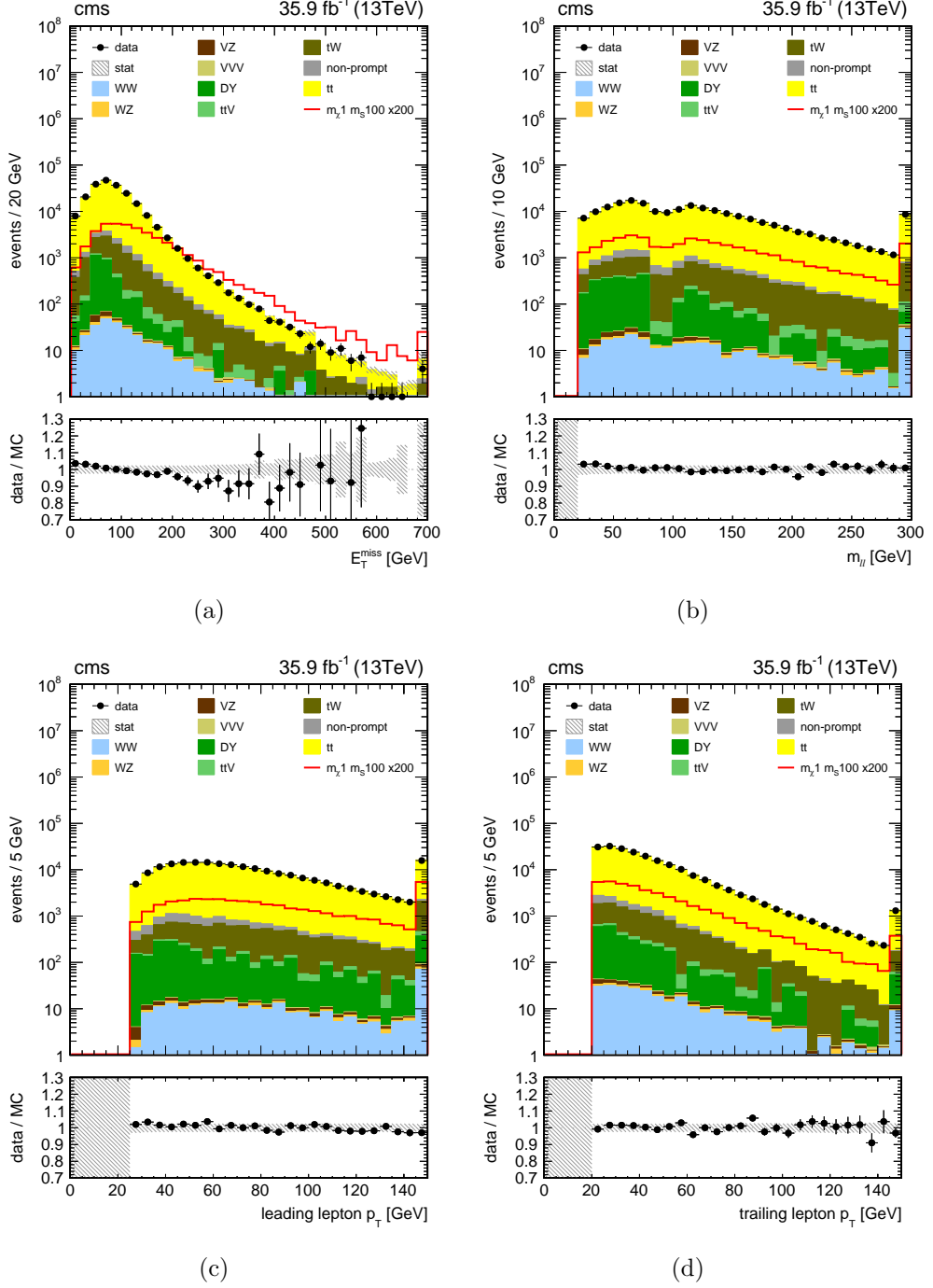| variable	requirement
leading lepton ID	tight
trailing lepton ID	tight
additional loose leptons	0
leading lepton p_T	> 25 GeV
trailing lepton p_T	> 20 GeV
$q^\text{leading} \cdot q^\text{trailing}$	< 0
no. of jets	≥ 2
no. of b-tagged jets	≥ 1
$m_{\ell\ell}$	> 20 GeV
$|m_{\ell\ell} - m_Z|$	> 15 GeV for ee and $\mu\mu$
E_T^miss	> 50 GeV for ee and $\mu\mu$

Table 4.7: Initial selection.

(a)

(b)

(c)

(d)

Figure 4.3: Distributions of the variables (a) E_T^{miss}, (b) $m_{\ell\ell}$, (c) leading lepton p_T, (d) trailing lepton p_T, once the event selection has been applied, for the 2016 integrated luminosity. Scaled by a factor of 200, the $m_S = 100$ GeV signal is superimposed. Uncertainties are statistical only.

process	ee	$\mu\mu$	$e\mu$	$\ell\ell$
WW	36.0 ± 2.8	72.8 ± 4.2	166.0 ± 6.0	274.7 ± 7.8
WZ	5.21 ± 0.63	8.18 ± 0.85	15.75 ± 1.14	29.14 ± 1.56
VZ	10.32 ± 0.51	23.30 ± 0.78	9.01 ± 0.49	42.63 ± 1.05
VVV	2.12 ± 0.25	4.89 ± 0.39	9.96 ± 0.56	16.97 ± 0.73
Z+jets	717 ± 124	1492 ± 198	402 ± 57	2610 ± 240
$t\bar{t}$V	78.12 ± 1.94	144.4 ± 2.8	321.6 ± 4.1	544.1 ± 5.3
$t\bar{t}$	23318 ± 29	47035 ± 44	122851 ± 69	193199 ± 87
tW	1166.5 ± 14.1	2257 ± 21	5792 ± 32	9216 ± 41
non-prompt	$250. \pm 31$	1447 ± 35	2283 ± 63	3979 ± 78
total bkg.	25582 ± 132	52490 ± 210	131850 ± 114	209910 ± 270
data	27051	50067	133520	210638

Table 4.8: Observed data and expected backgrounds after the event selection displayed on table 4.7. The non-prompt lepton background is derived from data, while the remaining processes come directly from MC. Errors are statistical only.

Chapter 5

Signal-background discrimination

The target of any search is to corroborate, or if that were not the case, to refute hypotheses of new physics against that of well-established phenomena. In order to do that, it is convenient to identify observables for which the new and the established can exhibit different values. The purpose of this chapter is to explore variables which may meet that requisite and to enhance those differences by a new technique cd developed in this thesis.

Concerning the former, we, ourselves, have developed a new variable which aims to distinguish between $t\bar{t}$+DM and $t\bar{t}$, and which is widely explained in section 5.1. Section 5.2 will introduce some others. Finally, section 5.3 will deal in depth with the multivariate procedure implemented to intensify the signal-background discrimination.

5.1   Dark matter p_{T}

The objective of what is recounted in this section is to reach a powerful enough discriminant variable between $t\bar{t}$+DM and $t\bar{t}$ through the reconstruction of the p_{T} of the DM signal. In case of (entire) success, it would be useful

to isolate a signal-only region where it would be possible to check if we have a statistically significant amount of data to claim discovery.

The top quark decays almost entirely as $t \to Wb$. As for decays of $t\bar{t}$ pairs, they are classified according to the products of their Ws. This search is confined to the case where both W go to leptons.[1] The six final products are: b, $\bar{b}$, ℓ_1^+, ν_{ℓ_1}, ℓ_2^- and $\bar{\nu}_{\ell_2}$; ℓ_1 and ℓ_2 standing for either e or μ. However, neutrinos can be only partially inferred via the presence of $\vec{E}_{\mathrm{T}}^{\mathrm{miss}}$. Alternatively, knowing every momentum component of each neutrino would mean to know the four-momentum of both t and $\bar{t}$. Subsections 5.1.1 and 5.1.2 illustrates how this is indeed attainable. Subsections 5.1.3 and 5.1.4 aims at extending the procedure for the case when further invisible particles, e.g. DM, accompany the $t\bar{t}$.

5.1.1 Top-antitop reconstruction

This subsection reviews the kinematic reconstruction of the SM $t\bar{t}$ decay chain ending in two leptons, two b-jets and $E_{\mathrm{T}}^{\mathrm{miss}}$ from its two neutrinos, i.e. DM particle is not considered yet. In the following, subscripts in ℓ_1^+ and ℓ_2^- are removed: leptons will be unmistakably identified by their charge. In the same way, ν_{ℓ_1} and $\bar{\nu}_{\ell_2}$ come to ν and $\bar{\nu}$, respectively.

The kinematics of the $t\bar{t}$ dileptonic decay chain is summarised by equations (5.1) to (5.6).

$$p_x^{\mathrm{miss}} = p_{\nu_x} + p_{\bar{\nu}_x}, \tag{5.1}$$

$$p_y^{\mathrm{miss}} = p_{\nu_y} + p_{\bar{\nu}_y}, \tag{5.2}$$

$$m_{W^+}^2 = (E_{\ell^+} + E_\nu)^2 - (\vec{p}_{\ell^+} + \vec{p}_\nu)^2, \tag{5.3}$$

$$m_{W^-}^2 = (E_{\ell^-} + E_{\bar{\nu}})^2 - (\vec{p}_{\ell^-} + \vec{p}_{\bar{\nu}})^2, \tag{5.4}$$

$$m_t^2 = (E_b + E_{\ell^+} + E_\nu)^2 - (\vec{p}_b + \vec{p}_{\ell^+} + \vec{p}_\nu)^2, \tag{5.5}$$

$$m_{\bar{t}}^2 = (E_{\bar{b}} + E_{\ell^-} + E_{\bar{\nu}})^2 - (\vec{p}_{\bar{b}} + \vec{p}_{\ell^-} + \vec{p}_{\bar{\nu}})^2. \tag{5.6}$$

---

[1]The case where the W decays to a τ lepton deserves a brief remark. The τ lepton has a mean lifetime of $\sim 10^{-13}$ s, thus a decay length of just $\sim 100~\mu$m. It decays $\sim 35\%$ of the times leptonically —electron or muon plus two neutrinos— and the remaining $\sim 65\%$, hadronically. This search just considers its leptonic decays.

Quantities referring to b, $\bar{b}$, ℓ^+ and ℓ^- are all measured, whereas neutrino energies are computable via $E^2 = \vec{p}\,^2 + m^2$ relation, where one can assume null mass. The four masses appearing in the system, although treated like knowns, are not exactly known but follow Breit-Wigner distributions. Finally, p_x^miss and p_y^miss are equalled to E_x^miss and E_y^miss, respectively, derived from the experiment, as explained in the previous chapter. Thus, one has six equations for six unknowns: the three momentum components of each neutrino.

A point-by-point account of how to engineer the system, including Sylvester matrices, is offered in reference [17]. At the end, one gets a quartic equation in one of the unknowns, analytically solvable but which leads to a up to fourfold ambiguity. This is not however the only source: since the jet charge cannot be experimentally resolved with enough certitude, assignment of the b-jets to the leptons —the so-called "pairing"— introduces further indeterminacy. In any case, even presuming it is the right one, measured or measure-derived quantities are affected by a variable degree of uncertainty, the energy resolution for jets and its impact on E_T^miss being the dominant.

5.1.2 The reconstruction from a practical point of view

As mentioned above, provided that it is ignored which b quark goes with either lepton as well as the particle momenta are known with a limited degree of resolution, the following method, rooted in reference [123], has been developed to carry out the $t\bar{t}$ reconstruction.

First of all, according to the selection described in section 4.2, events can be sorted into two disjoint categories: a) those with more than one b-jet versus b) those with just one b-jet.

- In the first case, only two combinations are checked, the two possible permutations between the two leptons, ℓ^+ and ℓ^-, and the two most energetic b-jets, b_1 and b_2: $\{\ell^+ \leftrightarrow b_1, \ell^- \leftrightarrow b_2\}$ and $\{\ell^+ \leftrightarrow b_2, \ell^- \leftrightarrow b_1\}$.

- The second case is a bit less simple: the b-jet is always kept together

with every non-b-tagged jet in the event; the two combinations with leptons considered as above. For example, if the event contains one b-jet and two non-b-tagged jets, one would have: $\{\ell^+ \leftrightarrow b, \ell^- \leftrightarrow j_1\}$, $\{\ell^+ \leftrightarrow j_1, \ell^- \leftrightarrow b\}$, $\{\ell^+ \leftrightarrow b, \ell^- \leftrightarrow j_2\}$, $\{\ell^+ \leftrightarrow j_2, \ell^- \leftrightarrow b\}$.

For each combination, one hundred instances of m_{W^+}, m_{W^-}, m_t and $m_{\bar{t}}$ are generated according to their Breit-Wigner distributions, see figure 5.1.
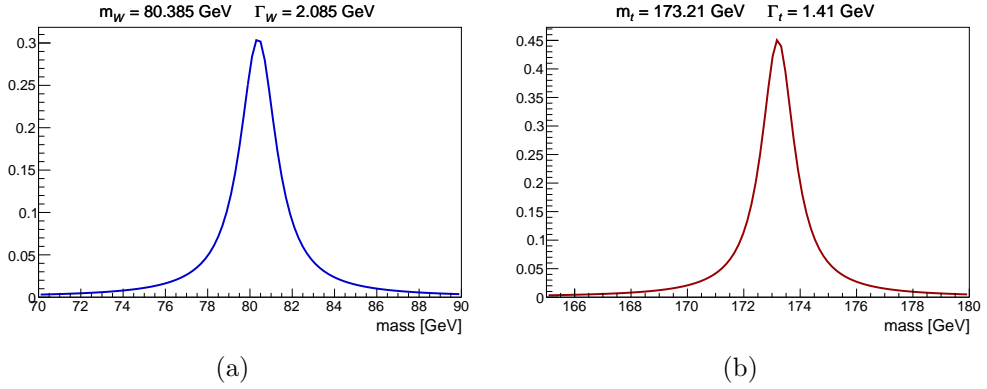
Figure 5.1: Breit-Wigner distributions for the mass resonance of (a) the W boson and (b) the top quark.

Variations of the p_T of both b (or b-like) jets are also computed as follows: The jet measured energy is updated by an additive factor, ΔE, generated according to a Gaussian centred at zero and width equal to the jet energy uncertainty, which depends on E itself and η. A correction factor, λ, is derived from the original and the updated vector momentum:

$$\lambda(E, \eta) = \frac{[E + \Delta E(E, \eta)]^2 - m^2}{\vec{p}^{\,2}}. \tag{5.7}$$

The updated p_T is simply:

$$p_T^{\text{new}} = \lambda(E, \eta)\, p_T^{\text{old}}. \tag{5.8}$$

One hundred different quartic equations have to be solved, with up to four real roots each. However, if any, just one is picked: the one which results

in the lowest invariant mass of the $t\bar{t}$ system, $m_{t\bar{t}}$. The motivation for this lies in the empirical fact that in 85% of cases, the solution satisfying this requisite matches the true simulated kinematics [124].

One way of rating the correctness of the {lepton, b-jet} pairing, i.e. the quality of the combination, is through the likelihood of $m_{(\ell b)_1}$ and $m_{(\ell b)_2}$ occurring in a real $t\bar{t}$ decay. In order to do that, one takes the $m_{\ell b}^{\text{true}}$ spectrum as a probability density function, see figure 5.2, and evaluates both $m_{(\ell b)_1}$ and $m_{(\ell b)_2}$ against it each of the hundred iterations (remember that the jet p_T is recalculated every time). The product of both probabilities constitutes the "weight of the iteration", but if no solution exists, this weight is set to zero. The "weight of the combination" as a whole, or "global weight" to avoid confusion, is just the addition of the hundred iteration weights. The higher the global weight, the most reliable the pairing.
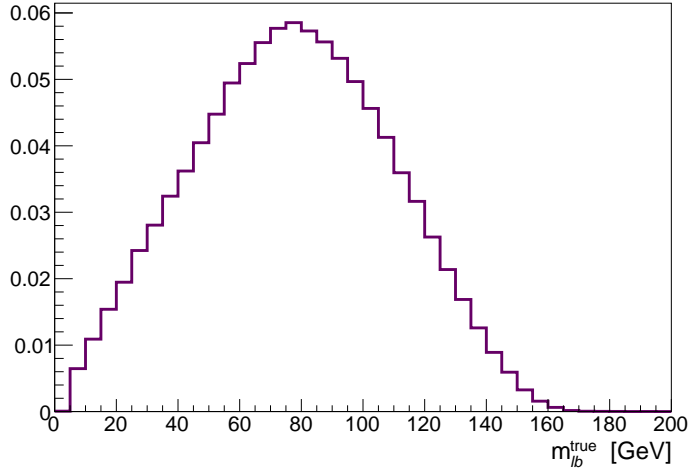

Figure 5.2: Normalised distribution of $m_{\ell b}$ from simulated events, i.e. not suffering from inefficiencies from the reconstruction.

The selected combination is that of the highest global weight. If there is no solution at all, the event is categorized as unsolved at this stage.

5.1.3 $t\bar{t}+$DM reconstruction

As a central part of this thesis, an extension of the former method to processes with one additional invisible particle ahs been developed.

In the following, it will be assumed that the absence of solution in the previous step is due to the presence of additional $\vec{E}_{\mathrm{T}}^{\mathrm{miss}}$.[2] That is, equations (5.1) and (5.2) now turn into:

$$p_x^{\mathrm{miss}} \;=\; p_{\nu_x} + p_{\bar{\nu}_x} + p_{\mathrm{DM}_x}, \tag{5.9}$$

$$p_y^{\mathrm{miss}} \;=\; p_{\nu_y} + p_{\bar{\nu}_y} + p_{\mathrm{DM}_y}, \tag{5.10}$$

where the extra term is attributed to DM in the current context. It is clear that the system of equations becomes undetermined.

No solution means that for as many as {number of combinations $\times$ hundred iterations} quartic polynomials, all of them lie above or below the horizontal axis. Thus, one defines a "cost" variable like the minimum distance between the polynomial and the axis, which would reflect the closeness to the solvable state, see figure 5.3.

Let the mth combination, nth iteration of smallest cost be selected. The method will rely on the polynomial to intersect the axis by varying $\vec{E}_{\mathrm{T}}^{\mathrm{miss}}$, as explained just below. The difference between the original $\vec{E}_{\mathrm{T}}^{\mathrm{miss}}$ and the value which makes the equation to have a root will be imputed to DM.

Nothing prevents from defining the "cost" as a function of $\vec{E}_{\mathrm{T}}^{\mathrm{miss}}$, i.e. $\mathrm{cost} = \mathrm{cost}(E_x^{\mathrm{miss}}, E_y^{\mathrm{miss}})$. To bring the polynomial closer to the horizontal axis simply means to minimize the "cost" function. A gradient descent algorithm will be used for this purpose.

Each iteration starts by an update on the variable:

$$(E_x^{\mathrm{miss}}, E_y^{\mathrm{miss}})^{\mathrm{new}} = (E_x^{\mathrm{miss}}, E_y^{\mathrm{miss}})^{\mathrm{old}} - \epsilon \, \nabla \mathrm{cost}|_{(E_x^{\mathrm{miss}}, E_y^{\mathrm{miss}})^{\mathrm{old}}}, \tag{5.11}$$

---

[2]For sure, other reasons such as experimental errors, misreconstructions, etc. could be behind this behaviour, but this method will only consider them as systematic effects.

where ϵ is the step size, not constant but regulated according to:

$$\left.\begin{array}{c} \mathrm{cost}_{i-1} - \mathrm{cost}_{i-2} < 0 \\ \nabla\mathrm{cost}_{i-1} - \nabla\mathrm{cost}_{i-2} < 0 \end{array}\right\} \epsilon_i = \kappa\,\epsilon_{i-1}, \qquad \text{otherwise } \epsilon_i = \epsilon_{i-1},$$

with $\kappa = 0.9$ and $\epsilon_0 = 0.7\,E_{\mathrm{T}}^{\mathrm{miss\,orig}}$, both constants set after checking quite a few combinations.

Immediately after, it is checked if the quartic equation, entering $(E_x^{\mathrm{miss}}, E_y^{\mathrm{miss}})^{\mathrm{new}}$, is solvable. If it is, then the difference with respect to the original $\vec{E}_{\mathrm{T}}^{\mathrm{miss}}$ is ascribed to DM, $\vec{p}_{\mathrm{T}}^{\mathrm{DM}}$:

$$\vec{p}_{\mathrm{T}}^{\mathrm{DM}} = (E_x^{\mathrm{miss}}, E_y^{\mathrm{miss}})^{\mathrm{orig}} - (E_x^{\mathrm{miss}}, E_y^{\mathrm{miss}})^{\mathrm{new}}. \tag{5.12}$$

Otherwise, a new iteration sets off.

Up to one thousand iterations are attempted. If the quartic equation remains unsolvable, the event is categorised as fully unsolved.

A schematic view of the algorithm operation is provided in figure 5.4.

A delicate issue poses at this point. Given a definite set of $\{\ell^+, \ell^-, b, \bar{b}\}$, more than one point on the plane $(E_x^{\mathrm{miss}}, E_y^{\mathrm{miss}})$ prompts solution for the quartic equation; in other words, purely neutrino $\vec{E}_{\mathrm{T}}^{\mathrm{miss}}$ is not uniquely determined, as one can deduce from equations (5.1) to (5.6). Well-behaved $(E_x^{\mathrm{miss}}, E_y^{\mathrm{miss}})$ points seem to spread over an ellipse: once touched wherever by the gradient descent algorithm, the calculation stops, which makes one to consider that it remains profit to be exploited.

5.1.4   Performance of $\vec{p}_{\mathrm{T}}^{\mathrm{DM}}$

The adequacy of $\vec{p}_{\mathrm{T}}^{\mathrm{DM}}$ computation can be validated in figures 5.5 and 5.6, where true (generated) versus reconstructed $|\vec{p}_{\mathrm{T}}^{\mathrm{DM}}|$ for different $t\bar{t}$+DM models are plotted. One can appreciate how events accumulate at the vicinity of the diagonal. To be more precise, figure 5.7 shows the resolution of $|\vec{p}_{\mathrm{T}}^{\mathrm{DM}}|$ defined
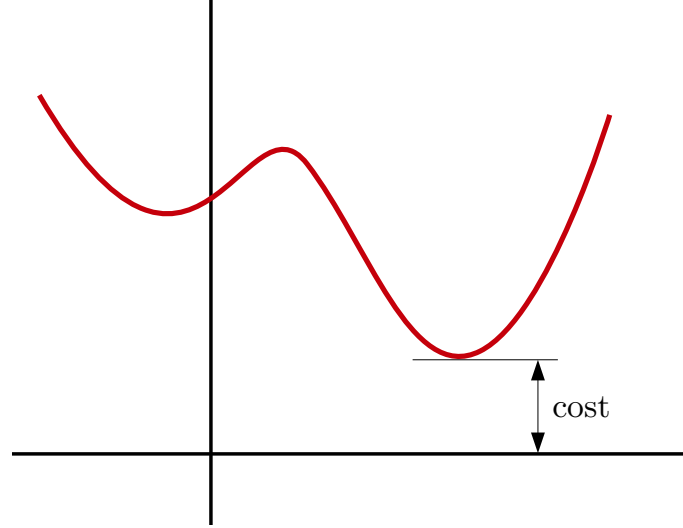
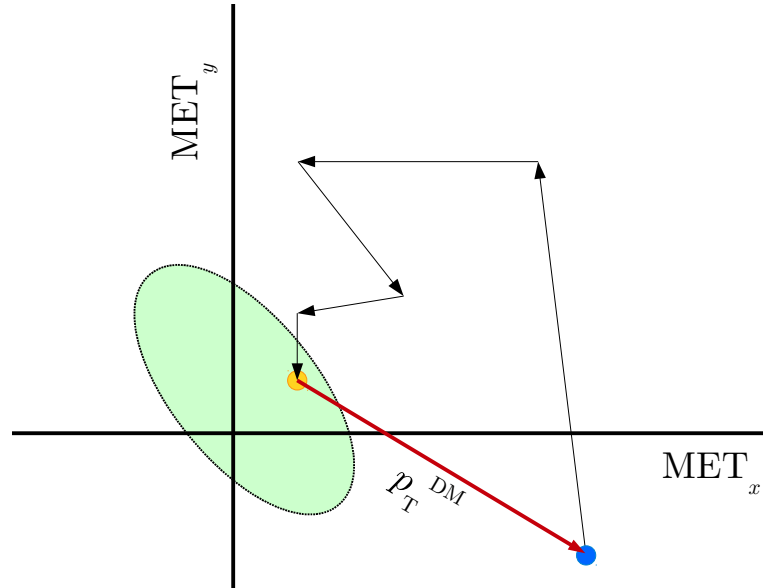Figure 5.3: Schematic representation of the definition of the "cost" function.

Figure 5.4: Schematic representation of the computation of $\vec{p}_{\mathrm{T}}^{\mathrm{DM}}$ through the gradient descent method. Potential $(E_x^{\mathrm{miss}}, E_y^{\mathrm{miss}})$ solutions for a SM $t\bar{t}$ event would lie on the pale green ellipse. The blue dot exemplifies the case for a $t\bar{t}+$DM event. The gradient descent method operates along the pathway marked by the black arrows. The first iteration which falls inside the ellipse ends at the yellow dot. The difference with respect to the blue dot is $\vec{p}_{\mathrm{T}}^{\mathrm{DM}}$.

as:

$$\delta = \frac{|\vec{p}_\mathrm{T}^{\,\mathrm{DM}}| - |\vec{p}_\mathrm{T\ TRUE}^{\,\mathrm{DM}}|}{|\vec{p}_\mathrm{T\ TRUE}^{\,\mathrm{DM}}|} \, , \tag{5.13}$$

One can observe how δ is more spread for the scalar models than for pseudoscalar ones. Moreover, it is worse for low mediator masses. The cause can be sensed by going back to figure 1.4. There, for the same mediator mass, $E_\mathrm{T}^{\mathrm{miss}}$ peaks before for the scalar model than for the pseudoscalar one, and for those of lower mass with respect to those of higher mass. Thus one concludes than the higher the $E_\mathrm{T}^{\mathrm{miss}}$, the better the performance of $\vec{p}_\mathrm{T}^{\,\mathrm{DM}}$.

It is worth contrasting how $|\vec{p}_\mathrm{T}^{\,\mathrm{DM}}|$ behaves for some reference signals and the main background ($t\bar{t}$) under real conditions, i.e. accounting for detection disturbance. This is shown in figure 5.8, where the histograms have been normalised to their sample size. Needless to say, events used here did not succeed the reconstruction described in subsection 5.1.1, referred to as "standard". One can appreciate how production of light-scalar-mediator DM with $t\bar{t}$ barely differentiates from $t\bar{t}$ alone, but, still, it does a bit. Ideally, their spectra should peak in the first bin, [0, 40 GeV]. Thus, one could associate an offset of ~ 60 GeV to the method itself in addition to mismeasurements effects. On the other hand, the peak shift for the heavier mediator cases, as well as its spread, supports the potential of $\vec{p}_\mathrm{T}^{\,\mathrm{DM}}$ from qualitative grounds.

The discussion on the paragraph above does not care about the rates of success of either reconstruction for the different processes. It does deserve some numbers: Quite reasonably, the standard reconstruction for the $t\bar{t}$ process achieves a satisfactory result 98.5% of the times. For $m_\mathrm{S} = 10$ GeV $t\bar{t}$+DM, the rate is slightly lower: 95.0%, whereas for $m_\mathrm{S} = 500$ GeV $t\bar{t}$+DM, it does not reach the 30.0%. Having said that, the application of the reconstruction explained in this subsection raises the success rate to the following figures: 99.5% for the $t\bar{t}$; 97.5% for the $m_\mathrm{S} = 10$ GeV $t\bar{t}$+DM; and, the most remarkable, 85.0% for $m_\mathrm{S} = 500$ GeV $t\bar{t}$+DM. These results are summarised in table 5.1.

The "dark matter p_T" variable, represented by $p_\mathrm{T}^{\mathrm{DM}}$, is defined as follows: for those events where the $t\bar{t}$ (or standard) reconstruction described in sub-
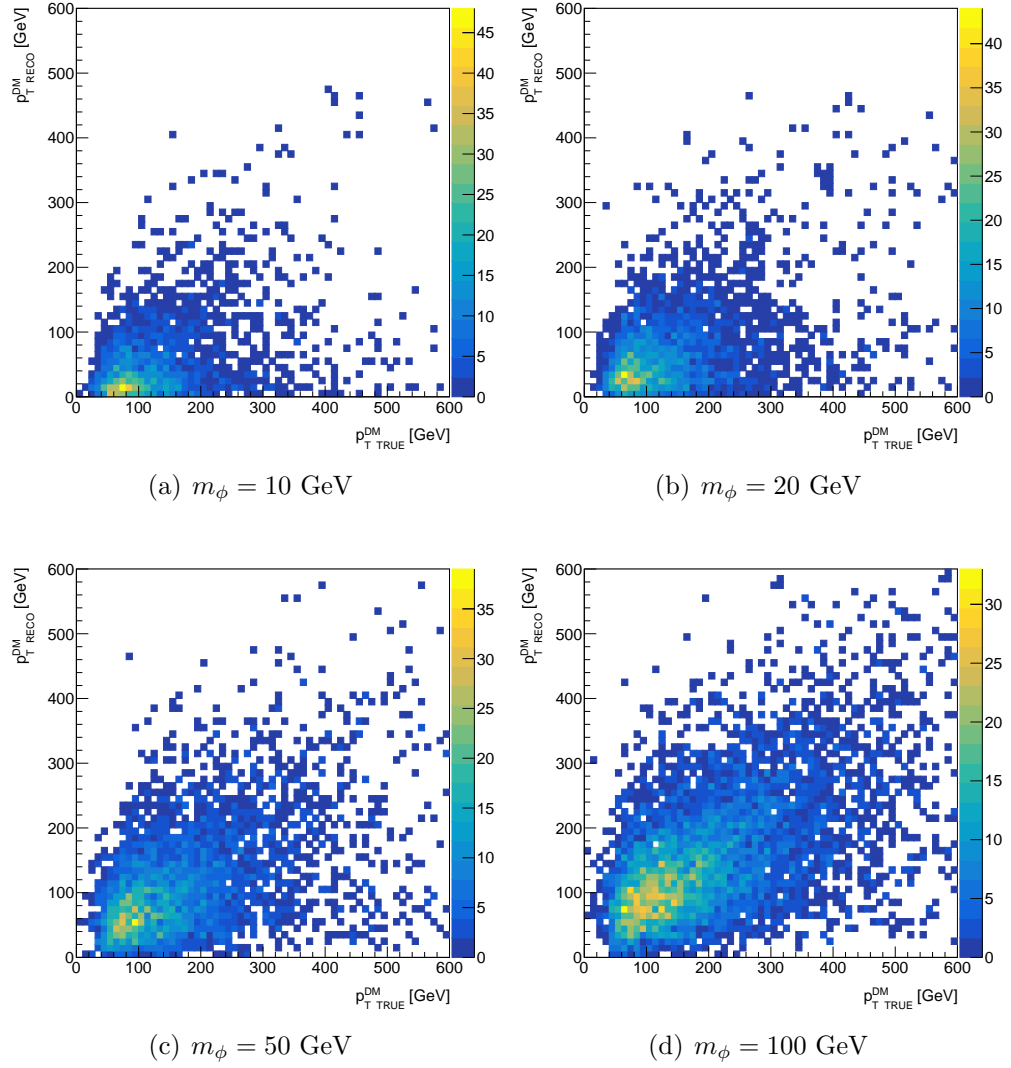
(a) $m_\phi = 10$ GeV

(b) $m_\phi = 20$ GeV

(c) $m_\phi = 50$ GeV

(d) $m_\phi = 100$ GeV

Figure 5.5: Generated versus reconstructed $|\vec{p}_\mathrm{T}|$ for different $t\bar{t}+$DM scalar models.
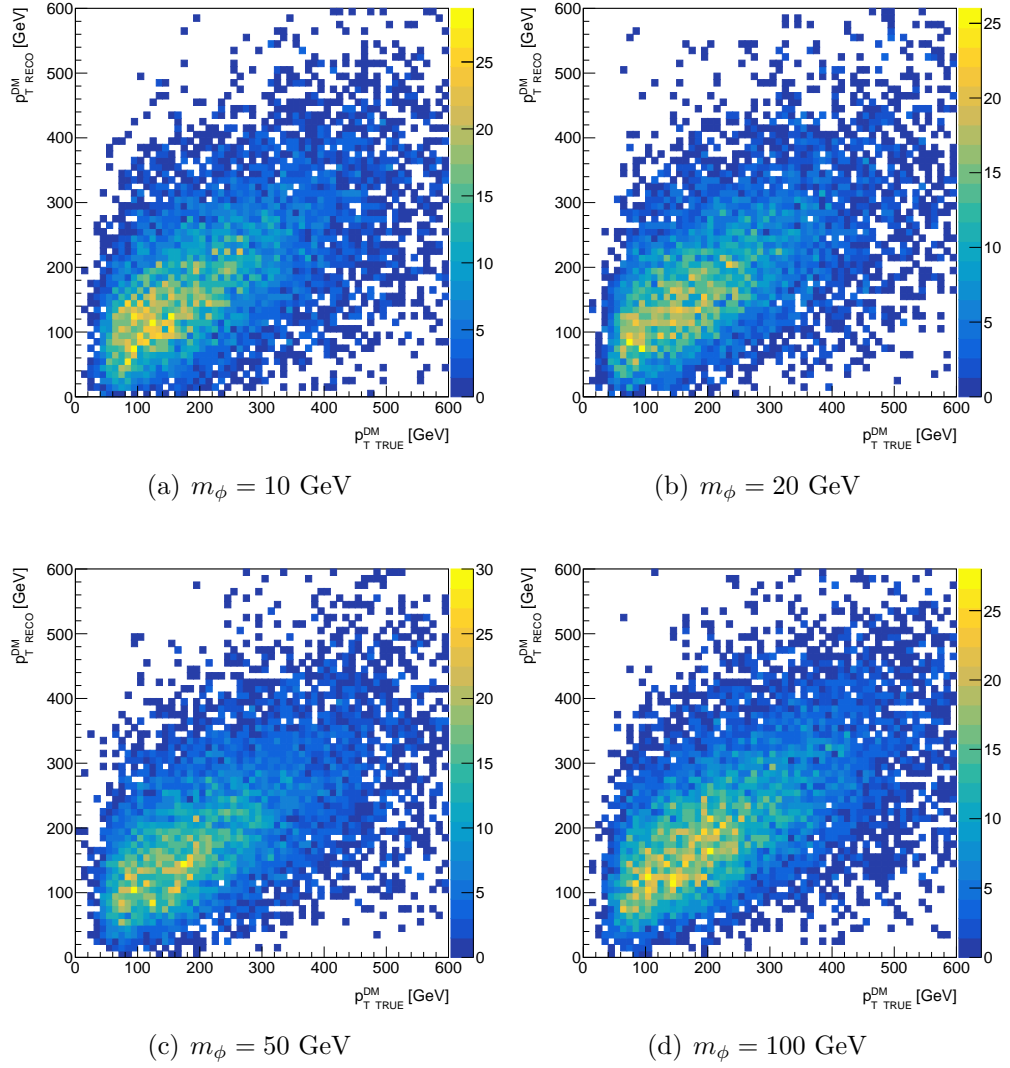
(e) $m_\phi = 200$ GeV

(f) $m_\phi = 300$ GeV

(g) $m_\phi = 500$ GeV

Figure 5.5: Generated versus reconstructed $|\vec{p}_{\mathrm{T}}|$ for different $t\bar{t}+$DM scalar models (cont.)

(a) $m_\phi = 10$ GeV

(b) $m_\phi = 20$ GeV
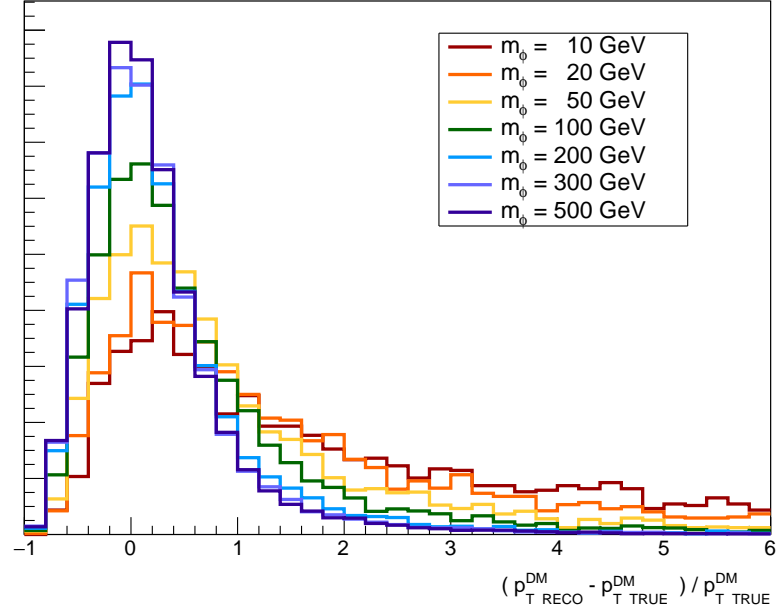
(c) $m_\phi = 50$ GeV

(d) $m_\phi = 100$ GeV

Figure 5.6: Generated versus reconstructed $|\vec{p}_\mathrm{T}|$ for different $t\bar{t}+\mathrm{DM}$ pseudoscalar models.

(e) $m_\phi = 200$ GeV

(f) $m_\phi = 300$ GeV
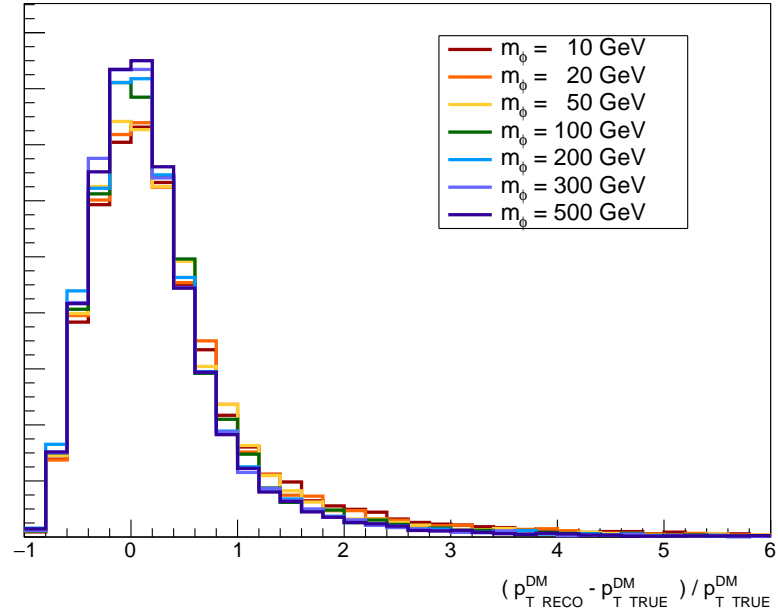
(g) $m_\phi = 500$ GeV
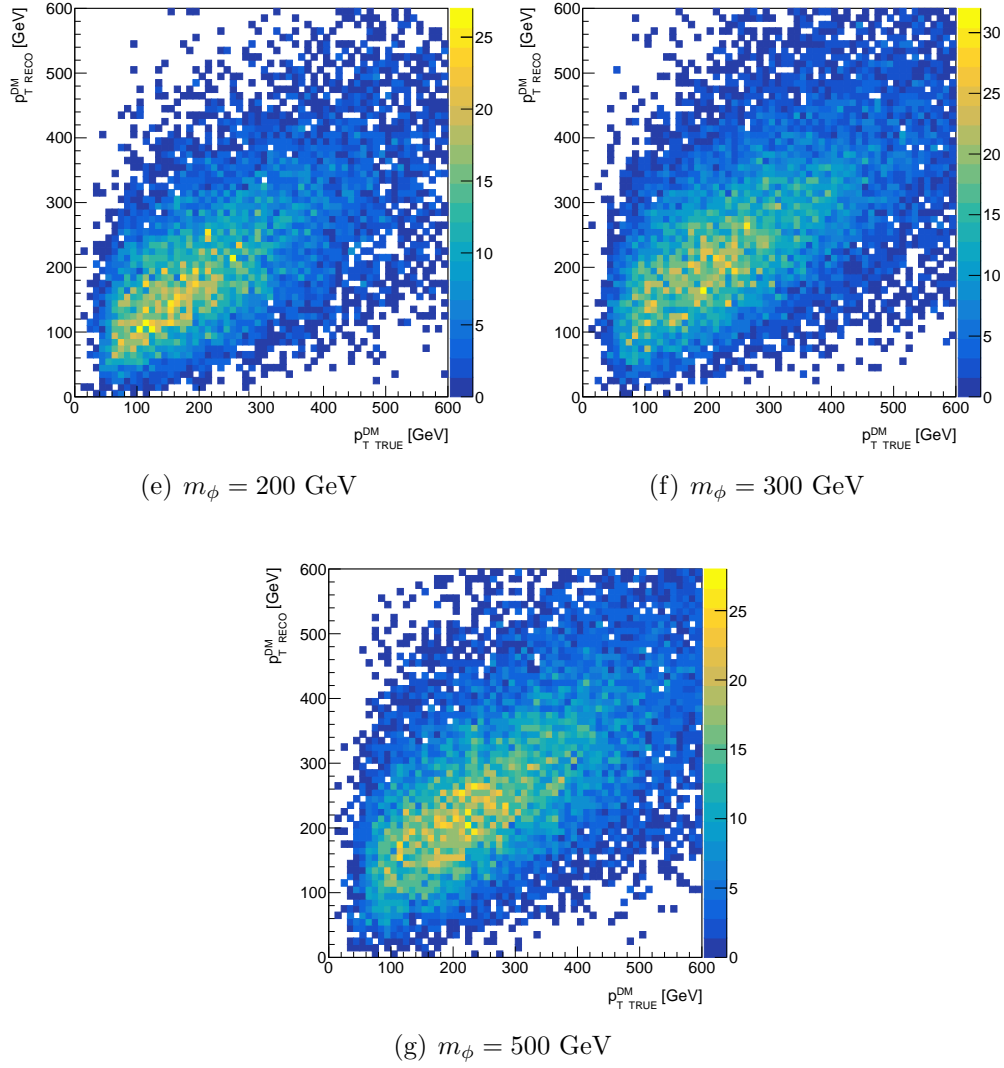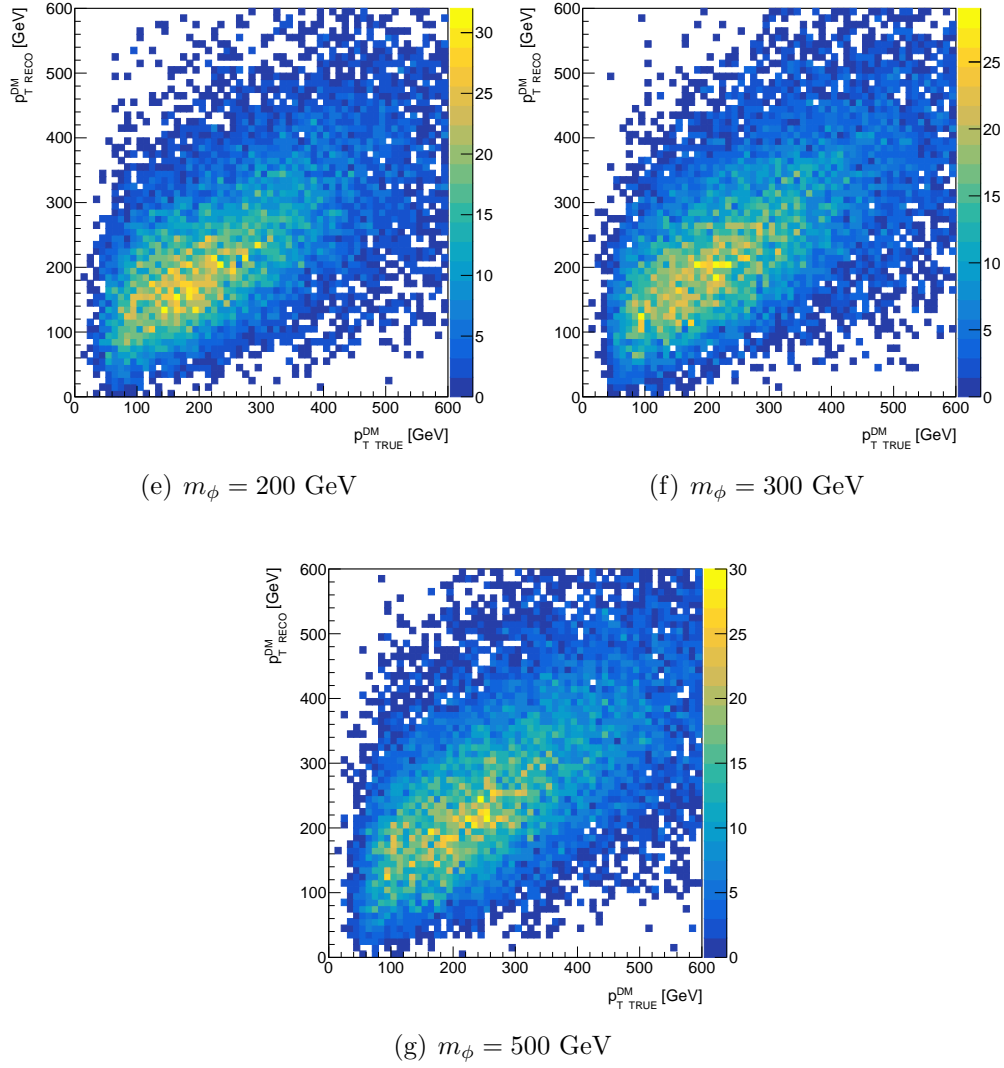
Figure 5.6: Generated versus reconstructed $|\vec{p}_\mathrm{T}|$ for different $t\bar{t}$+DM pseudoscalar models (cont.)
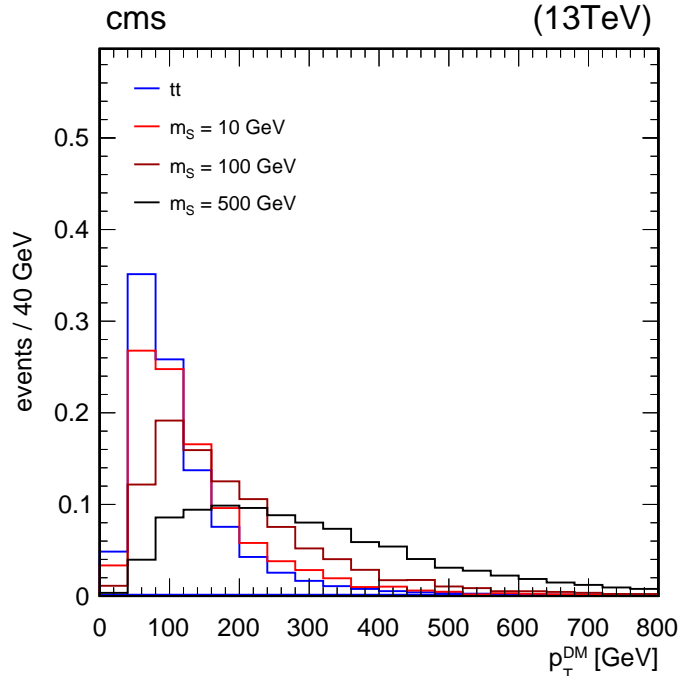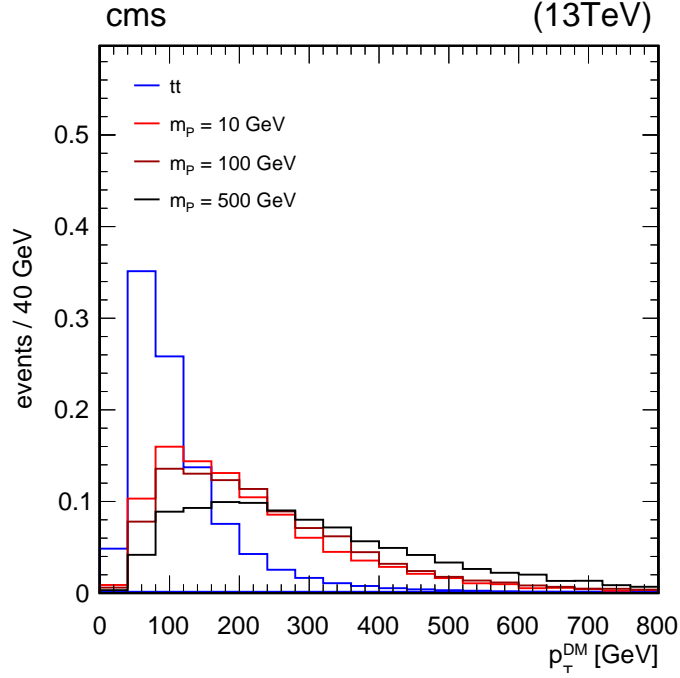
(a)

(b)

Figure 5.7: $|\vec{p}_\mathrm{T}^\mathrm{DM}|$ resolution for (a) scalar and (b) pseudoscalar models.

(a)

(b)

Figure 5.8: Shape distribution of $|\vec{p}_{\mathrm{T}}^{\mathrm{DM}}|$ for the $t\bar{t}$ together with three (a) scalar and (b) pseudoscalar signal models.

	$t\bar{t}$	light $t\bar{t}$+DM	heavy $t\bar{t}$+DM
standard reconstruction	98.5%	95.0%	< 30%
either reconstruction	99.5%	97.5%	85.0%

Table 5.1: Rate of events succeeding the standard reconstruction (first row) and either reconstruction (second row), for three reference processes.

section 5.1.1 works, p_T^{DM} is the above-mentioned global weight multiplied by an appropriate negative constant; if it does not succeed, but the $t\bar{t}$+DM reconstruction does, p_T^{DM} is the magnitude (thus, ≥ 0) of $\vec{p}_T^{DM}$ introduced in equation (5.12); finally, events failing both are discarded.

It is worth noting that the so-called global weight introduced at the end of section 5.1.2, always greater than or equal to zero, is indicative of $t\bar{t}$ likeness. Remember that, either in relative or in absolute terms, the higher the global weight, the larger the likelihood that the event will be an authentic $t\bar{t}$. It is multiplied by a negative constant here just because one is interested in keeping positive values of p_T^{DM} solely for $t\bar{t}$+DM events (or $t\bar{t}$+DM-like, at worst). In conclusion, the more negative p_T^{DM}, the higher the compatibility with being a $t\bar{t}$. Moreover, continuity at $p_T^{DM} = 0$ is ensured.

5.2 Observables used to distinguish the signal from the SM background

Had the selection contained in table 4.7 been applied, variables which would presumably reflect differences between signal and background are inspected. A list of those finally considered together with a brief description of each is provide below; their spectra shown for an integrated luminosity of 35.9 ± 0.9 fb^{-1} in figure 5.9 as well.

E_T^{miss} : Extensively described above. It is the magnitude of the sum of the $\vec{p}_T$ of all undetected objects in the event, indirectly determined. On top of "bare" $t\bar{t}$, $t\bar{t}$+DM contributes the DM particles to E_T^{miss}, even though the sum of all the $\vec{p}_T$ is of course a vector sum. E_T^{miss} is, doubtless,

the most immediate observable to try separating the signal from the background. Figure 5.9(a) is an exact replica of figure 4.3(a), thus comments on the data-MC agreement at the end of section 4.2 applies here equally.

$\Delta\phi_{\ell\ell\,E_{\mathrm{T}}^{\mathrm{miss}}}$: Difference in the azimuthal angle between the system formed by the two leptons and $\vec{E}_{\mathrm{T}}^{\mathrm{miss}}$. It was already put in use in the previous version of this search at $\sqrt{s} = 8$ TeV [1]. Its motivation has to do with the fact that the production of DM particles would force the accompanying $t\bar{t}$ to decay in a relatively narrow cone in order to balance the momentum in the transverse plane. That would not be the case for a $t\bar{t}$ event, provided that no extras have to be balanced. In figure 5.9 (b) one can appreciate the slight difference in the spectra slope for those of $t\bar{t}$ and $t\bar{t}$+DM. Figure 5.9(b) shows a complete data-MC agreement within the statistical uncertainties, so no further words are required.

$p_{\mathrm{T}}^{\mathrm{DM}}$: Fully described in section 5.1. It has been designed on purpose to separate $t\bar{t}$+DM from $t\bar{t}$. It tries to recover the p_{T} of the eventual DM contribution. Figure 5.9(c) shows an almost complete data-MC agreement within the statistical uncertainties. Systematic effects will cover the mismatch.

$M_{\mathrm{T}2}(\ell\ell)$: It extends the potentiality of the "transverse mass" variable, m_{T}, to pairs of identical particles, or particle-antiparticle, decaying in an equivalent way to $W \to \ell\nu$, i.e. to one visible plus one invisible. The point here is that $\vec{p}_{\mathrm{T}}$ of invisibles cannot be inferred separately, as they fuse into $\vec{E}_{\mathrm{T}}^{\mathrm{miss}}$.

Let $\vec{p}_{\mathrm{T}1}^{\,\mathrm{vis}}$ and $\vec{p}_{\mathrm{T}2}^{\,\mathrm{vis}}$ be the transverse momentum of the first and second visibles. Supposed $p_{\mathrm{T}} \gg m$ for both the visibles and the invisibles. $M_{\mathrm{T}2}$ is defined as [125]:

$$M_{\mathrm{T}2}^2 = \min_{\vec{p}_{\mathrm{T}1}^{\,\mathrm{invis}}+\vec{p}_{\mathrm{T}2}^{\,\mathrm{invis}}=\vec{E}_{\mathrm{T}}^{\mathrm{miss}}} \left[\max\left\{ m_{\mathrm{T}}^2(\vec{p}_{\mathrm{T}1}^{\,\mathrm{vis}}, \vec{p}_{\mathrm{T}1}^{\,\mathrm{invis}}), m_{\mathrm{T}}^2(\vec{p}_{\mathrm{T}2}^{\,\mathrm{vis}}, \vec{p}_{\mathrm{T}2}^{\,\mathrm{invis}}) \right\} \right],$$

(5.14)

where

$$m_{\mathrm{T}}^2(\vec{p}_{\mathrm{T}}^{\,\mathrm{vis}}, \vec{p}_{\mathrm{T}}^{\,\mathrm{invis}}) = 4\, |\vec{p}_{\mathrm{T}}^{\,\mathrm{vis}}|\, |\vec{p}_{\mathrm{T}}^{\,\mathrm{invis}}|\, \sin^2\left(\frac{\alpha}{2}\right),$$

(5.15)

being α the angle between $\vec{p}_{\mathrm{T}}^{\,\mathrm{vis}}$ and $\vec{p}_{\mathrm{T}}^{\,\mathrm{invis}}$.

That is, one must save the highest m_{T} of every hypothetical $(\vec{p}_{\mathrm{T}1}^{\,\mathrm{invis}}, \vec{p}_{\mathrm{T}2}^{\,\mathrm{invis}})$ pair satisfying the constraint $\vec{p}_{\mathrm{T}1}^{\,\mathrm{invis}} + \vec{p}_{\mathrm{T}2}^{\,\mathrm{invis}} = \vec{E}_{\mathrm{T}}^{\mathrm{miss}}$, and ultimately admit the realisation which results in the most unfavourable ($\equiv$ lowest mass) case.

Here, the leptons play the role of visibles, hence $M_{\mathrm{T}2}(\ell\ell)$. For an ideal $t\bar{t}$, i.e. without instrumental errors, the $M_{\mathrm{T}2}(\ell\ell)$ spectrum should exhibit an edge on m_W. On the contrary, for the $t\bar{t}+\mathrm{DM}$ case, since $\vec{E}_{\mathrm{T}}^{\mathrm{miss}}$ is not only due to neutrinos, one would expect a non-singular $M_{\mathrm{T}2}(\ell\ell)$ distribution. Such is the case as figure 5.9(d) illustrates. Data-MC agreement within statistical uncertainties is clearly preserved up to ~ 130 GeV. Beyond, one should bear in mind that systematic effects will cover the mismatch; in any case, the subsequent analysis procedure will mitigate this concern.

Why $t\bar{t}$ presents a tail beyond $m_W \simeq 81$ GeV is explained by different reasons: instrumental $\vec{E}_{\mathrm{T}}^{\mathrm{miss}}$ (see figure 5.10) mainly due to the impact of jet energy errors, lately taken into account by the "jet energy scale" systematic; or selected leptons which are actually non-prompt.

Larger or smaller, it is clear that the four variables have some separation power. Fortunately, there are tools capable of maximise it with minor associated costs. Essentially, they lie in combining information from different sources in a non-linear, complexity-growing way. "Artificial neural networks" (ANNs) are one type of those amongst many.

5.3   The artificial neural network approach

The problem is the following: for a relatively small set of events, each identified by a vector $\vec{x}$ —in this case $\vec{x} = (E_{\mathrm{T}}^{\mathrm{miss}}, \Delta\phi_{\ell\ell\,E_{\mathrm{T}}^{\mathrm{miss}}}, p_{\mathrm{T}}^{\mathrm{DM}}, M_{\mathrm{T}2}(\ell\ell))$—, one knows which category amongst two the event belongs to —"signal" or "background". Now, knowing $\vec{x}$ for a much bigger set of unlabelled events, a real number, y, between zero and one indicating signal (or background)
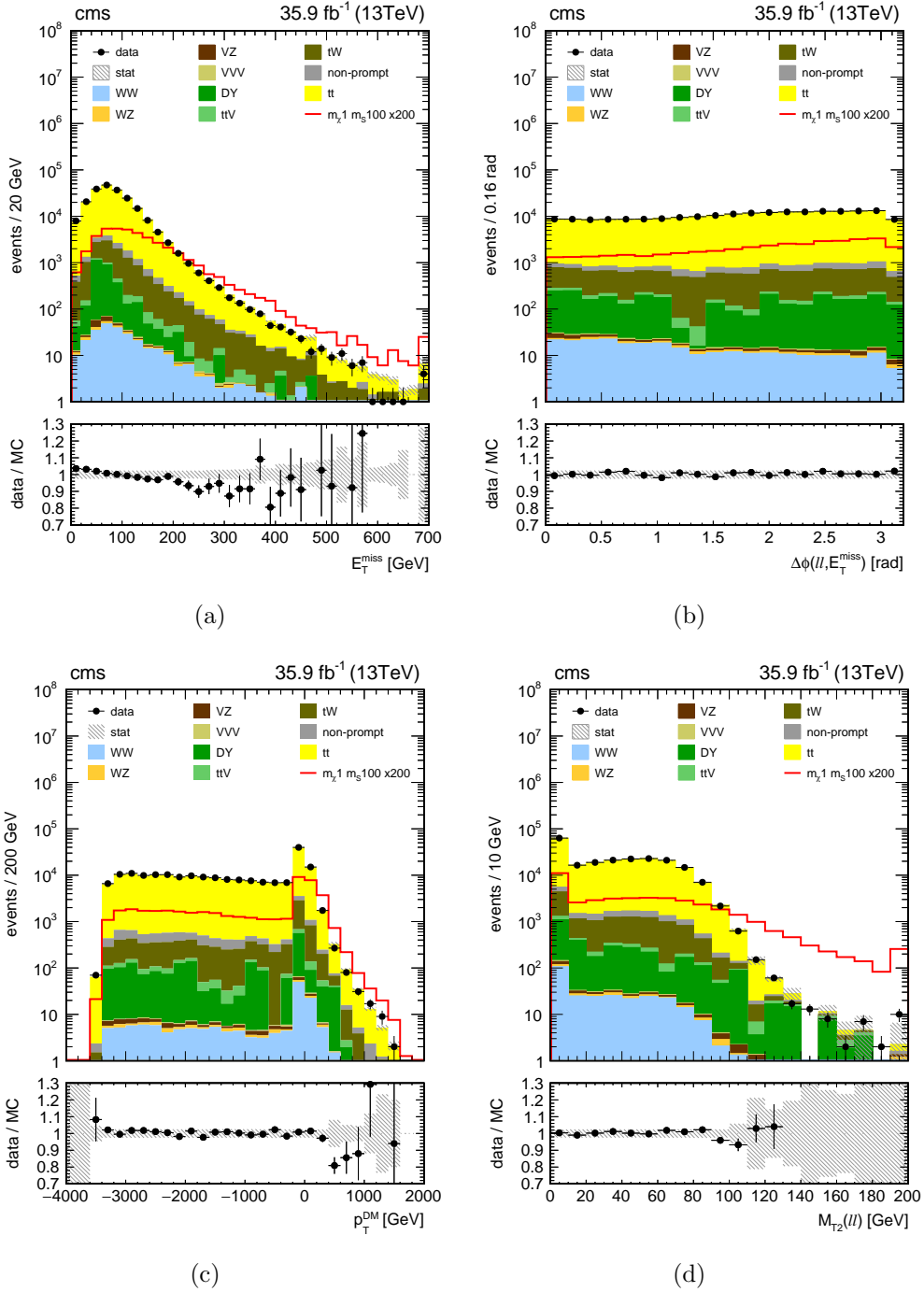
Figure 5.9: Distributions of the four discriminating variables considered: (a) E_T^{miss}, (b) $\Delta\phi_{\ell\ell\,E_T^{miss}}$, (c) p_T^{DM}, (d) $M_{T2}(\ell\ell)$, for the 2016 integrated luminosity. Scaled by a factor of 200, the $m_S = 100$ GeV signal is superimposed. Uncertainties are statistical only.

likeness needs to be assigned. Chosen the classifier model and its external parameters, the internal ones are recursively adjusted from the smaller set, for which both the input and the output are known.

The small set is indeed divided into two subsets (usually two halves). One is intended for the the adjustment of the internal parameters itself ("training" set), whereas the other one is saved to evaluate the performance of the once finished classifier ("test" set): events from the latter are given to the new classifier and it is checked how well it tags them.

A direct way to look at this is through the background rejection versus signal efficiency curve (a few will be shown in the following, see for example figure 5.11): For an specific threshold y_{th} within the bounds of y (normally $y_{low} = 0.$ and $y_{up} = 1.$), the rate of background events assigned $y < y_{th}$ over the total is set against the rate of signal events assigned $y > y_{th}$ over the total. Acting y_{th} like the parameter, the parametric curve is traced. In our case, the more it tends towards the top right-hand corner, the better.

Different multivariate techniques are available on the market, being perhaps Boosted decision trees (BDTs) and artificial neural networks (ANNs) the most renowned today. Although our expertise leaned towards the latter, in a preliminary stage of this investigation, both were considered. Figure 5.11 shows a comparison of the performance of two BDT and three ANN instances in terms of their above-described background rejection versus signal efficiency curves.[3] Just one, uncomplicated parameter has been modified for each case: the "maximum depth" of the BDT[4] and the "architecture" of the ANN (more will be said about below). The $m_S = 100$ GeV $t\bar{t} + $ DM (mildly distinct from the main background, $t\bar{t}$) played the role of signal here, whereas the background (here and everywhere below) consisted of $t\bar{t}$ events. Provided that no huge differences arise amongst both classifiers, whereas we do know much more about the ANN case in advance, this will be the choice. Moreover, the own ranking on the legend, based on the area under the curve, places the

---

[3]The software package used for all the computations this section refers to is the Toolkit for Multivariate Data Analysis (TMVA) [126].

[4]In the BDT context, the maximum depth is defined as the number of nodes along the path from the root node to the farthest leaf node.

two ANNs above the three BDTs, although this does not constitute a strong argument at the current level of the optimisation.

ANNs are inspired by structures of the nervous tissue [127]. They are organised on the basis of functional units named "neurons", arranged in layers and highly connected to each other. Each connection is characterized by a weight, denoting its importance.

Neurons receive multiple signals either from outside or from their co-workers at the back layer, process them according to a non-linear internal "activation function", and fire the output either to the next layer or to the outside. Put it with mathematical notation: the neuron response function ρ maps the neuron input $\{i_1, i_2, ..., i_n\}$ onto the neuron output. The response function can be separated into a $\mathbb{R}^n \mapsto \mathbb{R}$ synapse function, κ, and the aforementioned $\mathbb{R} \mapsto \mathbb{R}$ neuron activation function, α, so that $\rho = \alpha \circ \kappa$. The chosen forms of both κ and α are detailed below.

The objective of the learning or "training" phase is to optimize the connection weights in such a way that the ANN delivers an output as faithful to the known event category as possible. Let it be $\tilde{y}_i$ the (value associated to the) true category of the ith event, and y_i, the value delivered by the ANN, which depends, of course, on all the connections weights, $\vec{w}$. The error function or "loss", $\mathcal{E}$, is then defined as the "distance", ε, between $\tilde{y}_i$ and $y_i(\vec{w})$ —specific definition of ε below— extended to the entire training set:

$$\mathcal{E}(\vec{w}) = \sum_{i=1}^{N} \varepsilon\left(\tilde{y}_i,\, y_i(\vec{w})\right). \tag{5.16}$$

The set of weights that minimises the function $\mathcal{E}(\vec{w})$ is found by using the method of the gradient descent. Starting from a random seed, $\vec{w}_0$, the weights are updated by moving a small distance in the $\vec{w}$-space into the direction, $-\nabla_{\vec{w}}\mathcal{E}$:

$$\vec{w}_{k+1} = \vec{w}_k - \eta \nabla_{\vec{w}}\mathcal{E}, \tag{5.17}$$

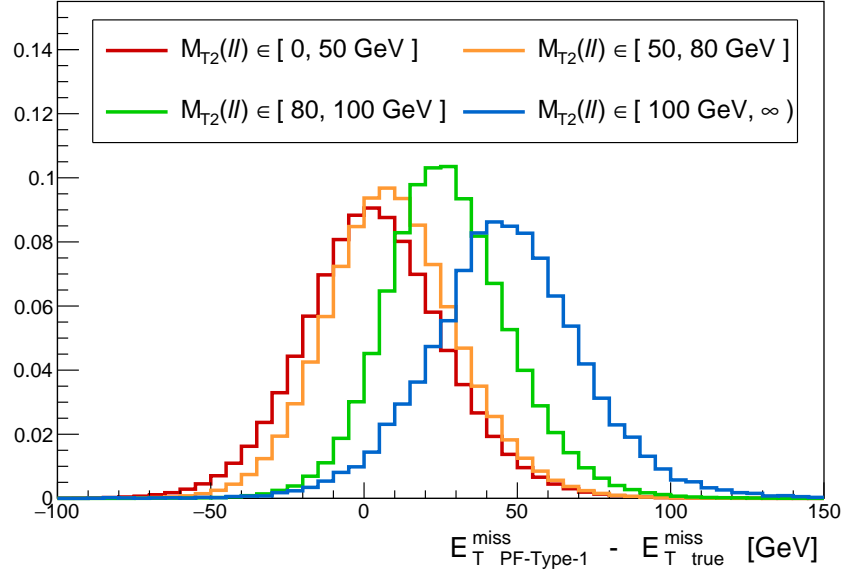where $\eta\ (\geq 0)$ is called the "learning rate".

Figure 5.10: Difference between reconstructed and generated (i.e. no detector effects) $E_{\mathrm{T}}^{\mathrm{miss}}$ in slices of $M_{\mathrm{T2}}(\ell\ell)$ for a simulated sample of $t\bar{t}$.
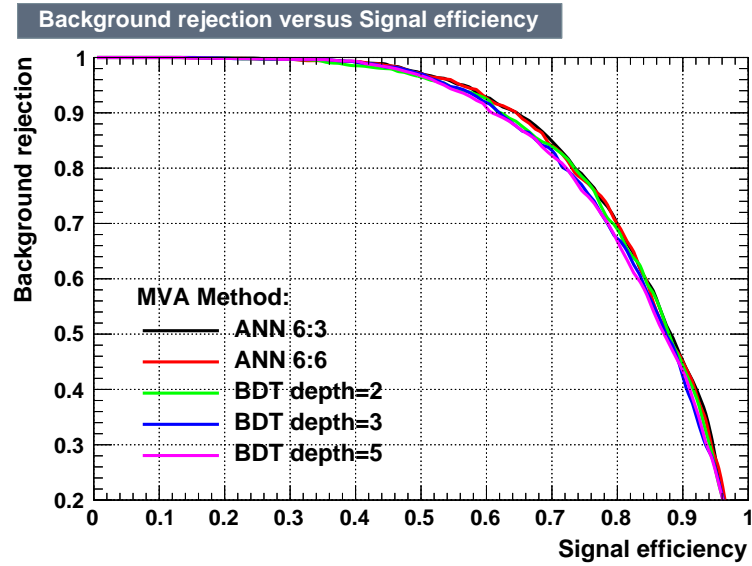

Figure 5.11: Proof of concept: background rejection versus signal efficiency for two ANN and three BDT realisations.

This search uses a separate ANN for each signal point —differences between their kinematics are apparent—, nonetheless all of them share a handful of features and parameters. They are presented in the following, together with a discussion about why they take such definitions and values.

- As shown in table 4.8, and further treated in chapter 6, the SM $t\bar{t}$ is the largest background by far. Thus, and for the sake of simplicity, the $t\bar{t}$ has been the sole **background** process which the ANNs have been trained against.

- The **architecture**: It refers to the number of neurons and their arrangement in layers. Several configurations have been tried and evaluated in terms of their background rejection versus signal efficiency curves. All them had in common: four neurons at the input layer; two hidden layers, m and n neurons each; and one output layer, one neuron. The different choices of m and n, detailed at the legends of figure 5.12, are: 3 and 3, 6 and 3, 6 and 6, and 9 and 6. One can observe there how the configuration $m = 6$, $n = 3$ for both the lightest and the heaviest scalar $t\bar{t}$+DM cases prevails.

  Thus, the "6:3" is the chosen architecture, a schematic view of it is given in figure 5.13.

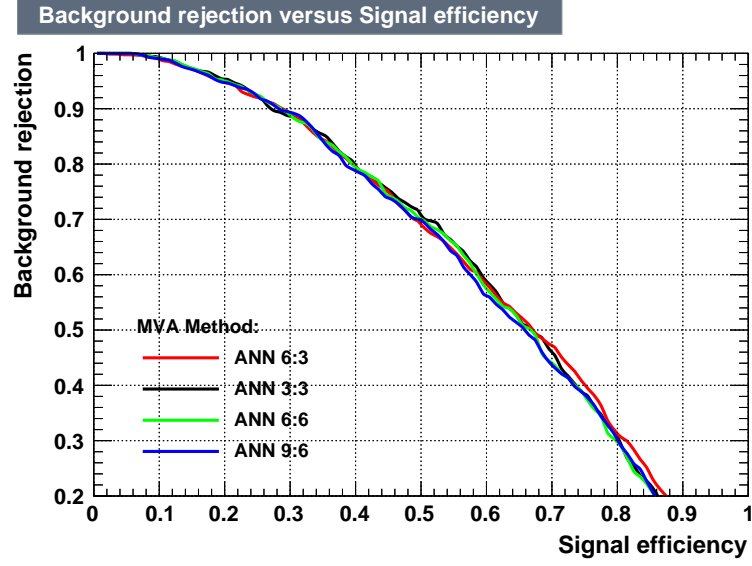- For all the neurons, the **synapse function**, κ, is a raw sum:

$$\kappa\left(y_1^{(\ell)}, y_2^{(\ell)}, ..., y_n^{(\ell)} \mid w_0^{(\ell)}, w_1^{(\ell)}, w_2^{(\ell)}, ..., w_n^{(\ell)}\right) = w_0^{(\ell)} + \sum_{i=1}^{n} y_i^{(\ell)} w_i^{(\ell)}. \tag{5.18}$$

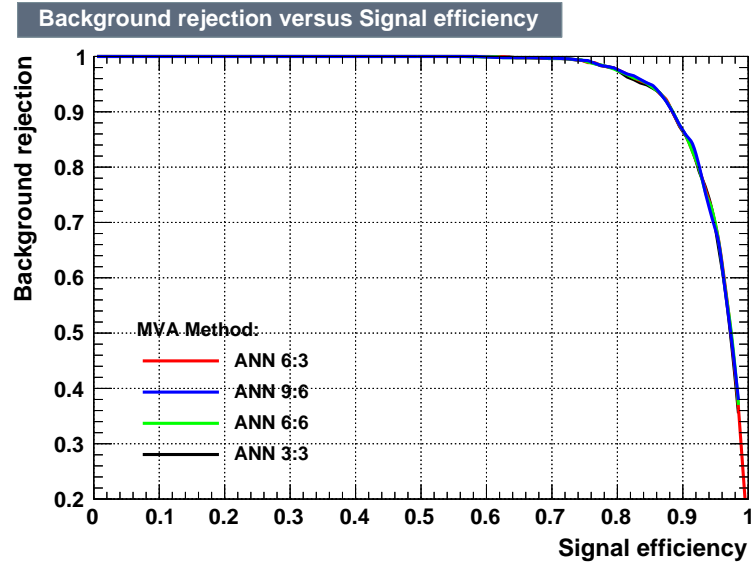- For all the neurons, the **activation function**, α, is an hyperbolic tangent:

$$\alpha(x) = \frac{e^x - e^{-x}}{e^x + e^{-x}}. \tag{5.19}$$

  The sigmoid function was also tried:

$$\alpha(x) = \frac{1}{1 + e^{-x}}. \tag{5.20}$$

(a)

(b)

Figure 5.12: Background rejection versus signal efficiency for four types of ANN architectures. Signal role played by (a) $m_S = 10$ GeV $t\bar{t}+$DM and (b) $m_S = 500$ GeV $t\bar{t}+$DM.

However, in the two (extremal) cases presented in figure 5.14 its performance was slightly worse.

- The **number of training events** N_{training}, is one thousand for signal plus another thousand for background. The same amounts applies to the **number of test events**, N_{test}.

  Two requirements drive the choice: First, the number of training events must be large enough to resolve all the weights. Given the architecture (4:)6:3(:1), the size of $\vec{w}$ is almost sixty, so this condition is satisfied by far ($N_{\text{training, sig}} + N_{\text{training, bkg}} = 2000$). Second, one cannot use training and test events later for the classification. At the same time, one would want to keep as many events as possible on this set in order not to depend on the statistics, which in our case concerns straight to the signal samples. Therefore, a compromise must be sought.

  A good way to achieve it is by looking at the overtraining test. Overtraining alarms blink if the number of free parameters of the model (i.e. number of weights) is not justified given the number of training events. But, although more rarely, they could also do so if training and test samples kept some distinctive feature in the end, i.e. if they do not represent each other.

  Figure 5.15 shows the ANN-output distribution for both the training and the test sets superimposed (and normalised the larger one to the smaller one) for three different choices of N_{training} and N_{test}. No overtraining is appreciated in none of them. However, it is quite clear that the smaller the training sample, the cruder the separation between the signal and the background.

- The **learning rate**, η, used in equation (5.3) and the **number of cycles**, N_{cycl}, (or, equivalently, number of updates of $\vec{w}$) go hand in hand, thus they are adjusted simultaneously. A look at the "convergence test" helps to make the choice. The check, figure 5.16, shows the $\mathcal{E}(\vec{w})$ distance defined in equation (5.3) for every iteration and for both the training and the test samples. One would expect the training curve (red) to be a monotonically decreasing function, whereas the test curve

(blue) should exhibit a minimum at some point. Just rightwards, the overtraining starts to grow. If this pattern is not found is may be due to too large or small learning rate and/or too few number of cycles.

The final choice here has been $\eta = 0.01$ and number of cycles $N_{\mathrm{cycl}} = 500$ (figure 5.16(d)).

The spectrum of the ANN-output variable, y_{ANN}, for every signal point is displayed in figures 5.17 and 5.18 for the 2016 integrated luminosity. No significant deviation is observed between the data and the SM background. Nonetheless, y_{ANN} will be put to good use in chapter 7 to set exclusion limits. The impact of each one of the four variables fed to the ANNs will be rated in terms on those very exclusion limits; therefore, one needs to go first through chapter 7 where they are introduced. Ratings themselves are given in appendix A.
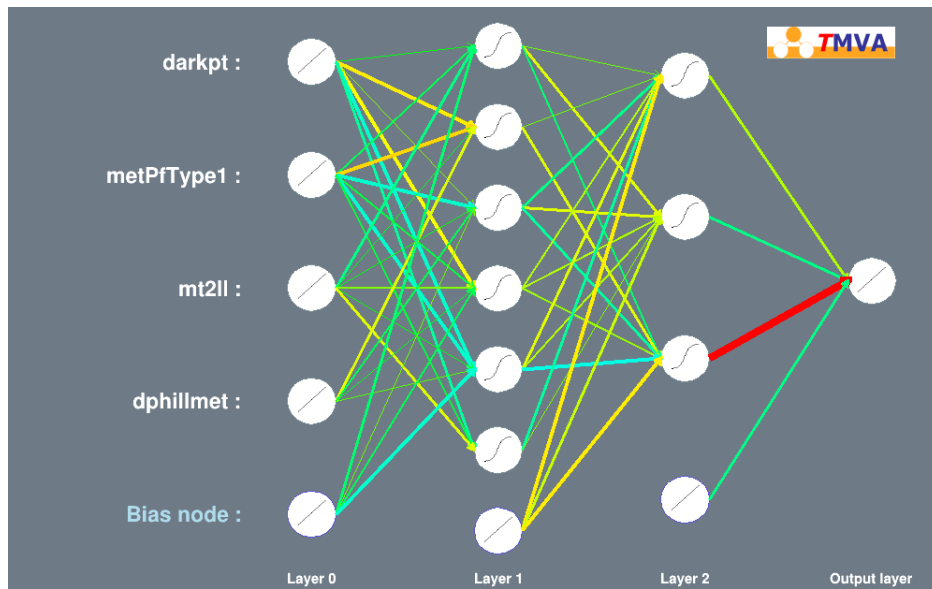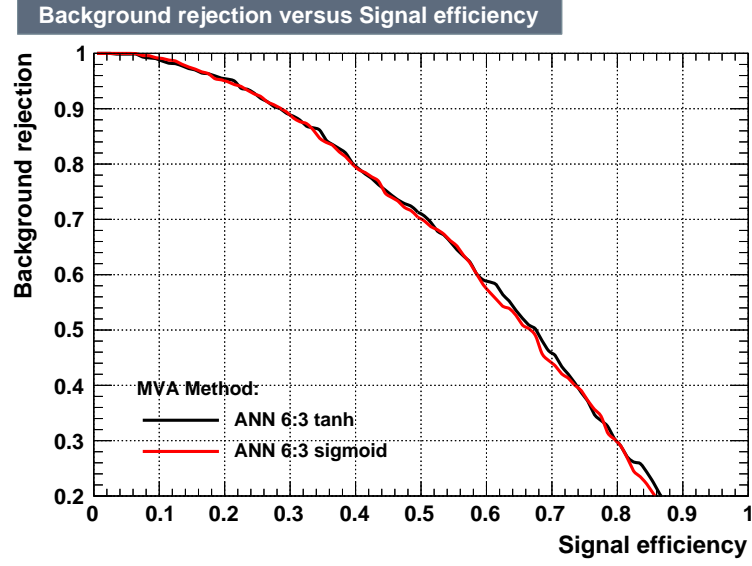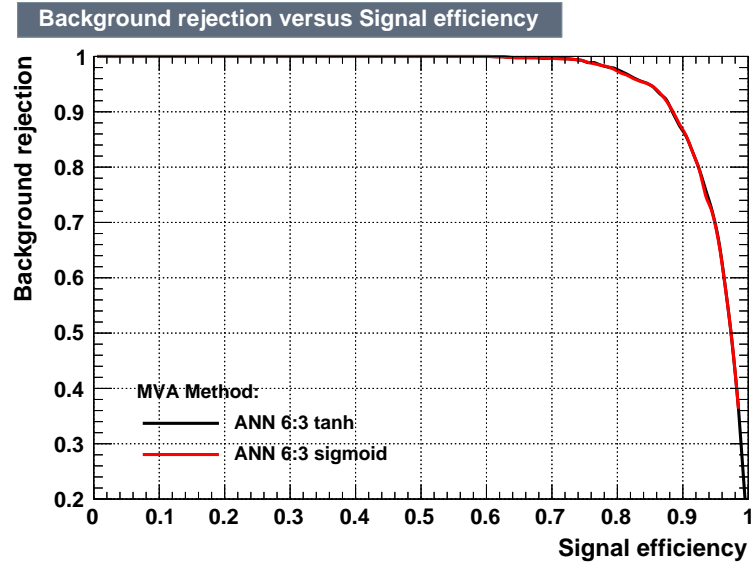
Figure 5.13: The "6:3" architecture shared by all the ANNs. The bottom neuron of the layers 0 (initial), 1 and 2 (hidden) sends a constant value to all the neurons on the next layer, except for its counterpart there.

(a)

(b)

Figure 5.14: Background rejection versus signal efficiency for two neuron activation functions. Signal role played by (a) $m_S = 10$ GeV $t\bar{t}$+DM and (b) $m_S = 500$ GeV $t\bar{t}$+DM.
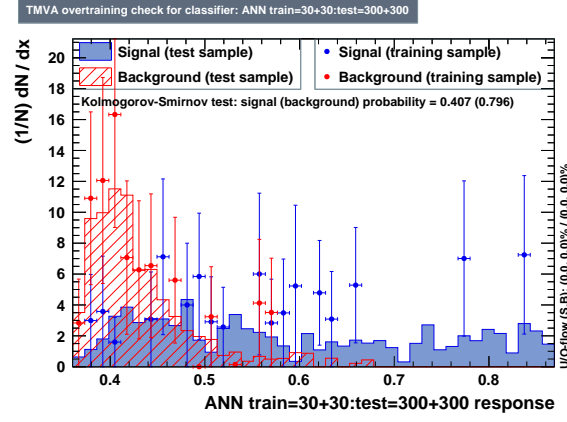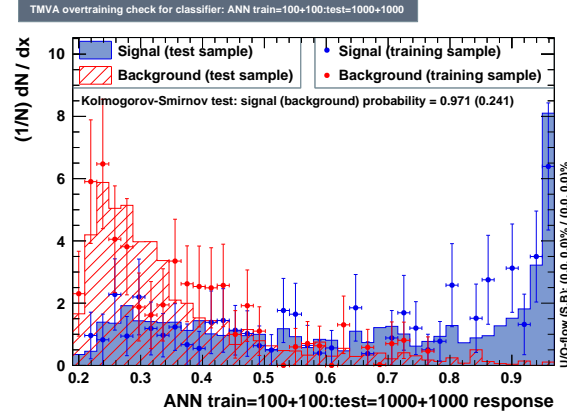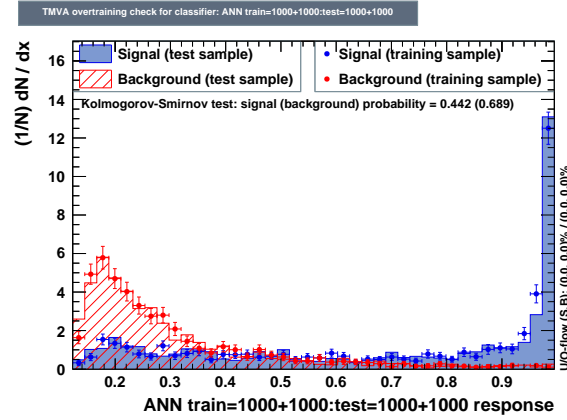
(a) $N_{\text{training}} = 30 + 30$, $N_{\text{test}} = 300 + 300$

(b) $N_{\text{training}} = 10^2 + 10^2$, $N_{\text{test}} = 10^3 + 10^3$

(c) $N_{\text{training}} = 10^3 + 10^3$, $N_{\text{test}} = 10^3 + 10^3$

Figure 5.15: Training and test distributions (the latter normalised to the former) for different choices of N_{training} and N_{test}.

(a) $\eta = 1.0$, $N_{\mathrm{cycl}} = 100$

(b) $\eta = 1.0$, $N_{\mathrm{cycl}} = 500$

(c) $\eta = 0.01$, $N_{\mathrm{cycl}} = 500$

(d) $\eta = 0.01$, $N_{\mathrm{cycl}} = 100$

(e) $\eta = 0.001$, $N_{\mathrm{cycl}} = 100$

(f) $\eta = 0.001$, $N_{\mathrm{cycl}} = 500$
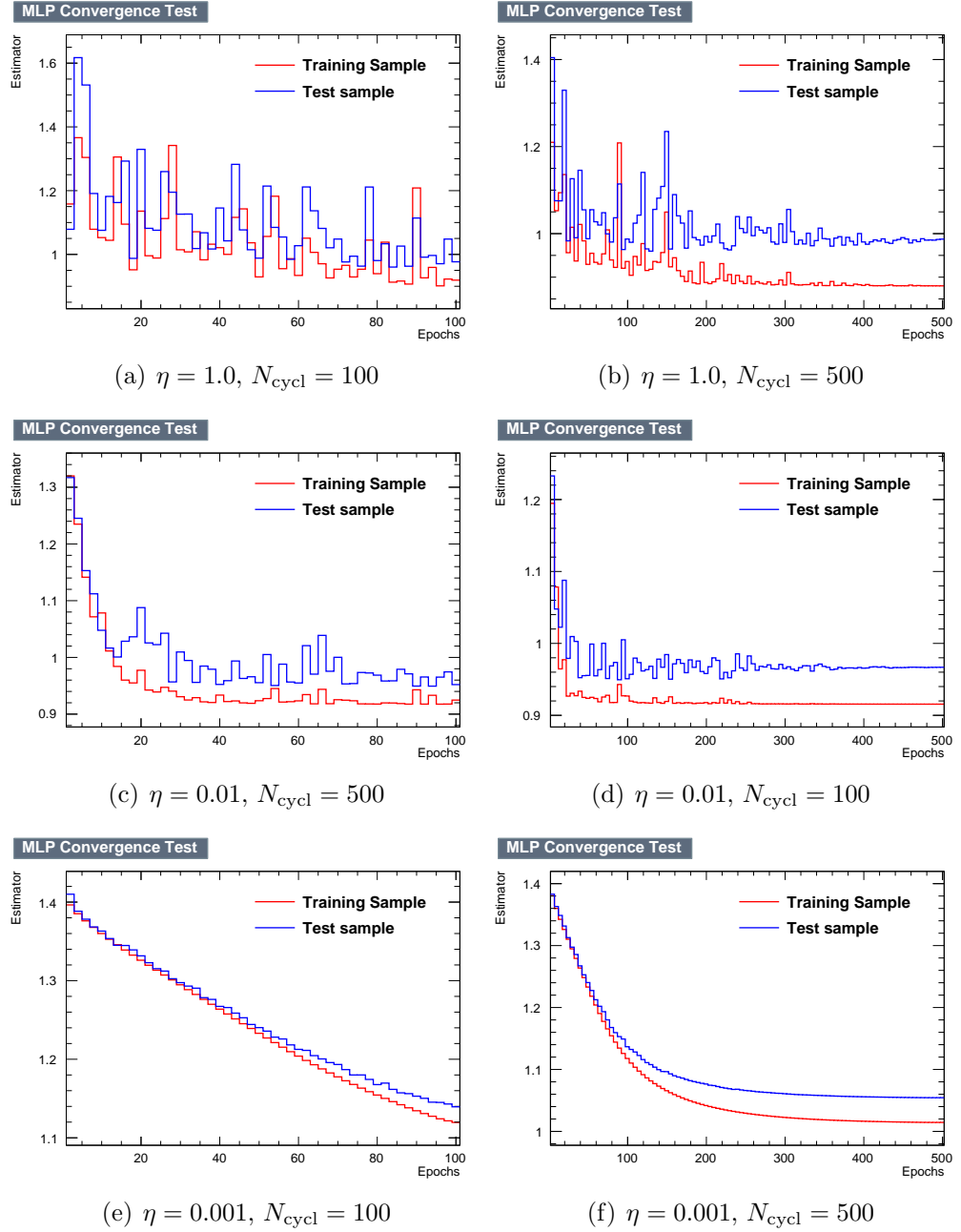
Figure 5.16: Convergence tests for three different learning rates and number of cycles.

(a) $m_\phi = 10$ GeV

(b) $m_\phi = 20$ GeV

(c) $m_\phi = 50$ GeV

(d) $m_\phi = 100$ GeV

Figure 5.17: ANN-output spectra for different scalar models. Uncertainties are statistical only. Signals are scaled by different factors.

(e) $m_\phi = 200$ GeV

(f) $m_\phi = 300$ GeV

(g) $m_\phi = 500$ GeV

Figure 5.17: ANN-output spectra for different scalar models. Uncertainties are statistical only. Signals are scaled by different factors (cont.)

(a) $m_\phi = 10$ GeV

(b) $m_\phi = 20$ GeV

(c) $m_\phi = 50$ GeV

(d) $m_\phi = 100$ GeV

Figure 5.18: ANN-output spectra for different pseudoscalar models. Uncertainties are statistical only. Signals are scaled by different factors.

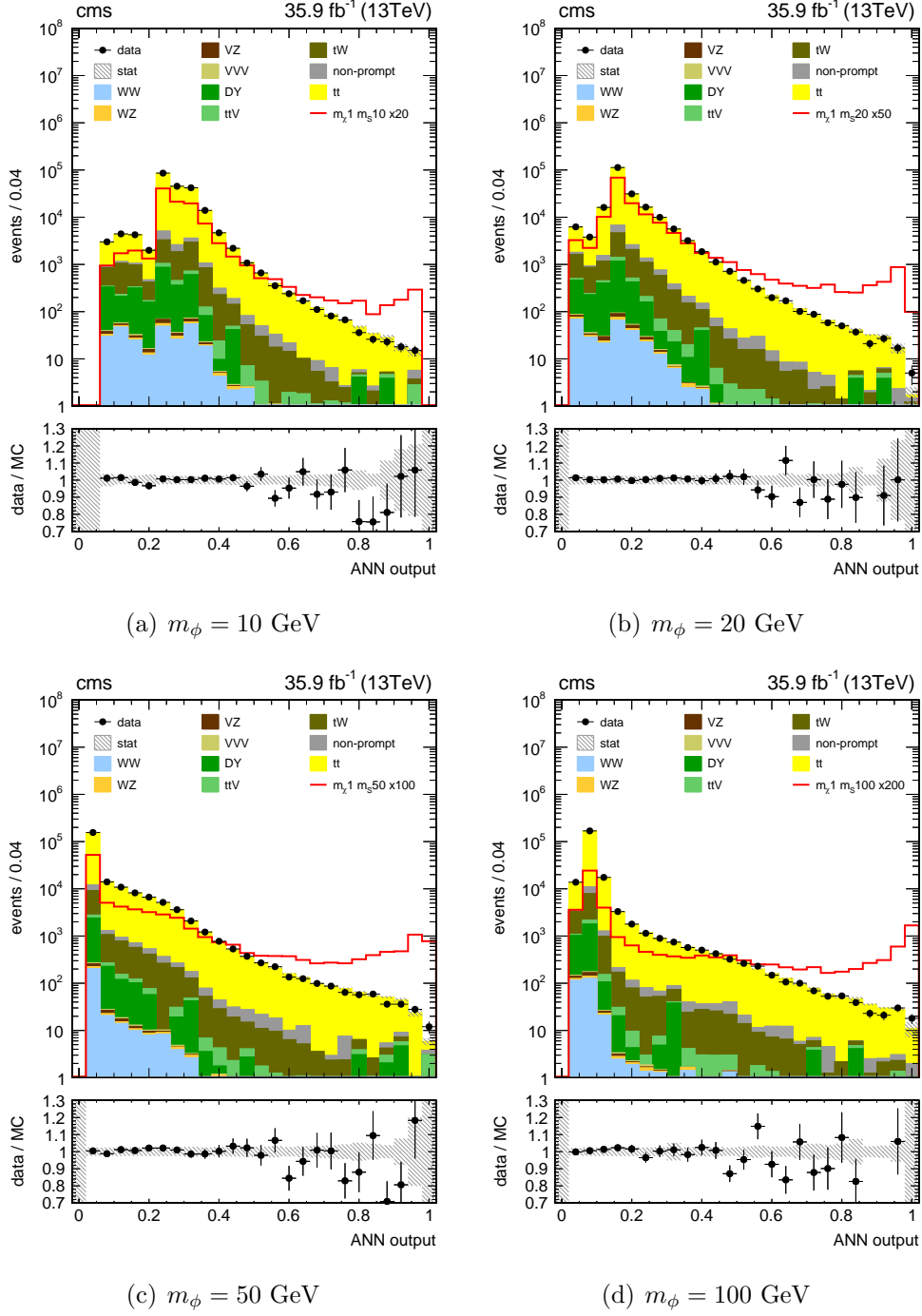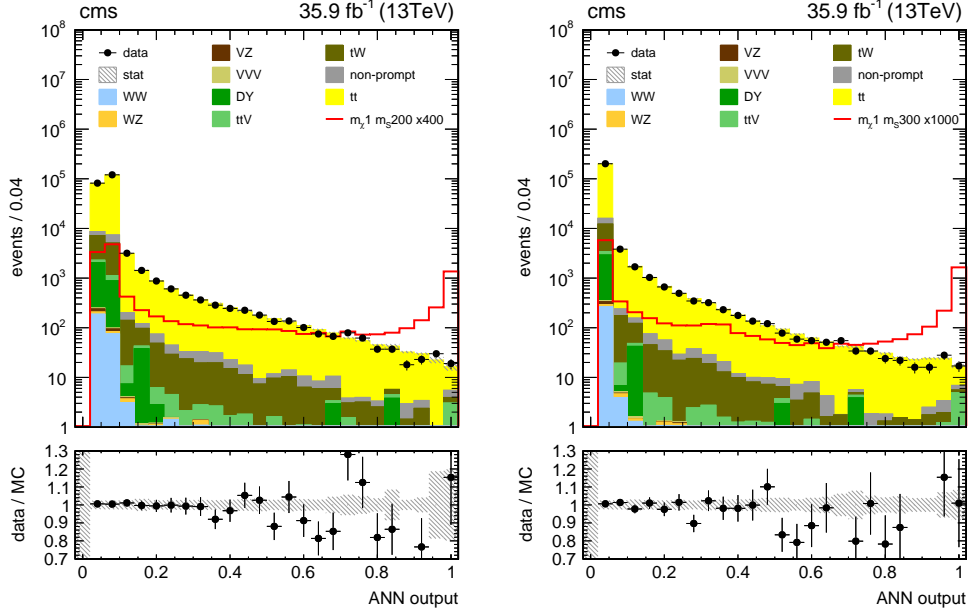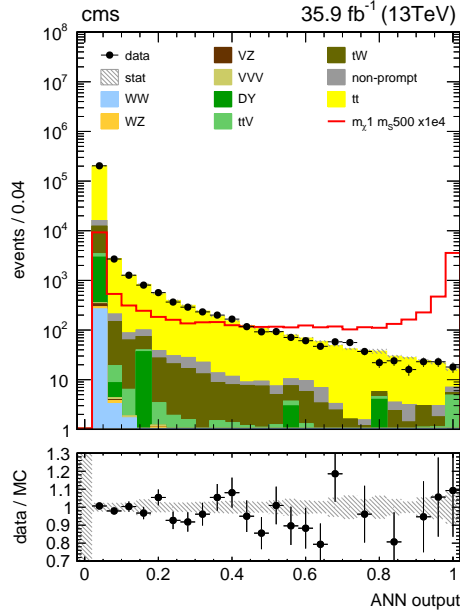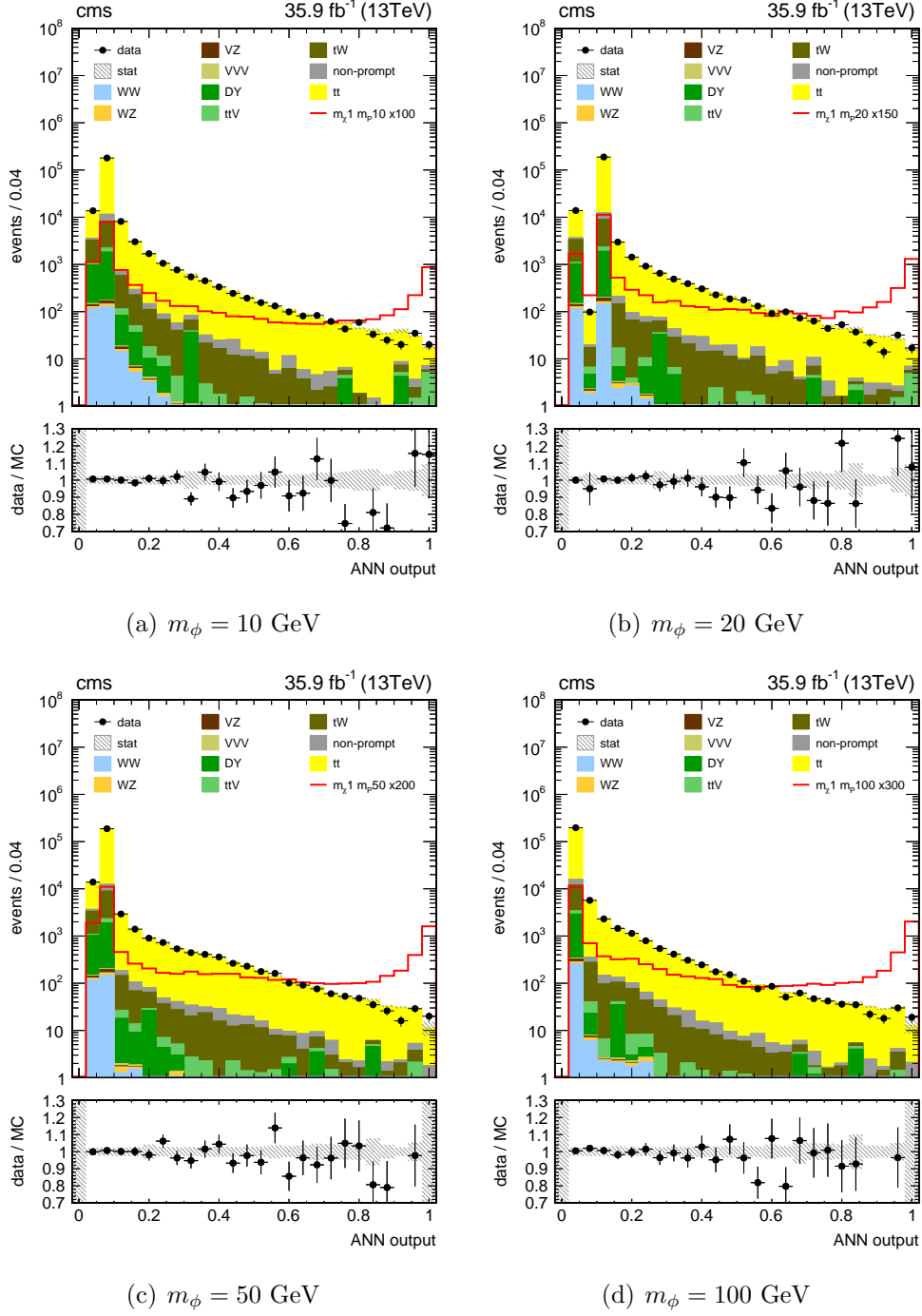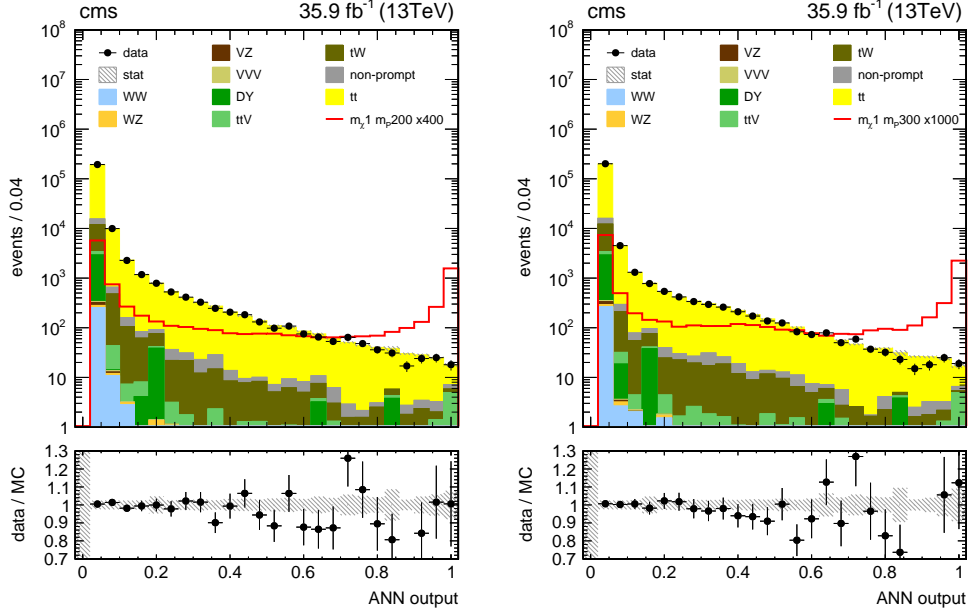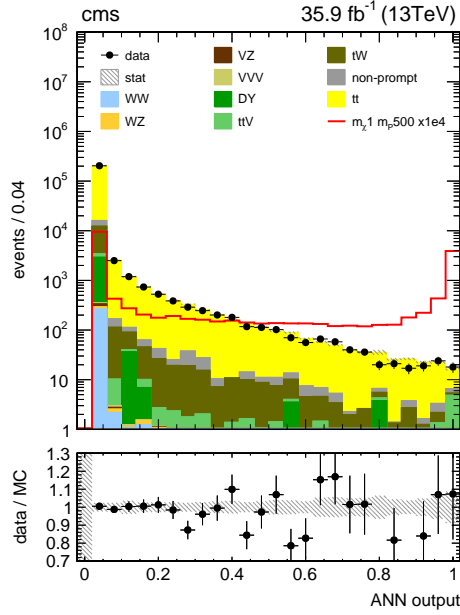(e) $m_\phi = 200$ GeV

(f) $m_\phi = 300$ GeV

(g) $m_\phi = 500$ GeV

Figure 5.18: ANN-output spectra for different pseudoscalar models. Uncertainties are statistical only. Signals are scaled by different factors (cont.)

Chapter 6

Background prediction

This chapter will deal with the estimation of the background processes. Needless to say, this is one of the major tasks, given that the tighter the background prediction, the more believable or significant the deviations.

Yields of the fifth column on table 4.8 have been converted here to percentages (and reordered) to state clearly the importance of every background process, see table 6.1. As one can appreciate, the $t\bar{t}$ process takes the lead by far. Nonetheless, gross amounts are not sufficient: one has also to consider kinematic similarities with respect to the signal. This is the case of the $t\bar{t}$V, which in spite of being the fifth contribution, could become identical to the $t\bar{t}$+DM, leaking from the typical background bins to the signal ones.

Dedicated sections will be devoted to the processes: $t\bar{t}$, non-prompt lepton background and Z+jets. Notwithstanding the source their estimation was based on, the rest will be taken directly from MC. My main contributions here have to do with the quality assessment of the MC predictions for the $t\bar{t}$ process.

process	$\ell\ell$
$t\bar{t}$	92.0 %
tW	4.4 %
non-prompt	1.9 %
Z+jets	1.2 %
$t\bar{t}$V	0.3 %
WW	0.1 %
WZ	<0.1 %
VZ	<0.1 %
VVV	<0.1 %
total bkg.	100.0 %

Table 6.1: Relative contributions of the background processes once applied the selection listed in table 4.7.

6.1   The main background: $t\bar{t}$

As mentioned several times, the $t\bar{t}$ process constitutes the main background of this analysis. Although eventually it has been taken from MC as is, a control region was defined and its behaviour checked through a scale factor data-MC.

The control region was delimited by the selection contained in table 4.7 from which a cut on $M_{\mathrm{T2}}(\ell\ell)$ variable was added, see figure 5.9(d): $M_{\mathrm{T2}}(\ell\ell) <$ 80 GeV.

The scale factor per bin of $M_{\mathrm{T2}}(\ell\ell)$ was computed as:

$$\mathrm{SF}_{t\bar{t}} = \frac{N_{\mathrm{data}} - N_{\mathrm{bkg}}}{N_{t\bar{t}}}, \tag{6.1}$$

where N_{bkg} refers to the count of all the other background processes. The values of $\mathrm{SF}_{t\bar{t}}$ against $M_{\mathrm{T2}}(\ell\ell)$ are provided in figure 6.1, along with a fit to a constant over the whole range. Moreover, two more fits were carried out just varying the range: [40, 80 GeV] and [70, 80 GeV]. Their results are given in table 6.2. Apart from statistical uncertainties, they are also affected by systematic effects such as those due to the jet energy scale, PDFs, etc.

(section 7.2) as well as the potential signal contamination. The combined uncertainty has been estimated to account for up to 7%. The three fits are compatible with each other and also with $\mathrm{SF}_{t\bar{t}} = 1$.

Provided the great agreement in this control region, we decided to rely on our $t\bar{t}$ MC. Furthermore, we cannot afford to give up all the signal events with $M_{\mathrm{T2}}(\ell\ell) < 80$ GeV due to statistics limitation, specially for lower mediator masses.

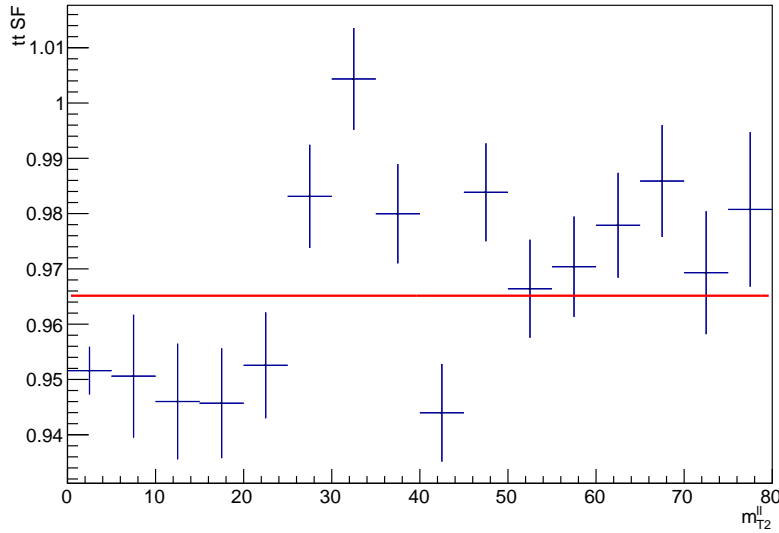Figure 6.1: $\mathrm{SF}_{t\bar{t}}$ per bin of $M_{\mathrm{T2}}(\ell\ell)$. In red, their fit to a constant. Notice the vertical axis starting at 0.93.

fit range	$\mathrm{SF}_{t\bar{t}}$
[0, 80 GeV]	0.966 ± 0.014
[40, 80 GeV]	0.962 ± 0.003
[70, 80 GeV]	0.966 ± 0.009

Table 6.2: Fitted-to-constant $\mathrm{SF}_{t\bar{t}}$ for different ranges. Uncertainties are statistical only.

6.2   Non-prompt lepton background

As detailed in chapter 4, this search is based on the selection of events
with one or more charged isolated high-quality leptons, usually referred to
as "prompt". However, there might be additional leptons and even non-
leptonic particles which fulfil those selection criteria, giving rise to so-called
"non-prompt lepton background".

In the case of electrons, these include contributions from semileptonic decays
of b and c quarks, photon conversions and jets with large electromagnetic
energy. Non-prompt muons can also originate from semileptonic decays of
b and c quarks, from charged hadron decays in the tracking volume or in
hadronic showers, or from high-energy pions passing through the calorimeters
(punch-through).

The overall non-prompt lepton background contribution is accounted for
from data, by applying a general tight-to-loose method which provides a
way to measure the yields and the kinematic distributions of this contami-
nation [103]. Essentially, it consists in defining a control region enriched in
QCD using a looser particle selection criteria, where the rate of misidentifi-
cation is expected to be high. Data contained in it are used to compute an
extrapolation factor or "fake rate" (FR), lately applied to the signal region
where the search is performed.

The QCD-enriched control region starts to be defined by requiring the fol-
lowing single lepton triggers paths:

- **Single Muon**

  ○ HLT_Mu8_TrkIsoVVL_v*

  ○ HLT_Mu17_TrkIsoVVL_v*

- **Single Electron**

  ○ HLT_Ele12_CaloIdM_TrkIdM_PFJet30_v*

       ◦ HLT_Ele23_CaloIdM_TrkIdM_PFJet30_v*

       ◦ HLT_Ele12_CaloIdL_TrkIdL_IsoVL_PFJet30_v*

       ◦ HLT_Ele23_CaloIdL_TrkIdL_IsoVL_PFJet30_v*

To effectively have a QCD-enriched sample, it is needed to get out of contributions from W or Z leptonic decays. Thus, several cuts are are demanded: to avoid the leptons from W decays, it is used $E_\mathrm{T}^\mathrm{miss} < 20$ GeV and $m_\mathrm{T} < 20$ GeV, whereas to reject those from the Z, only one lepton per event is required. Moreover, both muon and electron candidates are required to be well separated from the leading jet of the event: $\Delta\phi_{\ell\ell\,\mathrm{jet}} > 1$. However, provided that the subtraction is never complete, the presence of electroweak events could be estimated by using dedicated MC samples. In the coming plots, when this point applies, it will be marked by "With EWK correction".

The estimation of the FR is made by defining the so-called "fakeable" object, i.e. muon and electron objects passing only the cuts listed in table 6.3 and table 6.4, and fully selected objects, i.e. those able to pass the complete selection, table 4.7. The FR is then calculated as the ratio between these two quantities, within the QCD-enriched region, for both electrons and muons separately as a function of p_T and $|\eta|$:

$$\mathrm{FR}(p_\mathrm{T},\,\eta) = \left[\frac{N_\mathrm{tight}}{N_\mathrm{loose}}\right]_\mathrm{QCD\text{-}enrich.} \qquad (6.2)$$

The FR obtained in this way are represented in figure 6.2.

variable	requirement
is a PF muon	yes
is either global or tracker muon	yes

Table 6.3: "Muon Loose-ID" selection as defined in [119].

Additionally, the "prompt rate" (PR), defined as the rate of prompt leptons passing the tight selection, is also calculated before moving back to the signal region. It is computed in data as well by using a general tag and probe method within a Z enriched control region. The PR is then obtained by

(a)   (b)

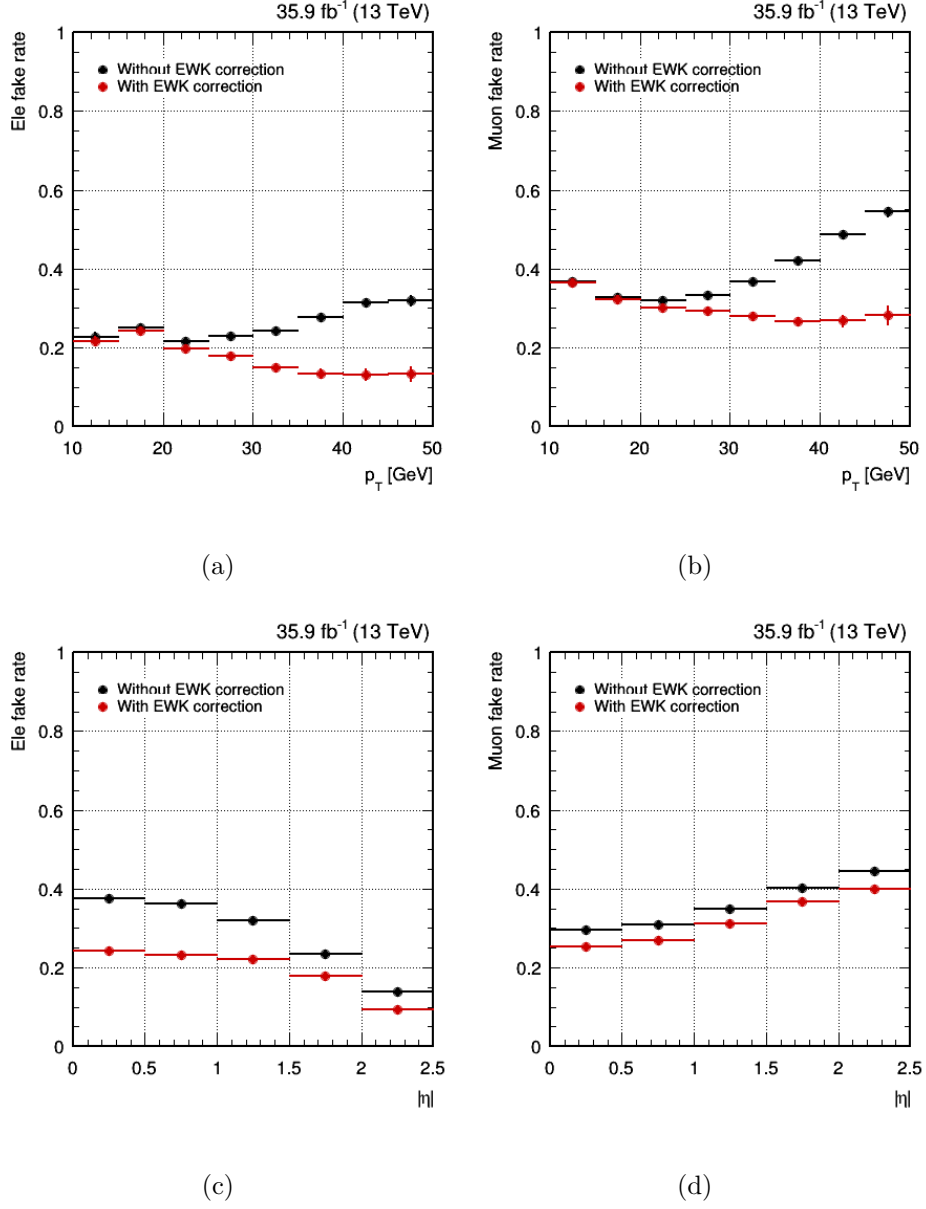(c)   (d)

Figure 6.2: FRs obtained within the QCD-enriched region for both electrons
(right) and muons (left), with respect to the lepton p_T (top) and $|\eta|$ (bottom),
with and without electroweak correction.

reconstructing the Z when at least one leading tight lepton is observed, and by dividing the number of tight by the number of loose trailing leptons.

$$\text{PR}(p_{\text{T}},\,\eta) = \left[\frac{N_{\text{tight}}}{N_{\text{loose}}}\right]_{Z\text{-enrich.}} \tag{6.3}$$

The results obtained in this way are represented in figure 6.3.

Next, the event selection detailed in table 4.7 but where the lepton IDs switch "tight" for "loose", i.e. table 4.4 for table 6.3 and table 4.5 for table 6.4, is applied to data.

The quantities, ε and ζ, are defined from the FR and the PR:

$$\varepsilon = \frac{\text{FR}}{1-\text{FR}}\,, \tag{6.4}$$

$$\zeta = \frac{1-\text{PR}}{\text{PR}}\,; \tag{6.5}$$

and from these, four weights:

$$w_{\text{p}_1\text{p}_2} = -\frac{\varepsilon_1\zeta_1 + \varepsilon_2\zeta_2}{(1-\varepsilon_1\zeta_1)(1-\varepsilon_2\zeta_2)}\,, \tag{6.6}$$

$$w_{\text{f}_1\text{f}_2} = -\frac{2\varepsilon_1\varepsilon_2}{(1-\varepsilon_1\zeta_1)(1-\varepsilon_2\zeta_2)}\,, \tag{6.7}$$

$$w_{\text{p}_1\text{f}_2} = -\frac{(1+\varepsilon_1\zeta_1)\varepsilon_2}{(1-\varepsilon_1\zeta_1)(1-\varepsilon_2\zeta_2)}\,, \tag{6.8}$$

$$w_{\text{f}_1\text{p}_2} = -\frac{\varepsilon_1(1+\varepsilon_2\zeta_2)}{(1-\varepsilon_1\zeta_1)(1-\varepsilon_2\zeta_2)}\,. \tag{6.9}$$

The total yield of the non-prompt lepton background is given by the sum of the four weights for every selected event. Results are provided in table 6.5.

The systematic uncertainty on the non-prompt lepton background is obtained from a validation region composed of same sign leptons. A flat 30% systematic uncertainty is assessed to this background to cover for the (dis)agreement

variable	requirement	
$\dfrac{E_{\mathrm{HCAL}}}{E_{\mathrm{ECAL}}}$	< 0.298	< 0.101
$\left\vert \dfrac{1}{E_{\mathrm{SC}}} - \dfrac{1}{p} \right\vert$	< 0.241	< 0.14
$\sigma_{\eta\eta}$	< 0.011	< 0.0314
$\vert\Delta\eta\vert$	< 0.00477	< 0.00868
$\vert\Delta\phi\vert$	< 0.222	< 0.213
relative isolation ($\Delta R < 0.3$)	< 0.0994	< 0.107
expected missing inner hits	≤ 1	≤ 1
conversion veto	yes	yes
transverse impact parameter	< 0.5 mm	< 1 mm
z distance of the track w.r.t. the PV	< 1 mm	< 2 mm

Table 6.4: "Electron Loose Cut-Based ID" as defined in [120]. The middle and the right columns refer to the barrel ($\vert\eta\vert < 1.479$) and the endcaps ($\vert\eta\vert > 1.479$), respectively

	ee	$\mu\mu$	$e\mu$	$\ell\ell$
non-prompt	250. ± 31	1447 ± 35	2283 ± 63	3979 ± 78

Table 6.5: Yields for the non-prompt lepton background estimated from data. Uncertainties are statistical only.
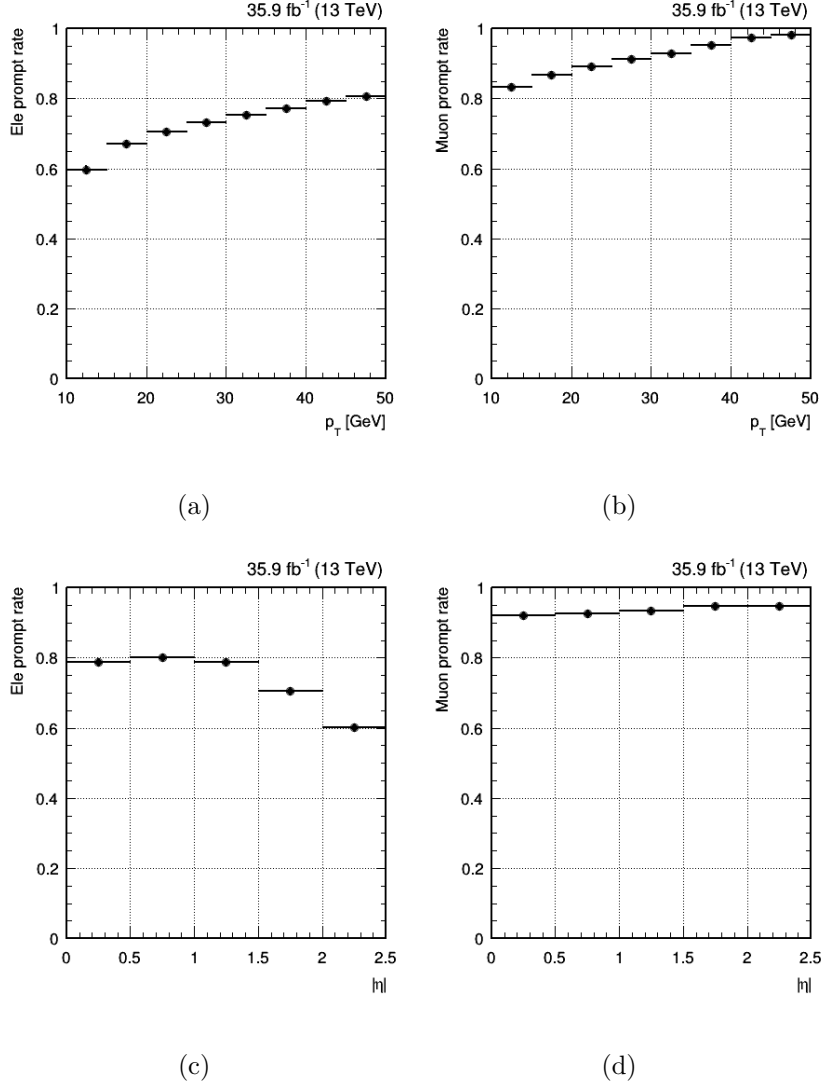
Figure 6.3: PRs obtained by applying a general tag and probe method within a Z enriched region for both electrons (left) and muons (right), with respect to the lepton p_T (top) and $|\eta|$ (bottom).

between the prediction and the observation, see figure 6.4.

(a)   (b)

Figure 6.4: Distribution of the invariant mass of the two same-sign leptons in the validation region for the (a) 0-jet bin and the (b) 1-jet bin. Uncertainties are statistical only.

6.2.1 Drell-Yan background

While simulation is used to estimate the shape of the Drell-Yan process in the designated signal region, data event yields within 15 GeV of M_Z are used to determine its normalisation . The ratio (R) of yields within 15 GeV of M_Z to yields outside this mass window constitute the data to MC normalisation scale factors. The predicted Drell-Yan normalisation, N_{DY}, is extrapolated from the observed Drell-Yan yield inside the Z boson mass window, N_{in}, according to,

$$N_{\mathrm{DY}} = N_{\mathrm{in}} \frac{R_{\mathrm{MC}}^{0b}}{R_{\mathrm{MC}}^{1b} \cdot R_{\mathrm{Data}}^{0b}}. \tag{6.10}$$

The quantity denoted as R_{MC}^{1b} is the ratio computed in Drell-Yan simulation with all other analysis requirements applied. To account for potential mis-modelling of the data mass shape by the simulation, additional ratios are

computed in data and simulation with a zero b-tag requirement, denoted R^{0b}_{Data} and R^{0b}_{MC}, respectively.

Non-Drell-Yan processes, namely dileptonic $t\bar{t}$, are subtracted in the computation of N_{in} and R^{0b}_{Data}. The $t\bar{t}$ to $e\mu$ decays are used to predict the ee or $\mu\mu$ contribution after adjusting for reconstruction and identification efficiency differences between electrons and muons, given the assumption that the branching ratios to electrons and muons are equal. The uncertainty on the Drell-Yan normalisation is dominated by the statistical uncertainty on N_{in} and R^{1b}_{MC} (around 15%).

The results obtained in this way are offered in figure 6.5. The maximum gap between their central values ($\sim 30\%$) is taken as systematic uncertainty.
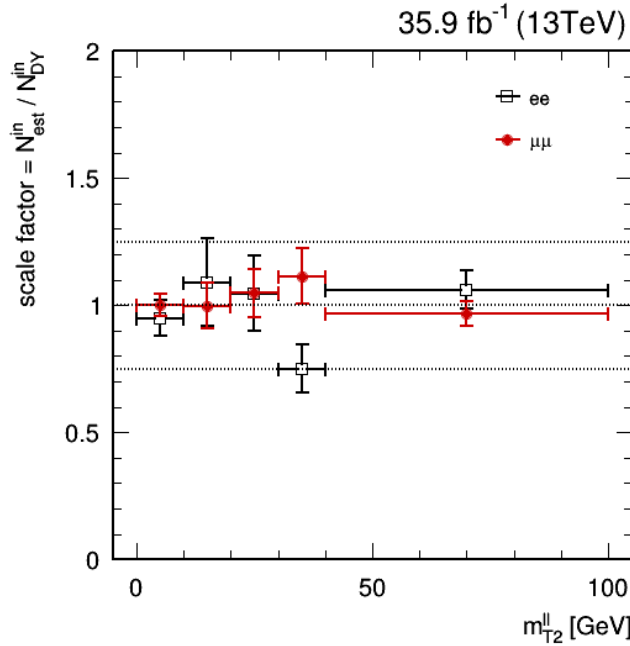

Figure 6.5: Scale factor obtained from the data-driven method applied to the Drell-Yan process as a function of $M_{\text{T2}}(\ell\ell)$ for the same flavour channels, where its contribution is significant. Uncertainties are statistical only.

The so-estimated yields of the Drell-Yan background are provided in ta-

ble 6.6.

	ee	$\mu\mu$	$e\mu$	$\ell\ell$
Drell-Yan	717 ± 124	1492 ± 198	402 ± 57	2610 ± 240

Table 6.6: Yields for the non-prompt lepton background estimated from data. Uncertainties are statistical only.

6.3 Other backgrounds

The rest of the background processes are directly taken from MC simulations. They are scaled to the recorded luminosity (35.9 ± 0.9 fb^{-1}) according to the cross sections they were generated with. As detailed in section 4.1.2, these are however known up to some grade of precision. Therefore, a (theoretical) systematic effect will be associated to them.

Chapter 7

Results

The final chapter is devoted to the interpretation of our data in terms of exclusion limits on the signal strength. To present it in a comprehensible way, it starts —section 7.1— by a minimal introduction of the statistical procedure followed. Section 7.2 deals with the systematic effects the search is affected by. It says which ones they are, how they have been estimated and how they are treated going into the statistical interpretation. Lastly, section 7.3 gives the final numbers, the hierarchy of systematics, and a few comments on them.

My main contributions here have to do with the estimation of some systematics and the understanding of their impact on the search, the arrangement of the numerical input provided to our "official" statistical tool, and with the interpretation of the results returned.

7.1 Statistical interpretation

Provided the statistical nature of every measurement, one has to judge the compatibility amongst prediction and observation on statistical grounds.

The previous section has had as purpose to build a variable, y_{ANN}, for which

some values were typical of the background processes whereas some others were of the signal.

The expected count for every bin in which y_{ANN} is partitioned is:

$$e_i = b_i + \mu s_i \, , \tag{7.1}$$

where b_i and s_i are the (expected) number of background and signal events in the ith bin, respectively. The μ parameter, the so-called signal strength, will be used to release the normalisation of the signal; it does not depend on the bin.

The numbers b_i and s_i can be viewed as derived from:

$$b_i \;=\; B(\vec{\theta}_{\mathrm{b}}^{\mathrm{norm}}) \int_{\mathrm{bin}\,i} f_{\mathrm{b}}(y_{\mathrm{ANN}};\, \vec{\theta}_{\mathrm{b}}^{\mathrm{shape}})\, dy_{\mathrm{ANN}} \, , \tag{7.2}$$

$$s_i \;=\; S \int_{\mathrm{bin}\,i} f_{\mathrm{s}}(y_{\mathrm{ANN}};\, \vec{\theta}_{\mathrm{s}}^{\mathrm{shape}})\, dy_{\mathrm{ANN}} \, . \tag{7.3}$$

The functions $f_{\mathrm{b}}(y_{\mathrm{ANN}};\, \vec{\theta}_{\mathrm{b}}^{\mathrm{shape}})$ and $f_{\mathrm{s}}(y_{\mathrm{ANN}};\, \vec{\theta}_{\mathrm{s}}^{\mathrm{shape}})$ must be read as the probability density functions of y_{ANN} for the background and the signal, where $\vec{\theta}_{\mathrm{b}}^{\mathrm{shape}}$ and $\vec{\theta}_{\mathrm{s}}^{\mathrm{shape}}$ are the nuisance parameters affecting their shapes, linked to most of the systematics and bin-by-bin statistical uncertainties, as detailed in section 7.2.

The quantities $B(\vec{\theta}_{\mathrm{b}}^{\mathrm{norm}})$ and S represent the total number of background and signal events. On one hand, S is not treated as an adjustable parameter, but remains fixed to the value predicted by the nominal signal model.[1] On the other hand, $B(\vec{\theta}_{\mathrm{b}}^{\mathrm{norm}})$ will be allowed to float according to the nuisance parameters $\vec{\theta}_{\mathrm{b}}^{\mathrm{norm}}$ in order to account for those systematic effects just affecting its normalisation.

All the nuisance parameters are included under $\vec{\theta}$: $\vec{\theta} = \{\vec{\theta}_{\mathrm{b}}^{\mathrm{norm}}, \vec{\theta}_{\mathrm{b}}^{\mathrm{shape}}, \vec{\theta}_{\mathrm{s}}^{\mathrm{shape}}\}$.

The observed count for every bin in which y_{ANN} is partitioned is named o_i.

---

[1]As mentioned above, the signal normalisation will be absorbed by the μ parameter.

Given μ and $\vec{\theta}$, the probability of obtaining o_i events in every bin is known as the likelihood function, $\mathcal{L}(\mu, \vec{\theta})$. It is the product of Poisson probabilities for all the bins multiplied by the product of the case-specific probabilities for all the nuisances parameters, here generically represented by ρ_j, and determined in section 7.2:

$$\mathcal{L}(\mu, \vec{\theta}) = \prod_i \frac{[b_i(\vec{\theta}) + \mu s_i(\vec{\theta})]^{o_i}}{o_i!} e^{-[b_i(\vec{\theta} + \mu s_i(\vec{\theta})]} \prod_j \rho_j(\theta_j) \,. \qquad (7.4)$$

Two hypotheses have now to be tested against each other: the background-only hypothesis ($\mu = 0$) versus the signal+background hypothesis ($\mu = 1$). Moreover, one would like to state which values of μ above some threshold: $\mu > \mu_{\text{up}}$ are discarded at some confidence level.

Provided that no significant excess is observed in figures 5.17 and 5.18 the test for discovery will not be carried out.

In order to set upper limits on the signal strength, μ, the test statistic $\tilde{q}_\mu$, introduced in reference [128], is used:

$$\tilde{q}_\mu = -2 \ln \frac{\mathcal{L}(\mu, \hat{\theta}_\mu)}{\mathcal{L}(\hat{\mu}, \hat{\theta})}, \qquad 0 \leq \hat{\mu} \leq \mu \,, \qquad (7.5)$$

where $\hat{\theta}_\mu$ is the value of $\vec{\theta}$ which, given μ (and the observed data, of course), maximises $\mathcal{L}$, i.e. it is the conditional maximum-likelihood estimator of $\vec{\theta}$. The denominator is the maximised unconditional likelihood function, i.e. $\hat{\mu}$ and $\hat{\theta}$ are the maximum-likelihood estimators of μ and $\vec{\theta}$, respectively.

Concerning the constraints, on one hand, $0 \leq \hat{\mu}$ means that the signal has to be always additive. On the other hand, $\hat{\mu} \leq \mu$ is enforced to guarantee a one-sided confidence interval, i.e. not detached from zero. In other words: upwards fluctuations of the observed data such that $\hat{\mu} > \mu$ are not considered as evidence against a μ-strong signal+background hypothesis.

Once explained equation (7.5), the procedure, broadly described at [129], runs as follows:

1. Given the observed data and chosen μ, compute the value of the test statistic according to equation (7.5): $\tilde{q}_\mu^{\mathrm{obs}}$. Furthermore, save $\hat{\theta}_\mu^{\mathrm{obs}}$.

2. Given the observed data, find the value of $\vec{\theta}$ which maximises $\mathcal{L}(\mu, \vec{\theta})$ for $\mu = 0$: $\hat{\theta}_0^{\mathrm{obs}}$.

3. Build the probability density functions of the test statistic under the assumption of $\{\mu, \hat{\theta}_\mu^{\mathrm{obs}}\}$ (signal+background hypothesis) and the assumption of $\{\mu = 0, \hat{\theta}_0^{\mathrm{obs}}\}$ (background-only hypothesis) by using either toy MC pseudodata or the asymptotic formulas derived in [128]. They will be represented by $f(\tilde{q}_\mu \,|\, \mu, \hat{\theta}_\mu^{\mathrm{obs}})$ and $f(\tilde{q}_\mu \,|\, 0, \hat{\theta}_0^{\mathrm{obs}})$, respectively.

4. From $f(\tilde{q}_\mu \,|\, \mu, \hat{\theta}_\mu^{\mathrm{obs}})$ and $f(\tilde{q}_\mu \,|\, 0, \hat{\theta}_0^{\mathrm{obs}})$, and $\tilde{q}_\mu^{\mathrm{obs}}$, two p-values are defined:

$$p_\mu\,(\mu) = P(\tilde{q}_\mu \geq \tilde{q}_\mu^{\mathrm{obs}} \,|\, \mu, \hat{\theta}_\mu^{\mathrm{obs}}) = \int_{\tilde{q}_\mu^{\mathrm{obs}}}^{\infty} f(\tilde{q}_\mu \,|\, \mu, \hat{\theta}_\mu^{\mathrm{obs}}) \, d\tilde{q}_\mu \,, \qquad (7.6)$$

$$p_{\mathrm{b}}\,(\mu) = P(\tilde{q}_\mu < \tilde{q}_\mu^{\mathrm{obs}} \,|\, 0, \hat{\theta}_0^{\mathrm{obs}}) = \int_{-\infty}^{\tilde{q}_\mu^{\mathrm{obs}}} f(\tilde{q}_\mu \,|\, 0, \hat{\theta}_0^{\mathrm{obs}}) \, d\tilde{q}_\mu \,. \qquad (7.7)$$

From p_μ and p_{b}, the $\mathrm{CL_s}$ ratio is defined like [130, 131]:

$$\mathrm{CL_s}(\mu) = \frac{p_\mu}{1 - p_{\mathrm{b}}} \,. \qquad (7.8)$$

5. To quote the $(1 - \alpha)$ $\mathrm{CL_s}$ confidence level upper limit on μ, tune this until $\mathrm{CL_s} = \alpha$. Usually, and in this thesis, $\alpha = 0.05$.

   The 95% $\mathrm{CL_s}$ upper limit obtained form observed data will be denoted by $\mu_{\mathrm{up,\,obs}}^{95\%}$.

When $\mu_{\mathrm{up,\,obs}}^{95\%}$ results will be presented, they will be accompanied by the sensitivity of the search, defined like the expectation ($\equiv$ median) value of μ, under the assumption of the background-only hypothesis, for which its $\mathrm{CL_s}$ is equal to $\alpha = 0.05$. It is denoted by $\mu_{\mathrm{up,\,exp}}^{95\%}$ and the precise calculation is explained below.

The target is to get a 95% CL$_\text{s}$ upper limit analogous to that one above, but starting not from the actual observed dataset, but from N simulated datasets, generated assuming the background-only hypothesis, i.e. $\{\mu = 0, \hat{\theta}_0^{\text{obs}}\}$. The following has to be taken into account for every one of them:

- For every μ under test, the value of the test statistic has to be computed according to equation (7.5): $\tilde{q}_\mu^{\text{exp}}$.

- The p-values defined by equations (7.6) and (7.7) are now computed switching $\tilde{q}_\mu^{\text{obs}}$ and $\tilde{q}_\mu^{\text{exp}}$.

- By varying μ, one has to find the particular value which gets CL$_\text{s}$ = 0.05: $\mu_{\text{up}}^{95\%}$.

A cumulative distribution can be built from the N instances of $\mu_{\text{up}}^{95\%}$, beginning with the lowers. The value at which the cumulative distribution intersects the 50% quantile is the median expected value, $\mu_{\text{up, exp}}^{95\%}$. The $\pm 1\sigma$ ($\pm 2\sigma$) band, $\mu_{\text{up, exp}\pm1\sigma}^{95\%}$ ($\mu_{\text{up, exp}\pm1\sigma}^{95\%}$), is defined by the 16% (2.5%) and 84% (97.5%) quantiles.

7.2   Systematics

Different sources of systematic uncertainty have been investigated, most of them affecting both the signal and the background, and implemented into the exclusion limit extraction procedure described in section 7.1 through the nuisance parameters, $\vec{\theta}$. The $\rho_j(\theta_j)$ functions introduced in equation (7.4) will be defined at the end of the section.

In a general way, their estimation means studying the effect of a well-defined variation on the ingredients of the analysis. Systematic uncertainties were always computed by repeating the analysis for every variation, but —it must be emphasised— with the original training of the ANN (remember: one training per signal point).

The following sources of systematic uncertainty, of which the foremost listed
are the predominant sources, were accounted for:

- **Jet energy scale (JES).** Reconstructed jet four-momenta in the sim-
  ulation are simultaneously varied according to the uncertainty on the
  jet energy scale. Jet energy scale uncertainties are coherently propa-
  gated to all observables including $E_\mathrm{T}^\mathrm{miss}$, $M_\mathrm{T2}(\ell\ell)$, and p_T^DM. Uncertainty
  effects due to the jet energy resolution were found to be negligible.

- **Factorization and renormalisation scales.** Uncertainties due to
  the renormalisation scale μ_R and the factorization scale μ_F in the sim-
  ulation matrix-element generator are modelled by varying the scales
  independently by a factor of 0.5 or 2, and by propagating the aver-
  age change to the distributions used in the fit. This is accommodated
  via weights obtained directly from the generator information in the
  MC simulation where available. The uncertainty is considered to be
  uncorrelated among the different background processes.

- **Unclustered energy.** The variation of the unclustered energy
  —ECAL and HCAL deposits not assigned to any object— is propa-
  gated to the $E_\mathrm{T}^\mathrm{miss}$ in the event. It is evaluated for all processes.

- **PDF uncertainties.** Uncertainties on the PDFs are estimated by re-
  weighting every event in each process with the NNPDF3.0 [132] one
  hundred replicas [133]. For a given process, let y_i^α the content of the
  ith bin of the observable y when the αth replica is applied. The PDF
  uncertainty of that bin is chosen to be the standard deviation, σ_i:

$$\sigma_i = \sqrt{\frac{\sum_\alpha \left(y_i^\alpha\right)^2}{100} - \left(\frac{\sum_\alpha y_i^\alpha}{100}\right)^2}. \tag{7.9}$$

- **Single top and diboson normalisation.** The expected yields for
  background processes are either scaled to data or to theory predictions
  with the best available accuracy. The uncertainties on the cross section
  predictions are taken into account in the PDF as well as renormalisa-

tion and factorization scale uncertainties. In the single top and dibo-son simulation samples, an uncertainty of 20% is assigned to the nor-malisations and these uncertainties are treated independently of each other [134, 135].

- **Pile-up modelling.** Systematic uncertainties due to pile-up modelling are taken into account by varying the minimum bias cross section of 69 mb used to calculate the data pileup distributions by $\pm5\%$ [114].

- **Luminosity.** An uncertainty of 2.5% is taken on the integrated luminosity of the data sample [92].

- **Lepton reconstruction and selection.** The uncertainty on lepton reconstruction and selection efficiency is associated with the efficiency measurement with samples of Z bosons decaying to dielectrons or dimuons. The p_{T}- and η-dependent scale factors are varied within their uncertainties which amounts to $\approx 2\%$ per lepton.

- **Lepton trigger.** The uncertainty on lepton triggering efficiency is associated with the efficiency measurement with samples of Z bosons decaying to dielectrons or dimuons. The corresponding uncertainty ranges from 1% to 2%.

- **b-tagging efficiency.** The b-tagging efficiency and the respective uncertainty is measured on independent control samples. Uncertainties from gluon splitting, the b quark fragmentation function, the selections used to define the control samples, etc. are propagated to the efficiency scale factors [136].

- **Simulation statistics.** Shape uncertainties due to the limited size of the simulated signal and background samples are included by allowing each bin of the distributions included in the signal extraction to fluctuate independently according to the statistical uncertainty on the simulation.

The following sources of systematic uncertainty are accounted for on the pertinent background processes in the signal region. The uncertainty associated

with the fake lepton background is the sole uncertainty applied to this process, where the rest are applied in addition to the aforementioned sources of systematic uncertainty.

- **Misidentified lepton background.** The sources of uncertainty on the misidentified lepton background stem from the statistical uncertainty of the single lepton control sample to which the rate is applied. A flat 30% was assigned as systematic uncertainty.

- **Drell-Yan background.** The dependency on $M_{\mathrm{T2}}(\ell\ell)$ of the Drell-Yan scale factor was studied in section 6.2.1; the maximum deviation found, 30%, was assessed as a systematic uncertainty.

- **Top p_{T} reweighting.** Differential measurements of top quark pair production show that measured p_{T} spectrum of top quarks is softer than in simulation. Scale factors to cover this effect are derived in previous CMS measurements [118] and are applied in the analysis by default. An associated systematic uncertainty is estimated by not applying the scale factor re-weighting.

From all of the systematics above, the next ones have been considered to affect the background normalisation, i.e. form $\vec{\theta}_{\mathrm{b}}^{\mathrm{norm}}$: luminosity, pile-up modelling, misidentified lepton background, Drell-Yan background and single top and diboson normalisation. For all of them, ρ is a log-normal distribution centred around zero whose width, σ, matches the corresponding estimation given above ($\sigma \equiv \tilde{\theta}$):

$$\rho(\theta) = \frac{1}{\sqrt{2\pi}\theta\tilde{\theta}} \exp\left[-\frac{1}{2}\left(\frac{\ln\theta}{\tilde{\theta}_i}\right)^2 \right]. \tag{7.10}$$

The rest of the systematics —jet energy scale, factorization and renormalisation scales, unclustered energy, PDF uncertainties, lepton reconstruction and selection efficiencies, lepton trigger, b-tagging efficiency, simulation statistics and top p_{T} reweighting— have been considered to affect either the background or the signal shapes, i.e. form $\vec{\theta}_{\mathrm{b}}^{\mathrm{shape}}$ and $\vec{\theta}_{\mathrm{s}}^{\mathrm{shape}}$. For all of them, ρ

is a product of as many Gaussian distributions as the number of bins (index i), centred at zero and whose width, σ_i, matches the difference between the nominal and the systematic-associated histograms for every bin ($\sigma_i \equiv \tilde{\theta}_i$):

$$\rho(\theta) = \prod_i \frac{1}{\sqrt{2\pi\tilde{\theta}_i^2}} \exp\left[-\frac{1}{2}\left(\frac{\theta}{\tilde{\theta}_i}\right)^2\right] . \tag{7.11}$$

7.3 Results

Expected and observed upper limits on μ have been calculated at 95% confidence level using the $\mathrm{CL_s}$ criterion described in section 7.1. They are plotted against the DM mediator masses in figure 7.1 as well as gathered in table 7.1.

First of all, differences in sensitivity (red dash lines) between both Lorentz structures are apparent: scalar models could be rejected up to 80 GeV approximately, whereas it would be hardly possible for any pseudoscalar mass. The cause has much to do with nominal cross sections. It must be remembered that for a mediator mass of 10 GeV, the cross section of the scalar model is forty times larger than the pseudoscalar one (table 4.3), which means that, not surprisingly, the separation is even better for the latter, provided that, roughly speaking, $\mu_{\mathrm{up,exp}}^{95\%}$ goes with $1/\sqrt{\sigma}$.

Observed limits come to confirm the expectations. In fact, all of them lie within the $\pm 1\sigma$ green band.

One can appreciate in figure 7.1(a), how a remarkable segment of the parameter line has been excluded. However, a kind of an aesthetic criteria is behind the choice $g_\mathrm{q} = 1$; in other words, one could continue the endeavour by exploring other accessible regions of the space $\{m_\chi, m_\phi, g_\chi, g_\mathrm{q}\}$.

The quality of the estimation of every systematic as well as their relative importance have been evaluated by means of the "pulls" and "impacts" plot. Its concept, contents and interpretation will be explained below in relation
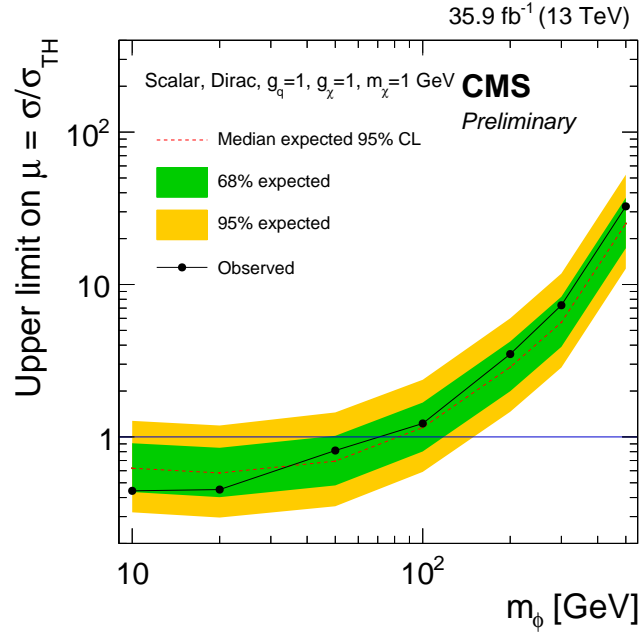
(a)
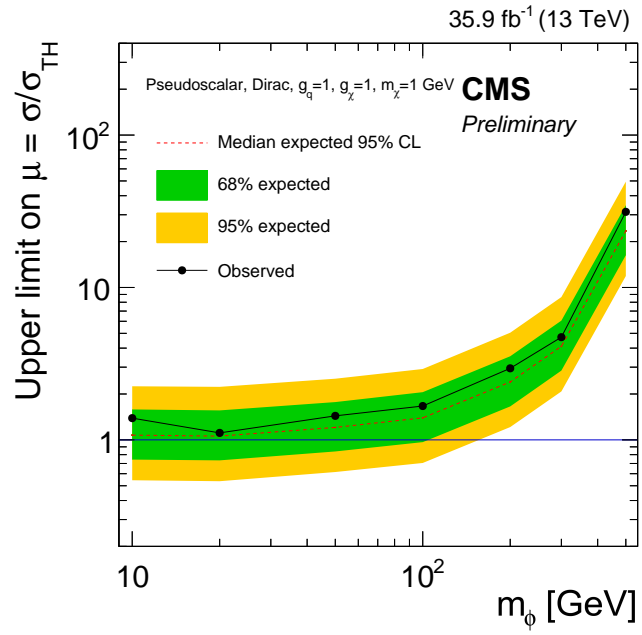
(b)

Figure 7.1: Expected and observed upper limits on the signal strengt, μ, for (a) scalar and (b) pseudoscalar models with $m_\chi = 1$ GeV and $g_q = g_\chi = 1$.

to the illustrative example provided in figure 7.2. Plots referring to every signal point are given in appendix B.

On one hand, by quality of the systematic estimation we refer to the difference between the maximum-likelihood estimator of θ_j, i.e. $\hat{\theta}_j$ and our preliminary estimation: $\tilde{\theta}_j$, relative to the latter. They are given in the central part of the figure 7.2. Error bars take the value of the ratio of the uncertainty on $\hat{\theta}_j$ to $\tilde{\theta}_j$ itself.

On the other hand, the importance of every systematic is graded according to the effect on μ when the associated nuisance, and just that one, is varied. Specifically, the "impact" is defined like the shift on the maximum likelihood estimator of μ, i.e $\hat{\mu}$, induced by moving $\hat{\theta}_j$ by $\pm 1\sigma$, leaving the other nuisance parameters fixed. Their values are given in the right side of figure 7.2. They drive the ordering of the list.

Regarding the particular interpretation of figure 7.2: First of all, dots moved rightwards (leftwards) from zero means overestimation (underestimation) of the associated systematic. This is clearly the case of the "JES" systematic. One has to conclude that taking its shape into account is helping to reduce it. Secondly, a short error bar means that the corresponding systematic could be estimated with a great accuracy thanks to the fit of the largest background ($t\bar{t}$) in the low range of the ANN spectrum, which is indeed working as a control region (fit $\equiv$ $t\bar{t}$-normalisation). Such is the case for the

m_ϕ [GeV]	scalar		pseudoscalar	
	expected	observed	expected	observed
10	0.62	0.44	1.07	1.39
20	0.58	0.45	1.06	1.11
50	0.69	0.81	1.21	1.44
100	1.15	1.23	1.39	1.67
200	2.87	3.50	2.40	2.95
300	5.64	7.31	4.11	4.72
500	25.13	32.56	23.50	31.35

Table 7.1: Expected and observed upper limits on μ for scalar and pseudoscalar models with $m_\chi = 1$ GeV and $g_\mathrm{q} = g_\chi = 1$.
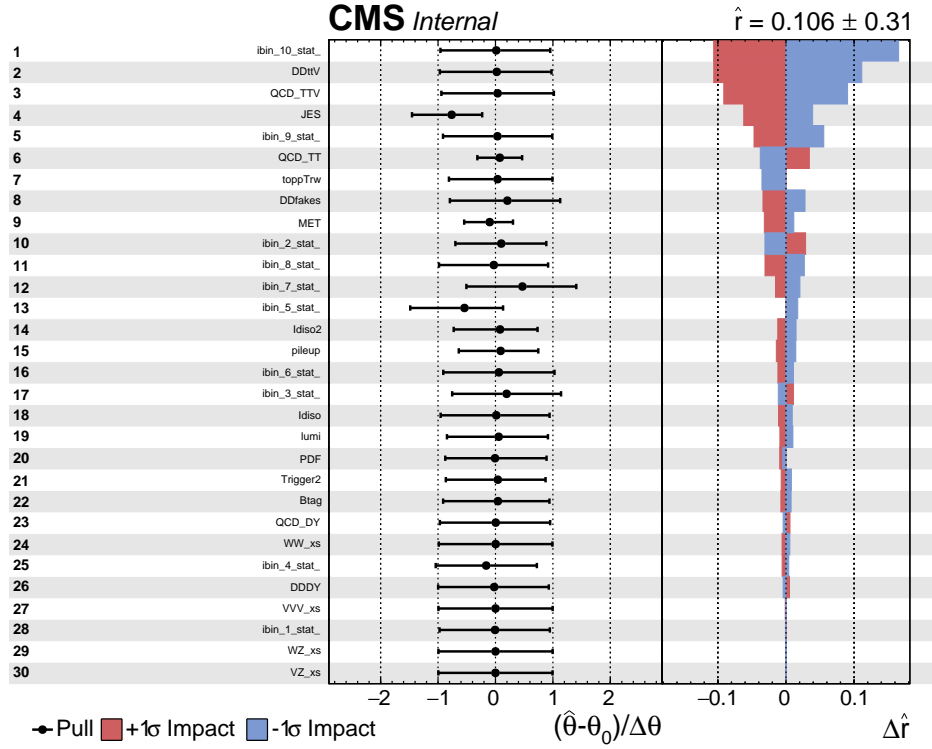
Figure 7.2: An illustrative example of the pulls and impacts plot (the chosen signal point is the 100 GeV scalar mediator). Impacts are shown on the right side by solid blue and red bars. They drive the ordering of the list. Nuisance names (according to the datacard nomenclature) and numbers are displayed on the left side. As it can be seen, only the first thirty are listed. Pulls come in the middle by dots and bars. The $\hat{r}$ value at the top right-hand corner is the maximum-likelihood estimator of μ, i.e. $\hat{r} \equiv \hat{\mu}$. The label "$(\hat{\theta} - \theta_0)/\Delta\theta$" might be confusing. What it actually means is "$(\hat{\theta} - \tilde{\theta})/\tilde{\theta}$". All the fourteen plots are given in appendix B.

"JES", "QCD_TT" and "MET" nuisances.

However, when one looks at the impacts (solid bars), he can observe how the statistical uncertainty for the most signal-like bin has, in general, a greater importance to fix $\hat{\mu}$, which means that the (small) size of the MC signal samples has an effect worthy of consideration. As one can observe in appendix B, this is actually the case for practically all the signal points. One can also realise how the MET systematic gains importance as the mediator mass increases (which is quite natural), whereas the JES systematic behaves the other way round. QCD systematics show a big and constant importance according to this ranking.

Conclusions

I have carried out a search of DM in association with $t\bar{t}$ pairs decaying dilep-
tonically using 35.9 ± 0.9 fb^{-1} of proton-proton collisions at $\sqrt{s} = 13$ TeV
produced by the LHC and recorded by the CMS detector at CERN during
2016. I have not found evidence of DM and limits on the signal strength
have been determined. To conclude this, a succession of steps was followed:

First of all, knowing the signature of the signal, I have chosen my triggers
and tried different initial selections in order to reject most of the background
processes. This has required to consider progressive object definitions as well
as going through a series of key observables such as E_T^miss, the p_T of both the
first and the second leptons, their invariant mass, etc. To make the final
choice, I have had to keep in mind the limited number of simulated events
for the signal samples.

In order to improve the separation between the signal and the main back-
ground, an observable rooted in the kinematic reconstruction of $t\bar{t} \to 2\ell$ has
been developed. It has aimed at getting the $\vec{p}_\text{T}$ of the DM component in
$t\bar{t}$+DM events, against the $t\bar{t}$-likeness of potential $t\bar{t}$ ones. Apart from the in-
herent issues to the $t\bar{t} \to 2\ell$ reconstruction itself, I have needed to think of a
way to proceed with the associated quartic equation when it has no solution.
My proposal has lied in quantifying its non-solvability by means of a function
which depends on E_T^miss, and next, to minimise it in order to obtain a new
E_T^miss value, considering the typical of the $t\bar{t}$ part. The difference between
this one and the original one has been assigned to the DM component.

The method is capable of reproducing the p_T of the DM, specially for high

values of p_T. Nonetheless, I consider it to be rather primitive, therefore it will be worth further exploration to extract the p_T in a more precise way. It could be decisive for future searches where a $t\bar{t}$ decays dileptonically with additional real E_T^{miss} wherever it comes from, e.g. DM, neutralinos, heavy Z' bosons going to neutrinos, etc.

To increase the separation power of the new observable along with some others, a multivariate analysis based on ANNs has been implemented. A great deal of study has been carried out to define, optimise and verify their performance. Eventually, I have achieved partial but unambiguous separation between the signal and the background, but no excess of data has been observed anywhere, i.e. everything agrees with the SM so far. Advances could come from a deeper exploitation of these machine learning techniques.

I have reckoned my SM backgrounds from different techniques. The $t\bar{t}$ MC has been validated in a region of $M_{\mathrm{T2}}(\ell\ell)$; the non-prompt lepton background and the Drell-Yan process have been estimated by two distinct data-driven methods. The rest of the backgrounds have been directly taken from MC simulations.

I have set upper limits on the strengths of my signal models. I have excluded $t\bar{t}$+DM for a DM mass of 1 GeV and a mediator mass up to 80 GeV when the latter couples both visible and invisible sectors with scalar structure and strength of one. Unfortunately, I cannot claim anything yet when the Lorentz structure is pseudoscalar. Thus, I would recommend to extend these searches both by refining or improving the strategy presented here and by recording further data. Moreover, it would be worth extending the search to other regions of the $\{m_\chi, m_\phi, g_\chi, g_q\}$ parameter space, because $g_\chi = g_q = 1$ is just the initial step.

This search for $t\bar{t}(2\ell)$+DM has been part of a joint effort within the CMS collaboration where three strategies have been deployed. Although independent from each other, they have agreed on common object definitions, background estimation methods or systematics treatment. Such a close interaction has turned out to be hugely useful for the three teams: continuous cross-checks

have allowed us to detect quite a few errors and to offer solid as well as compatible results.

Subsequently, one of the other two approaches (due to its higher simplicity) has joined the $t\bar{t} + $DM combination —all hadronic + semileptonic + dileptonic channels— which CMS has performed with the same data set ($\mathcal{L} = 35.9 \pm 0.9$ fb^{-1}). Under the same conditions, i.e. $m_\chi = 1$ GeV and $g_\chi = g_{\mathrm{q}} = 1$, it has come to exclude up to $m_\phi = 165$ GeV (223 GeV) for scalar (pseudoscalar) models, being the strongest limit given by CMS at low mass for collider spin-0 mediated DM with the 2016 data set. Where the dileptonic channel more effectively contributes is in the low mass region ($\lesssim 100$ GeV) for scalar mediator models, being even better than the semileptonic contribution there.

It is worth stating again the pros and cons of the $t\bar{t}(2\ell)+$DM search with respect to the other two channels: On one hand, the $t\bar{t} \to 2\ell$ branching ratio is the lowest: $^1/_9$ versus $^4/_9$ for either the semileptonic or the fully hadronic channels; furthermore, part of the information of the $t\bar{t} \to 2\ell$ decay is missing because of the neutrinos. On the other hand, the way in which leptons can be identified is much more clean, efficient, which in turns allows to constrain backgrounds tightly and avoids large uncertainties. Thus, keep studying the $t\bar{t}(2\ell)+$DM case might not be crucial, but will be quite helpful in the future. In addition, I recommend strongly to pursue the $\vec{p}_{\mathrm{T}}^{\mathrm{DM}}$ reconstruction, investigating in depth the dependencies on $E_{\mathrm{T}}^{\mathrm{miss}}$ of both the $t\bar{t}+$DM and the $t\bar{t}$ cases.

Conclusiones

En esta tesis se ha llevado a cabo una búsqueda de materia oscura (DM) en asociación con pares de quark top, $t\bar{t}$, en el canal dileptónico con 35.9 ± 0.9 fb^{-1} de colisiones protón-protón a $\sqrt{s} = 13$ TeV producidas en el LHC y recogidas con el experimento CMS del CERN durante el año 2016. No se han hallado evidencias de DM y se han fijado límites de exclusión en las secciones eficaces. Para poder concluir esto, se ha tenido que seguir una serie de pasos:

En primer lugar, conocida la topología de la señal, se han escogido los triggers y se han probado distintas selecciones iniciales con el propósito de eliminar la mayoría de los fondos. Esto ha requerido considerar definiciones progresivas de los objetos así como examinar una sucesión de observables tales como la energía transversa perdida, $E_{\mathrm{T}}^{\mathrm{miss}}$; el momento transverso, p_{T}, del primer y segundo leptones; su masa invariante; etc. A la hora de tomar una decisión, se ha tenido presente que el número de sucesos generados para las muestras de señal es reducido, lo que puede hacer que cobre relevancia la incertidumbre estadística.

Con objeto de incrementar la separación entre la señal y el fondo principal, se ha desarrollado una variable inspirada en la reconstrucción cinemática de la desintegración $t\bar{t} \to 2\ell$. Prentende obtener el $\vec{p}_{\mathrm{T}}$ de la componente DM, en los sucesos $t\bar{t} + \mathrm{DM}$, por oposición al carácter $t\bar{t}$ de potenciales sucesos $t\bar{t}$. Aparte de las dificultades inherentes a la propia reconstrucción $t\bar{t} \to 2\ell$, ha sido preciso pensar una manera de tratar la ecuación cuártica asociada cuando carece de solución. La propuesta ha consistido en cuantificar su irresolubilidad por medio de una función que depende de $\vec{E}_{\mathrm{T}}^{\mathrm{miss}}$, y, a continuación,

minimizar ésta y obtener así un nuevo valor de $\vec{E}_\mathrm{T}^\mathrm{miss}$, considerado como el propio de la parte $t\bar{t}$. La diferencia entre éste y el original se ha atribuido a la componente DM, $\vec{p}_\mathrm{T}^\mathrm{DM}$.

El método es capaz de reproducir el p_T de la DM, sobre todo para valores altos de p_T. No obstante, se considera que es todavía primitivo, y por tanto, merece la pena desarrollar más la investigación para extraer el p_T de modo más preciso. Esto podría ser decisivo en futuras búsquedas donde el $t\bar{t}$ se desintegre a dos leptones, con $E_\mathrm{T}^\mathrm{miss}$ real adicional, cualquiera que sea su origen: DM, neutralinos, bosones Z' pesados que se desintegraran a neutrinos, etc.

Con el propósito de aumentar la capacidad de separación de la nueva variable y de otras, se ha efectuado un análisis multivariable basado en redes neuronales. A la postre, se ha podido conseguir una separación parcial pero inequívoca entre la señal y el fondo. Sin embargo, no se ha observado ningún exceso; dicho de otro modo: las observaciones son compatibles con el modelo estándar (SM). En cualquier caso, se podrían dar avances ahondando la explotación de éstas u otras técnicas de machine learning.

Se han estimado los fondos SM por medio de diferentes técnicas. La simulación del proceso $t\bar{t}$ ha sido validada en una región de $M_{\mathrm{T}2}(\ell\ell)$; el fondo de leptones "non-prompt" y el proceso Drell-Yan se han estimado a partir de zonas de control usando datos. El resto de fondos han sido obtenidos por simulaciones Monte Carlo (MC).

Se han establecido límites a la intensidad de la señal de nuestros modelos. Se ha excluido $t\bar{t}+$DM para masa de DM de 1 GeV ($m_\chi = 1$ GeV) y mediador escalar de masa de hasta 80 GeV ($m_\phi \lesssim 80$ GeV), acoplado tanto al sector visible como al invisible con intensidad uno ($g_\mathrm{q} = 1$). Desafortunadamente, no podemos pronunciarnos con respecto a los mediadores pseudoescalar. Así, se recomienda extender esta búsqueda mediante la recolección de más luminosidad y/o mejorando la estrategia presentada aquí. Además, animamos a dirigir la búsqueda a otras regiones de espacio de parámetros $\{m_\chi, m_\phi, g_\chi, g_\mathrm{q}\}$, puesto que $g_\chi = g_\mathrm{q} = 1$ es no más que la elección trivial.

Esta búsqueda de $t\bar{t}(2\ell)$+DM ha formado parte de un análisis conjunto de la colaboración CMS que ha integrado tres estrategias. Si bien independientes entre sí, las tres han adoptado una definición común de los objetos, los mismos métodos de estimación de fondo o el mismo tratamiento de los errores sistemáticos, lo que se ha revelado de una gran utilidad para los tres equipos: los controles recíprocos nos han permitido detectar fallos y ofrecer unos resultados sólidos y compatibles entre sí.

Posteriormente, una de las otras dos estrategias, por su facilidad para la combinación, se ha incorporado a la combinación $t\bar{t}$+DM (canales hadrónico + semileptónico + dileptónico) que la colaboración CMS ha llevado a cabo con los mismos datos ($\mathcal{L} = 35.9 \pm 0.9$ fb^{-1}). Ésta, en idénticas condiciones, $m_\chi = 1$ GeV y $g_\chi = g_\mathrm{q} = 1$, ha logrado excluir hasta $m_\phi = 165$ GeV ($m_\phi = 223$ GeV) para modelos escalares (pseudoescalares), siendo el límite más restrictivo a baja masa ($\lesssim 100$ GeV) dado por CMS para modelos de DM con mediadores de espín cero. La mejor contribución del canal dileptónico tiene lugar en la región de baja masa para modelos escalares, siendo allí incluso mejor que el canal semileptónico.

Merece la pena señalar una última vez cuáles son las ventajas y los inconvenientes de la búsqueda $t\bar{t}(2\ell)$+DM con respecto a los otros dos canales: Por un lado, la fracción de desintegración del canal $t\bar{t} \to 2\ell$ es la más baja: $^1/_9$ versus $^4/_9$ tanto para el canal semileptónico como para el hadrónico. Así mismo, una parte de la información de la desintegración $t\bar{t}(2\ell)$+DM se pierde debido a la aparición de los dos neutrinos. Pero por otro lado, los leptones se identifican de un modo mucho más limpio y eficiente que los jets de hadrones, lo que permite determinar con relativa seguridad los fondos y evitar incertidumbres grandes. Así, proseguir en un futuro con el estudio del caso $t\bar{t}(2\ell)$+DM puede no resultar crucial, pero sí será bastante útil. Además, se encarece la reconstrucción del $\vec{p}_\mathrm{T}^{\mathrm{DM}}$, analizando en profundidad las dependencias que manifiestan los procesos $t\bar{t}$ y $t\bar{t}$+DM respecto a $\vec{E}_\mathrm{T}^{\mathrm{miss}}$.

Appendix A

Impact of the ANN input variables

The objective of this appendix is to evaluate the individual impact of the four variables going into the ANNs: $E_{\mathrm{T}}^{\mathrm{miss}}$, $\Delta\phi_{\ell\ell\,E_{\mathrm{T}}^{\mathrm{miss}}}$, $p_{\mathrm{T}}^{\mathrm{DM}}$ and $M_{\mathrm{T2}}(\ell\ell)$, in terms of the expected upper limits, $\mu_{\mathrm{up,\,exp}}^{95\%}$.

In order to make this study, the analysis has been repeated from the ANNs-training phase by removing each of the four variables one at a time, and the expected upper limit computed without systematics (in order to speed up the process).

The results can be observed in table A.1. According to them, $M_{\mathrm{T2}}(\ell\ell)$ is the variable which has the strongest impact, followed by $E_{\mathrm{T}}^{\mathrm{miss}}$, $p_{\mathrm{T}}^{\mathrm{DM}}$ and $\Delta\phi_{\ell\ell\,E_{\mathrm{T}}^{\mathrm{miss}}}$. One can see how the ANNs are able to gain sensitivity by using $p_{\mathrm{T}}^{\mathrm{DM}}$.

m_ϕ [GeV]	4 variables	w/o $M_{\mathrm{T2}}(\ell\ell)$	w/o $E_{\mathrm{T}}^{\mathrm{miss}}$	w/o $p_{\mathrm{T}}^{\mathrm{DM}}$	w/o $\Delta\phi_{\ell\ell,E_{\mathrm{T}}^{\mathrm{miss}}}$
scalar					
10	0.1636	0.1714	0.1665	0.1655	0.1646
20	0.2568	0.3037	0.2666	0.2666	0.2529
50	0.5020	0.8672	0.5996	0.5820	0.5332
100	0.9727	2.2109	1.1992	1.0195	1.0039
200	2.5625	6.4688	3.0703	2.7422	2.6797
300	5.1094	13.6875	6.4093	5.2344	5.7031
500	22.6875	58.9688	28.6250	23.6875	25.8125
pseudoscalar					
10	0.9492	2.4297	1.1602	1.0117	1.0117
20	0.9492	2.5078	1.1758	1.0977	0.9883
50	1.0508	2.8516	1.2773	1.2148	1.1055
100	1.2461	3.4844	1.5625	1.3789	1.3320
200	2.1328	5.7031	2.6172	2.2734	2.3672
300	3.7969	9.9063	4.5781	4.3594	4.1406
500	21.4375	56.2500	25.9063	25.6250	23.6875

Table A.1: Expected upper limits, $\mu_{\mathrm{up,exp}}^{95\%}$, obtained by removing each time an input variable of the analysis.

Appendix B

Pulls and impacts plots

This appendix gathers together the pulls and impacts plots for the fourteen signal points. As stated in chapter 7, the "pull" is helpful to evaluate the quality of the a priori systematic estimation, whereas the "impact" measures the influence of the systematic on the signal strength result, which can be used to set a hierarchy of the systematic effects. One can observe how the statistical uncertainty on the most signal-like bin is the leading one in almost all the cases.
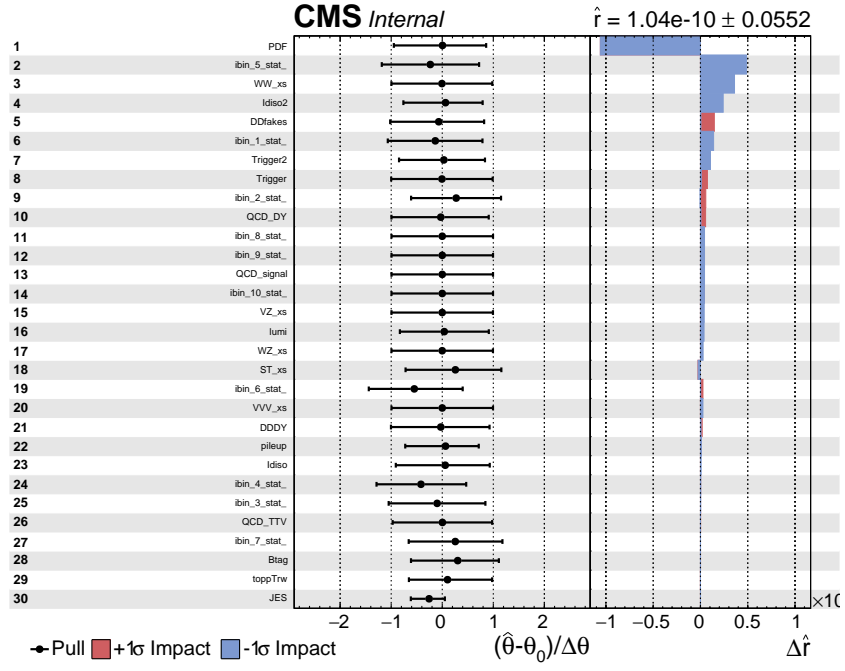
(a) $m_\phi = 10$ GeV
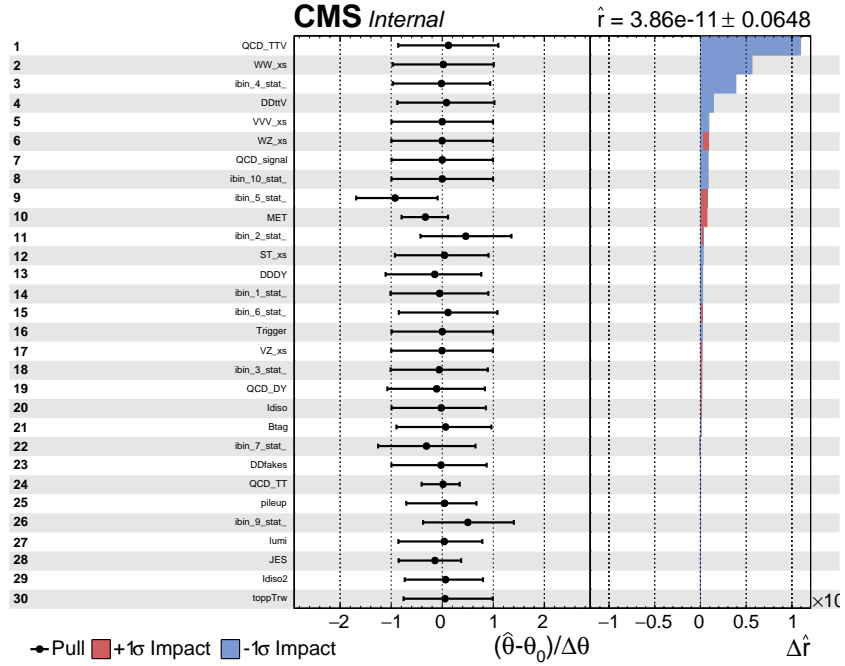
(b) $m_\phi = 20$ GeV

Figure B.1: Pulls (center) and impacts (right) for different scalar models. Nuisances are identified by their datacard names (left).
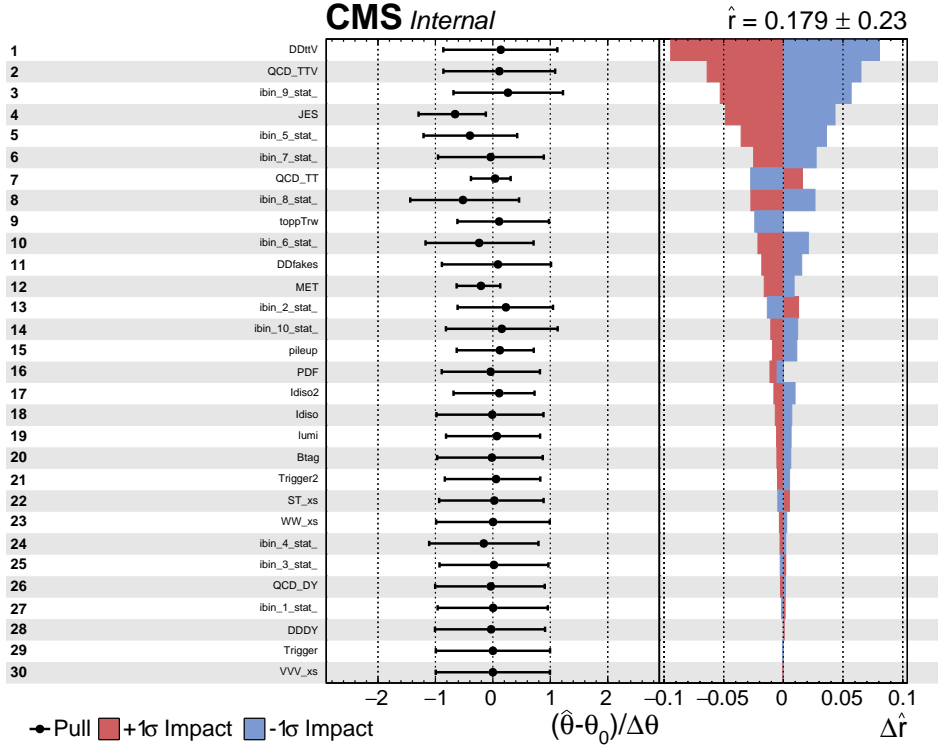
(c) $m_\phi = 50$ GeV
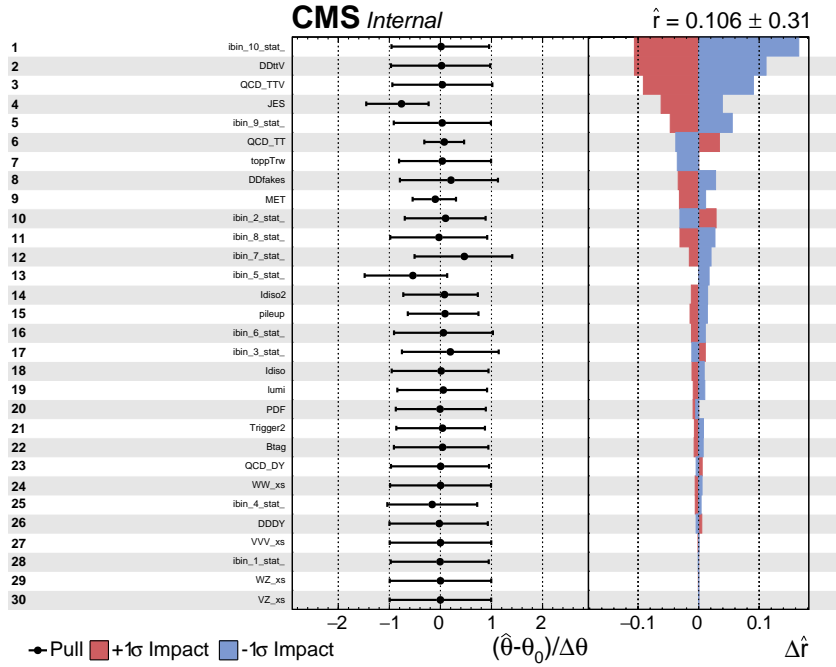
(d) $m_\phi = 100$ GeV

Figure B.1: Pulls (center) and impacts (right) for different scalar models. Nuisances are identified by their datacard names (left) (cont.)
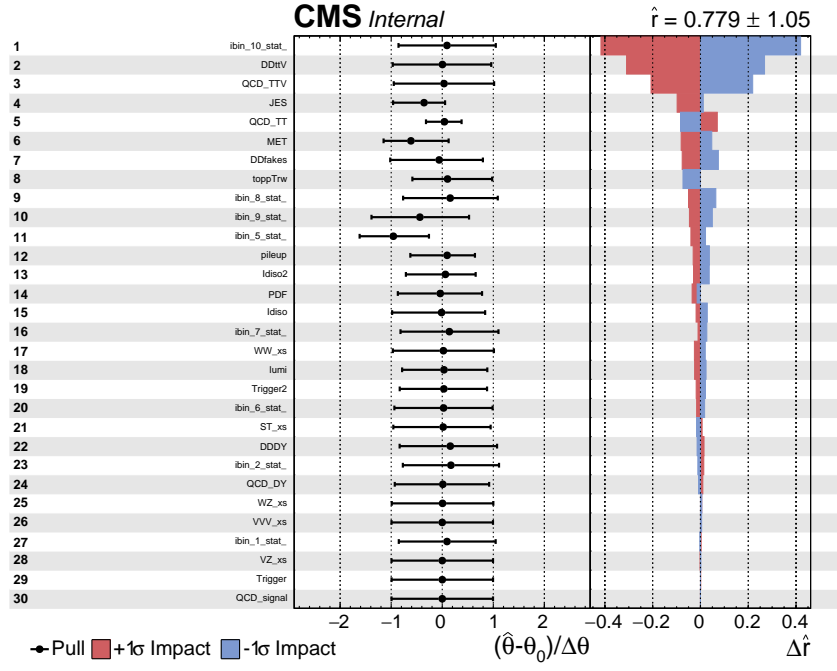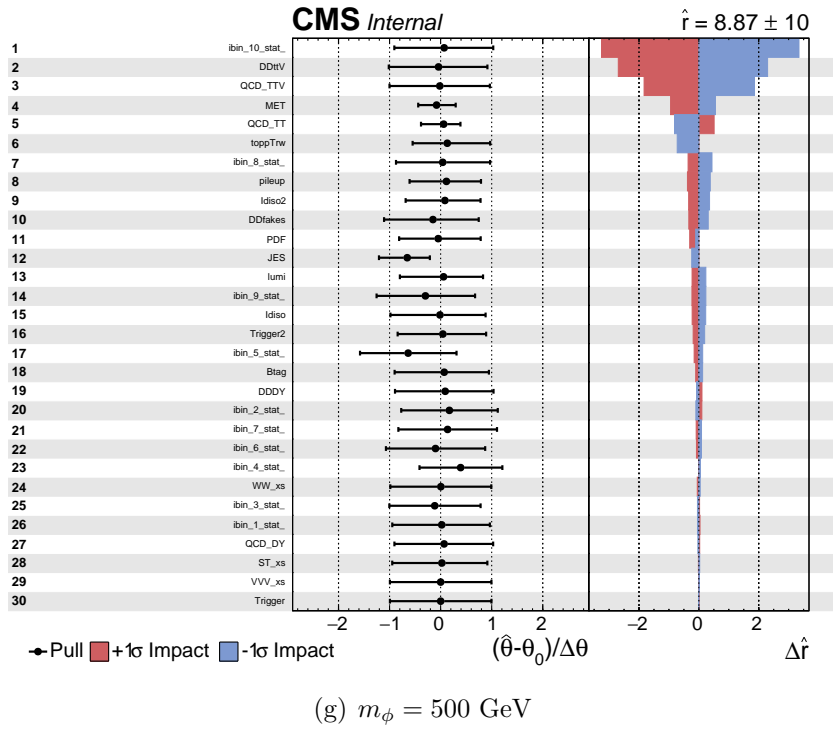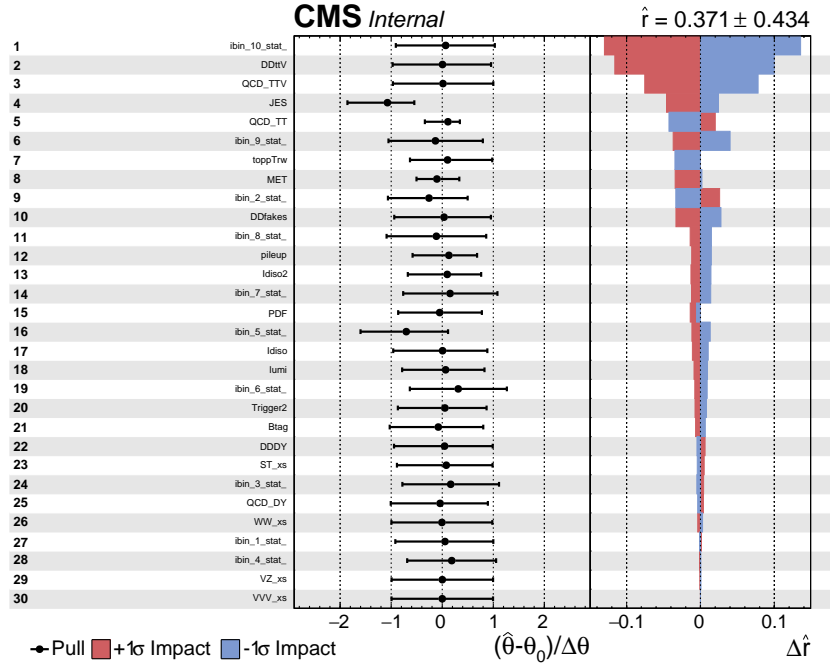
(e) $m_\phi = 200$ GeV
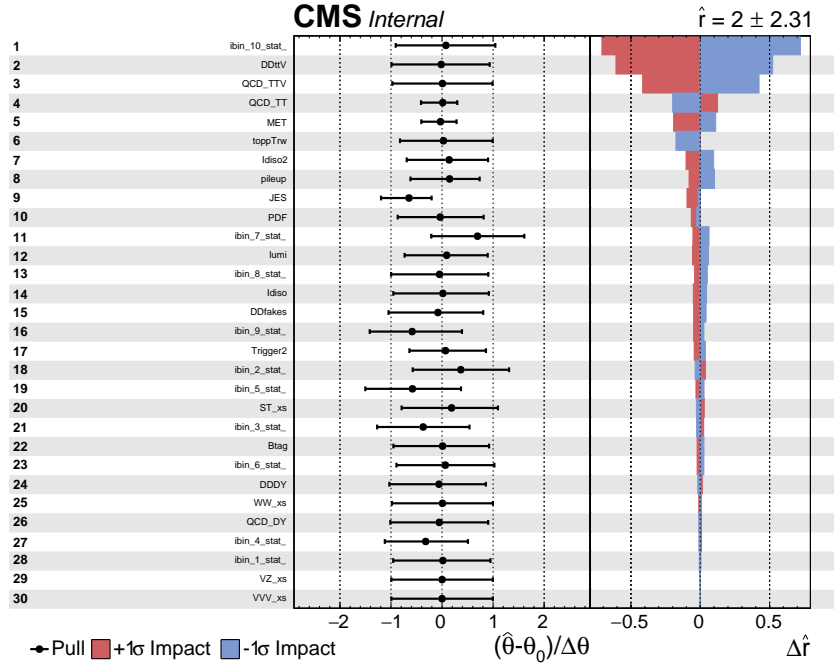
(f) $m_\phi = 300$ GeV

Figure B.1: Pulls (center) and impacts (right) for different scalar models. Nuisances are identified by their datacard names (left) (cont.)
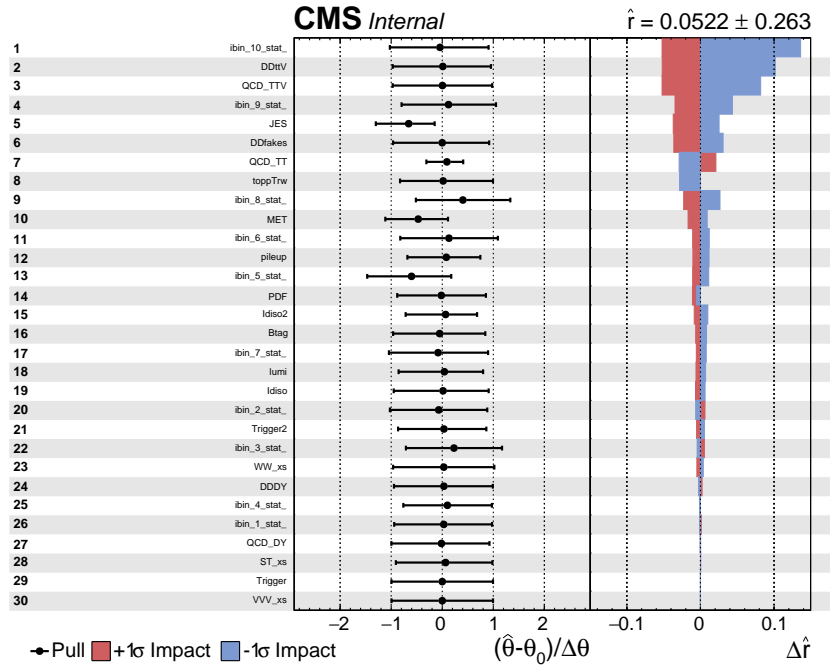
(g) $m_\phi = 500$ GeV

Figure B.1: Pulls (center) and impacts (right) for different scalar models. Nuisances are identified by their datacard names (left) (cont.)

(a) $m_\phi = 10$ GeV

(b) $m_\phi = 20$ GeV

Figure B.2: Pulls (center) and impacts (right) for different pseudoscalar models. Nuisances are identified by their datacard names (left).
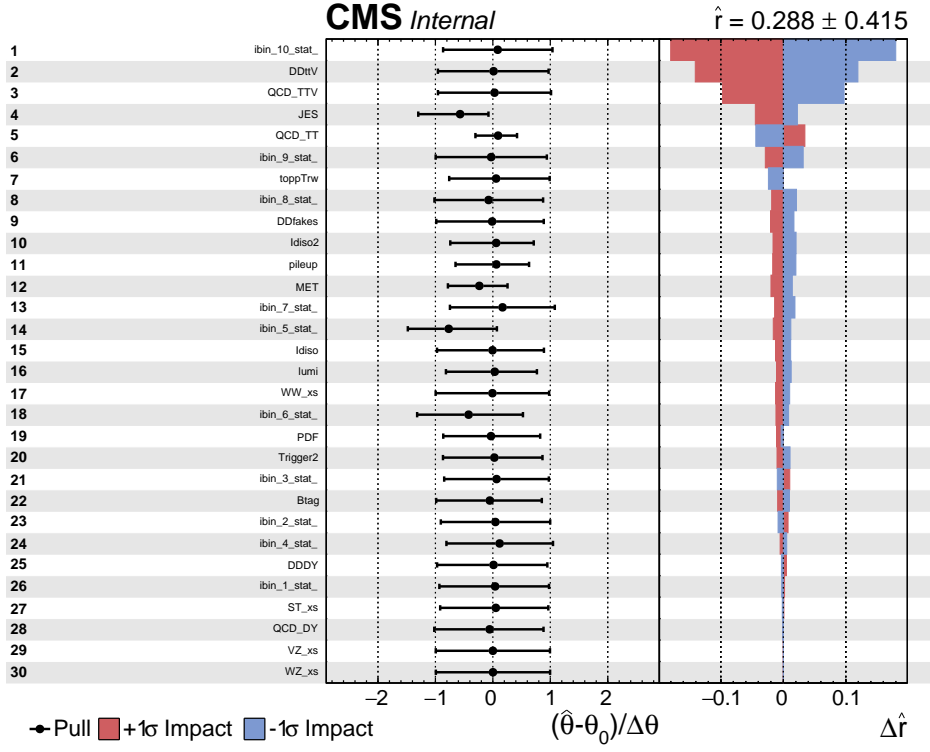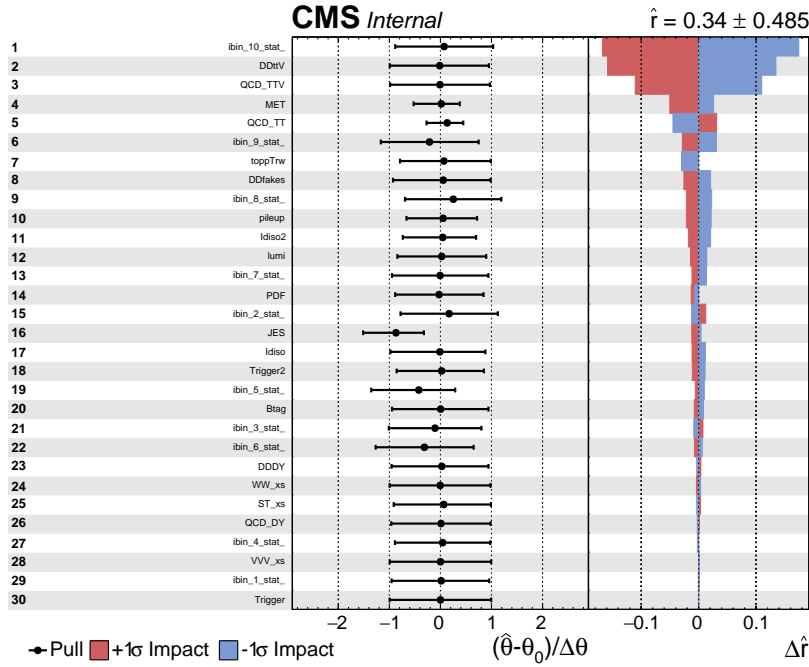
(c) $m_\phi = 50$ GeV

(d) $m_\phi = 100$ GeV

Figure B.2: Pulls (center) and impacts (right) for different pseudoscalar models. Nuisances are identified by their datacard names (left) (cont.)

(e) $m_\phi = 200$ GeV

(f) $m_\phi = 300$ GeV

Figure B.2: Pulls (center) and impacts (right) for different pseudoscalar models. Nuisances are identified by their datacard names (left) (cont.)
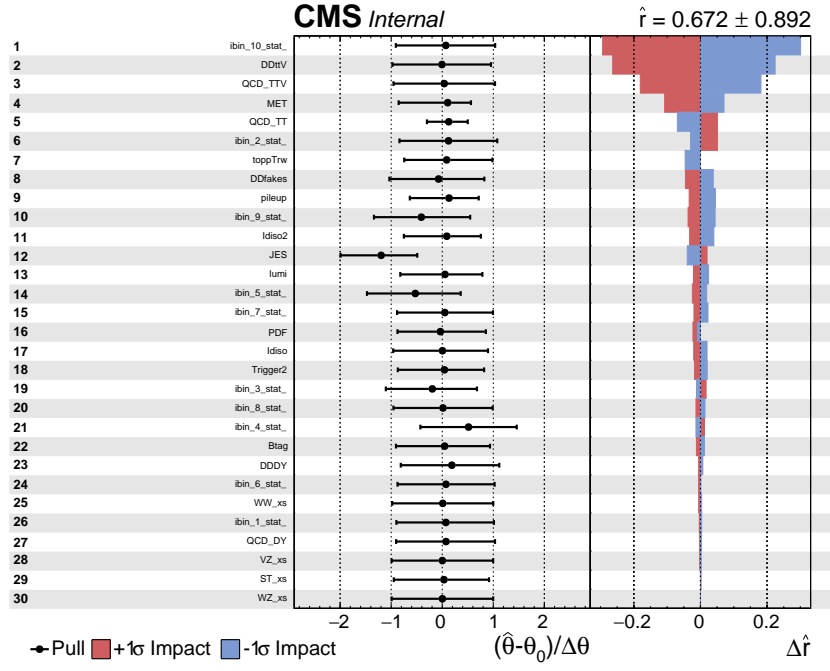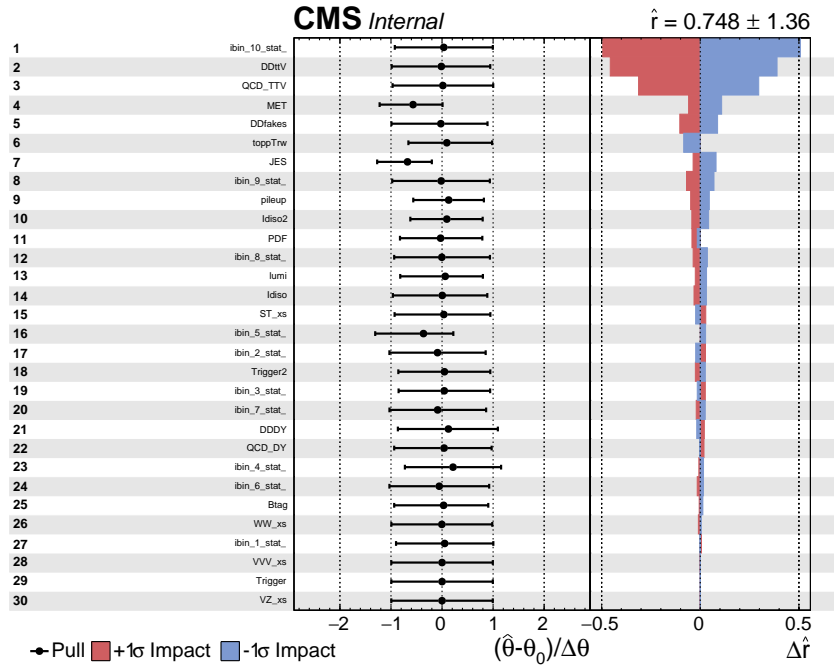
(g) $m_\phi = 500$ GeV

Figure B.2: Pulls (center) and impacts (right) for different pseudoscalar models. Nuisances are identified by their datacard names (left) (cont.)
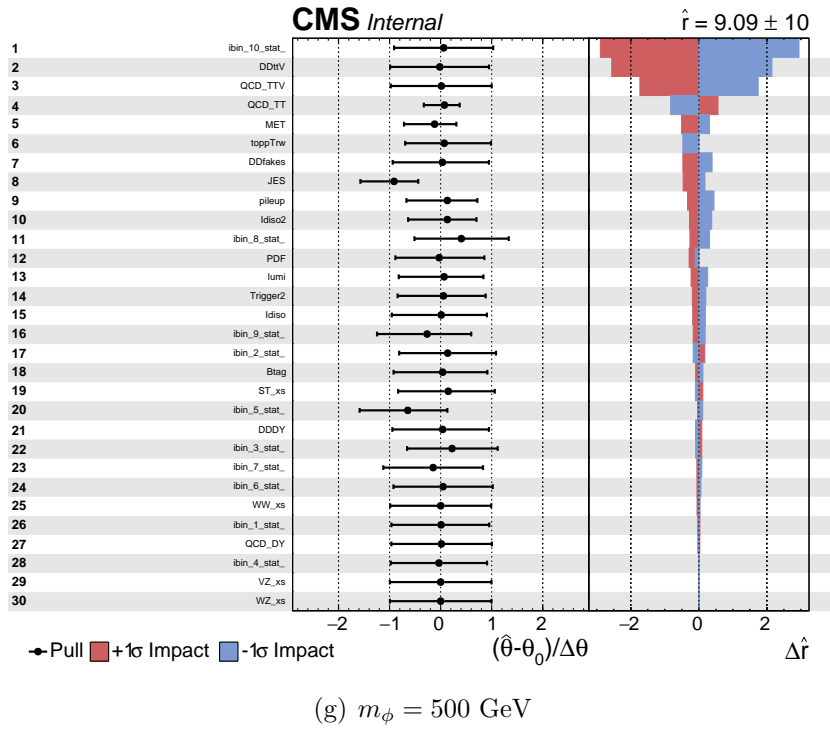
Bibliography

[1] C. Collaboration, "Search for the Production of Dark Matter in Association with Top Quark Pairs in the Di-lepton Final State in pp collisions at $\sqrt{s} = 8$ TeV," 2014.

[2] V. Khachatryan *et al.*, "Search for the production of dark matter in association with top-quark pairs in the single-lepton final state in proton-proton collisions at sqrt(s) = 8 TeV," *JHEP*, vol. 06, p. 121, 2015.

[3] "Search for direct top squark pair production and dark matter production in final states with two leptons in $\sqrt{s} = 13$ TeV *pp* collisions using 13.3 fb^{-1} of ATLAS data," Tech. Rep. ATLAS-CONF-2016-076, CERN, Geneva, Aug 2016.

[4] "Search for top squarks in final states with one isolated lepton, jets, and missing transverse momentum in $\sqrt{s} = 13$ TeV pp collisions with the ATLAS detector," Tech. Rep. ATLAS-CONF-2016-050, CERN, Geneva, Aug 2016.

[5] "Search for the Supersymmetric Partner of the Top Quark in the Jets+Emiss Final State at sqrt(s) = 13 TeV," Tech. Rep. ATLAS-CONF-2016-077, CERN, Geneva, Aug 2016.

[6] M. Aaboud *et al.*, "Search for dark matter produced in association with bottom or top quarks in $\sqrt{s} = 13$ TeV pp collisions with the ATLAS detector," *Eur. Phys. J.*, vol. C78, no. 1, p. 18, 2018.

[7] A. M. Sirunyan *et al.*, "Search for dark matter produced in association with heavy-flavor quark pairs in proton-proton collisions at $\sqrt{s} = 13$ TeV," *Eur. Phys. J.*, vol. C77, no. 12, p. 845, 2017.

[8] "Search for dark matter in association with a $t\bar{t}$ pair at $\sqrt{s} = 13$ TeV in the dilepton channel with 2016 data," Tech. Rep. CMS-PAS-EXO-17-014, CERN, Geneva, 2018.

[9] J. Silk *et al.*, *Particle Dark Matter: Observations, Models and Searches.* Cambridge: Cambridge Univ. Press, 2010.

[10] E. W. Kolb and M. S. Turner, "The Early Universe," *Front. Phys.*, vol. 69, pp. 1–547, 1990.

[11] E. Gildener, "Gauge-symmetry hierarchies," *Phys. Rev. D*, vol. 14, pp. 1667–1672, Sep 1976.

[12] G. Aad *et al.*, "Observation of a new particle in the search for the Standard Model Higgs boson with the ATLAS detector at the LHC," *Phys. Lett.*, vol. B716, pp. 1–29, 2012.

[13] S. Chatrchyan *et al.*, "Observation of a new boson at a mass of 125 GeV with the CMS experiment at the LHC," *Phys. Lett.*, vol. B716, pp. 30–61, 2012.

[14] G. Jungman, M. Kamionkowski, and K. Griest, "Supersymmetric dark matter," *Phys. Rept.*, vol. 267, pp. 195–373, 1996.

[15] J. Abdallah *et al.*, "Simplified Models for Dark Matter Searches at the LHC," *Phys. Dark Univ.*, vol. 9-10, pp. 8–23, 2015.

[16] G. D'Ambrosio, G. F. Giudice, G. Isidori, and A. Strumia, "Minimal flavor violation: An Effective field theory approach," *Nucl. Phys.*, vol. B645, pp. 155–187, 2002.

[17] L. Sonnenschein, "Analytical solution of ttbar dilepton equations," *Phys. Rev.*, vol. D73, p. 054015, 2006. [Erratum: Phys. Rev.D78,079902(2008)].

[18] M. Milgrom, "A Modification of the Newtonian dynamics as a possible alternative to the hidden mass hypothesis," *Astrophys. J.*, vol. 270, pp. 365–370, 1983.

[19] M. Milgrom, "A Modification of the Newtonian dynamics: Implications for galaxies," *Astrophys. J.*, vol. 270, pp. 371–383, 1983.

[20] V. C. Rubin and W. K. Ford, Jr., "Rotation of the Andromeda Nebula from a Spectroscopic Survey of Emission Regions," *Astrophys. J.*, vol. 159, pp. 379–403, 1970.

[21] M. S. Roberts and A. H. Rots, "Comparison of Rotation Curves of Different Galaxy Types," *Astron. Astrophys.*, vol. 26, pp. 483–485, 1973.

[22] H. Goldstein, C. P. Poole, and J. L. Safko, *Classical Mechanics*. Addison Wesley, 2002.

[23] F. Zwicky, "On the Masses of Nebulae and of Clusters of Nebulae," *Astrophys. J.*, vol. 86, pp. 217–246, 1937.

[24] D. Clowe, A. Gonzalez, and M. Markevitch, "Weak lensing mass reconstruction of the interacting cluster 1E0657-558: Direct evidence for the existence of dark matter," *Astrophys. J.*, vol. 604, pp. 596–603, 2004.

[25] D. Clowe, M. Bradac, A. H. Gonzalez, M. Markevitch, S. W. Randall, C. Jones, and D. Zaritsky, "A direct empirical proof of the existence of dark matter," *Astrophys. J.*, vol. 648, pp. L109–L113, 2006.

[26] V. Springel *et al.*, "Simulating the joint evolution of quasars, galaxies and their large-scale distribution," *Nature*, vol. 435, pp. 629–636, 2005.

[27] P. A. R. Ade *et al.*, "Planck 2015 results. XIII. Cosmological parameters," *Astron. Astrophys.*, vol. 594, p. A13, 2016.

[28] C. Patrignani *et al.*, "Review of Particle Physics," *Chin. Phys.*, vol. C40, no. 10, p. 100001, 2016.

[29] R. Dave, D. N. Spergel, P. J. Steinhardt, and B. D. Wandelt, "Halo properties in cosmological simulations of selfinteracting cold dark matter," *Astrophys. J.*, vol. 547, pp. 574–589, 2001.

[30] J. L. Feng and J. Kumar, "The WIMPless Miracle: Dark-Matter Particles without Weak-Scale Masses or Weak Interactions," *Phys. Rev. Lett.*, vol. 101, p. 231301, 2008.

[31] S. Weinberg, "A New Light Boson?," *Phys. Rev. Lett.*, vol. 40, pp. 223–226, 1978.

[32] F. Wilczek, "Problem of Strong p and t Invariance in the Presence of Instantons," *Phys. Rev. Lett.*, vol. 40, pp. 279–282, 1978.

[33] K. N. Abazajian, "Sterile neutrinos in cosmology," *Phys. Rept.*, vol. 711-712, pp. 1–28, 2017.

[34] J. L. Feng, A. Rajaraman, and F. Takayama, "Superweakly interacting massive particles," *Phys. Rev. Lett.*, vol. 91, p. 011302, 2003.

[35] L. J. Hall, K. Jedamzik, J. March-Russell, and S. M. West, "Freeze-In Production of FIMP Dark Matter," *JHEP*, vol. 03, p. 080, 2010.

[36] N. Arkani-Hamed, S. Dimopoulos, and G. R. Dvali, "The Hierarchy problem and new dimensions at a millimeter," *Phys. Lett.*, vol. B429, pp. 263–272, 1998.

[37] L. Randall and R. Sundrum, "A Large mass hierarchy from a small extra dimension," *Phys. Rev. Lett.*, vol. 83, pp. 3370–3373, 1999.

[38] N. Arkani-Hamed, A. G. Cohen, and H. Georgi, "Electroweak symmetry breaking from dimensional deconstruction," *Phys. Lett.*, vol. B513, pp. 232–240, 2001.

[39] R. Contino, "The Higgs as a Composite Nambu-Goldstone Boson," in *Physics of the large and the small, TASI 09, proceedings of the Theoretical Advanced Study Institute in Elementary Particle Physics, Boulder, Colorado, USA, 1-26 June 2009*, pp. 235–306, 2011.

[40] Z. Chacko, H.-S. Goh, and R. Harnik, "The Twin Higgs: Natural electroweak breaking from mirror symmetry," *Phys. Rev. Lett.*, vol. 96, p. 231802, 2006.

[41] I. García García, R. Lasenby, and J. March-Russell, "Twin higgs wimp dark matter," *Phys. Rev. D*, vol. 92, p. 055034, Sep 2015.

[42] T. R. Slatyer, "TASI Lectures on Indirect Detection of Dark Matter," in *Theoretical Advanced Study Institute in Elementary Particle Physics: Anticipating the Next Discoveries in Particle Physics (TASI 2016) Boulder, CO, USA, June 6-July 1, 2016*, 2017.

[43] E. Charles *et al.*, "Sensitivity Projections for Dark Matter Searches with the Fermi Large Area Telescope," *Phys. Rept.*, vol. 636, pp. 1–46, 2016.

[44] M. G. Aartsen *et al.*, "Search for Neutrinos from Dark Matter Self-Annihilations in the center of the Milky Way with 3 years of Ice-Cube/DeepCore," *Eur. Phys. J.*, vol. C77, no. 9, p. 627, 2017.

[45] M. Aguilar *et al.*, "Antiproton Flux, Antiproton-to-Proton Flux Ratio, and Properties of Elementary Particle Fluxes in Primary Cosmic Rays Measured with the Alpha Magnetic Spectrometer on the International Space Station," *Phys. Rev. Lett.*, vol. 117, no. 9, p. 091103, 2016.

[46] E. Aprile *et al.*, "First Dark Matter Search Results from the XENON1T Experiment," *Phys. Rev. Lett.*, vol. 119, no. 18, p. 181301, 2017.

[47] C. Fu *et al.*, "Spin-Dependent Weakly-Interacting-Massive-Particle–Nucleon Cross Section Limits from First Data of PandaX-II Experiment," *Phys. Rev. Lett.*, vol. 118, no. 7, p. 071301, 2017. [Erratum: Phys. Rev. Lett.120,no.4,049902(2018)].

[48] D. S. Akerib *et al.*, "Results from a search for dark matter in the complete LUX exposure," *Phys. Rev. Lett.*, vol. 118, no. 2, p. 021303, 2017.

[49] P. Agnes *et al.*, "Low-mass Dark Matter Search with the DarkSide-50 Experiment," 2018.

[50] P. Agnes *et al.*, "DarkSide-50 532-day Dark Matter Search with Low-Radioactivity Argon," 2018.

[51] P. A. Amaudruz *et al.*, "First results from the DEAP-3600 dark matter search with argon at SNOLAB," 2017.

[52] T. Aaltonen *et al.*, "A Search for dark matter in events with one jet and missing transverse energy in $p\bar{p}$ collisions at $\sqrt{s} = 1.96$ TeV," *Phys. Rev. Lett.*, vol. 108, p. 211804, 2012.

[53] V. Khachatryan *et al.*, "Search for dark matter, extra dimensions, and unparticles in monojet events in proton–proton collisions at $\sqrt{s} = 8$ TeV," *Eur. Phys. J.*, vol. C75, no. 5, p. 235, 2015.

[54] G. Aad *et al.*, "Search for dark matter in events with heavy quarks and missing transverse momentum in pp collisions with the ATLAS detector," *Eur. Phys. J.*, vol. C75, no. 2, p. 92, 2015.

[55] S. A. Malik *et al.*, "Interplay and Characterization of Dark Matter Searches at Colliders and in Direct Detection Experiments," *Phys. Dark Univ.*, vol. 9-10, pp. 51–58, 2015.

[56] G. Busoni, A. De Simone, E. Morgante, and A. Riotto, "On the Validity of the Effective Field Theory for Dark Matter Searches at the LHC," *Phys. Lett.*, vol. B728, pp. 412–421, 2014.

[57] O. Buchmueller, M. J. Dolan, and C. McCabe, "Beyond Effective Field Theory for Dark Matter Searches at the LHC," *JHEP*, vol. 01, p. 025, 2014.

[58] D. Alves, "Simplified Models for LHC New Physics Searches," *J. Phys.*, vol. G39, p. 105005, 2012.

[59] J. Abdallah *et al.*, "Simplified Models for Dark Matter and Missing Energy Searches at the LHC," 2014.

[60] S. Chatrchyan *et al.*, "Study of the Mass and Spin-Parity of the Higgs Boson Candidate Via Its Decays to Z Boson Pairs," *Phys. Rev. Lett.*, vol. 110, no. 8, p. 081803, 2013.

[61] G. Aad *et al.*, "Study of the spin and parity of the Higgs boson in diboson decays with the ATLAS detector," *Eur. Phys. J.*, vol. C75, no. 10, p. 476, 2015. [Erratum: Eur. Phys. J.C76,no.3,152(2016)].

[62] D. Abercrombie *et al.*, "Dark Matter Benchmark Models for Early LHC Run-2 Searches: Report of the ATLAS/CMS Dark Matter Forum," 2015.

[63] M. R. Buckley, D. Feld, and D. Goncalves, "Scalar Simplified Models for Dark Matter," *Phys. Rev.*, vol. D91, p. 015017, 2015.

[64] J. J. Thomson, "Cathode Rays," *Philosophical Magazine*, vol. 44, no. 269, pp. 293–316, 1897.

[65] H. Becquerel, "On the rays emitted by phosphorescence," *Compt. Rend. Hebd. Seances Acad. Sci.*, vol. 122, no. 8, pp. 420–421, 1896.

[66] V. F. Hess, "Über Beobachtungen der durchdringenden Strahlung bei sieben Freiballonfahrten," *Z. Phys.*, vol. 13, p. 1084, 1912.

[67] O. S. Brüning, P. Collier, P. Lebrun, S. Myers, R. Ostojic, J. Poole, and P. Proudlock, *LHC Design Report.* CERN Yellow Reports: Monographs, Geneva: CERN, 2004.

[68] R. Assmann, M. Lamont, and S. Myers, "A brief history of the LEP collider," *Nucl. Phys. Proc. Suppl.*, vol. 109B, pp. 17–31, 2002. [,17(2002)].

[69] F. Englert and R. Brout, "Broken symmetry and the mass of gauge vector mesons," *Phys. Rev. Lett.*, vol. 13, pp. 321–323, Aug 1964.

[70] P. W. Higgs, "Broken symmetries and the masses of gauge bosons," *Phys. Rev. Lett.*, vol. 13, pp. 508–509, Oct 1964.

[71] G. S. Guralnik, C. R. Hagen, and T. W. B. Kibble, "Global conservation laws and massless particles," *Phys. Rev. Lett.*, vol. 13, pp. 585–587, Nov 1964.

[72] S. Weinberg, "A model of leptons," *Phys. Rev. Lett.*, vol. 19, pp. 1264–1266, Nov 1967.

[73] G. 't Hooft, "Renormalizable Lagrangians for Massive Yang-Mills Fields," *Nucl. Phys.*, vol. B35, pp. 167–188, 1971.

[74] R. Barate *et al.*, "Search for the standard model Higgs boson at LEP," *Phys. Lett.*, vol. B565, pp. 61–75, 2003.

[75] A. M. Sirunyan *et al.*, "Evidence for the Higgs boson decay to a bottom quark-antiquark pair," 2017.

[76] "Evidence for the $H \rightarrow b\bar{b}$ decay with the ATLAS detector," Tech. Rep. ATLAS-CONF-2017-041, CERN, Geneva, Jul 2017.

[77] S. Chatrchyan *et al.*, "The CMS Experiment at the CERN LHC," *JINST*, vol. 3, p. S08004, 2008.

[78] S. Chatrchyan *et al.*, "Precise Mapping of the Magnetic Field in the CMS Barrel Yoke using Cosmic Rays," *JINST*, vol. 5, p. T03021, 2010.

[79] A. M. Sirunyan *et al.*, "Performance of the CMS muon detector and muon reconstruction with proton-proton collisions at $\sqrt{s} = 13$ TeV," 2018.

[80] G. L. Bayatyan *et al.*, *CMS TriDAS project: Technical Design Report, Volume 1: The Trigger Systems*. Technical Design Report CMS.

[81] S. Cittolin, A. Rácz, and P. Sphicas, *CMS The TriDAS Project: Technical Design Report, Volume 2: Data Acquisition and High-Level Trigger. CMS trigger and data-acquisition project*. Technical Design Report CMS, Geneva: CERN, 2002.

[82] `https://twiki.cern.ch/twiki/bin/view/CMSPublic/LumiPublicResults#2016_proton_proton_13_TeV_collis`.

[83] S. Chatrchyan *et al.*, "Description and performance of track and primary-vertex reconstruction with the CMS tracker," *JINST*, vol. 9, no. 10, p. P10009, 2014.

[84] A. M. Sirunyan *et al.*, "Particle-flow reconstruction and global event description with the CMS detector," *JINST*, vol. 12, no. 10, p. P10003, 2017.

[85] V. Khachatryan *et al.*, "Performance of Electron Reconstruction and Selection with the CMS Detector in Proton-Proton Collisions at $\sqrt{s} = 8$ TeV," *JINST*, vol. 10, no. 06, p. P06005, 2015.

[86] M. Cacciari, G. P. Salam, and G. Soyez, "The Anti-k(t) jet clustering algorithm," *JHEP*, vol. 04, p. 063, 2008.

[87] A. M. Sirunyan *et al.*, "Identification of heavy-flavour jets with the CMS detector in pp collisions at 13 TeV," 2017.

[88] P. Elmer, B. Hegner, and L. Sexton-Kennedy, "Experience with the CMS Event Data Model," *J. Phys. Conf. Ser.*, vol. 219, p. 032022, 2010.

[89] G. Petrucciani, A. Rizzi, and C. Vuosalo, "Mini-AOD: A New Analysis Data Format for CMS," *J. Phys. Conf. Ser.*, vol. 664, no. 7, p. 072052, 2015.

[90] R. Brun and F. Rademakers, "ROOT: An object oriented data analysis framework," *Nucl. Instrum. Meth.*, vol. A389, pp. 81–86, 1997.

[91] JSON file: `/afs/cern.ch/cms/CAF/CMSCOMM/COMM_DQM/certification/Collisions16/13TeV/ReReco/Final/Cert_271036-284044_13TeV_23Sep2016ReReco_Collisions16_JSON.txt`.

[92] "CMS Luminosity Measurements for the 2016 Data Taking Period," Tech. Rep. CMS-PAS-LUM-17-001, CERN, Geneva, 2017.

[93] S. Alioli *et al.*, "A general framework for implementing NLO calculations in shower Monte Carlo programs: the POWHEG BOX," *JHEP*, vol. 06, p. 043, 2010.

[94] R. D. Ball *et al.*, "Parton distributions for the LHC Run II," *JHEP*, vol. 04, p. 040, 2015.

[95] T. Sjostrand, S. Mrenna, and P. Z. Skands, "PYTHIA 6.4 Physics and Manual," *JHEP*, vol. 05, p. 026, 2006.

[96] T. Sjostrand, S. Ask, J. R. Christiansen, R. Corke, N. Desai, P. Ilten, S. Mrenna, S. Prestel, C. O. Rasmussen, and P. Z. Skands, "An Introduction to PYTHIA 8.2," *Comput. Phys. Commun.*, vol. 191, pp. 159–177, 2015.

[97] "Investigations of the impact of the parton shower tuning in Pythia 8 in the modelling of $t\bar{t}$ at $\sqrt{s} = 8$ and 13 TeV," Tech. Rep. CMS-PAS-TOP-16-021, CERN, Geneva, 2016.

[98] E. Re, "Single-top Wt-channel production matched with parton showers using the POWHEG method," *Eur. Phys. J. C*, vol. 71, p. 1547, 2011.

[99] "Underlying Event Tunes and Double Parton Scattering," Tech. Rep. CMS-PAS-GEN-14-001, CERN, Geneva, 2014.

[100] P. Skands, S. Carrazza, and J. Rojo, "Tuning PYTHIA 8.1: the Monash 2013 Tune," *Eur. Phys. J.*, vol. C74, no. 8, p. 3024, 2014.

[101] J. Alwall, R. Frederix, S. Frixione, V. Hirschi, F. Maltoni, O. Mattelaer, H. S. Shao, T. Stelzer, P. Torrielli, and M. Zaro, "The automated computation of tree-level and next-to-leading order differential cross sections, and their matching to parton shower simulations," *JHEP*, vol. 07, p. 079, 2014.

[102] R. Frederix and S. Frixione, "Merging meets matching in MC@NLO," *JHEP*, vol. 12, p. 061, 2012.

[103] H. Bakhshian et al., "Computing the contamination from fakes in leptonic final states," *CMS Physics Analysis Note*, vol. CMS-AN-10-261, 2010.

[104] N. Kidonakis, "Two-loop soft anomalous dimensions for single top quark associated production with W^- or H^-," *Phys. Rev. D*, vol. 82, p. 054018, 2010.

[105] J. M. Campbell, R. K. Ellis, and C. Williams, "Vector boson pair production at the LHC," *JHEP*, vol. 07, p. 018, 2011.

[106] M. Czakon and A. Mitov, "Top++: A Program for the Calculation of the Top-Pair Cross-Section at Hadron Colliders," *Comput.Phys.Commun.*, vol. 185, p. 2930, 2014.

[107] S. Alekhin *et al.*, "The PDF4LHC Working Group Interim Report," 2011.

[108] M. Botje *et al.*, "The PDF4LHC Working Group Interim Recommendations," 2011.

[109] A. D. Martin, W. J. Stirling, R. S. Thorne, and G. Watt, "Parton distributions for the LHC," *Eur. Phys. J. C*, vol. 63, p. 189, 2009.

[110] H.-L. Lai, M. Guzzi, J. Huston, Z. Li, P. M. Nadolsky, J. Pumplin, and C.-P. Yuan, "New parton distributions for collider physics," *Phys. Rev. D*, vol. 82, p. 074024, 2010.

[111] J. Gao, M. Guzzi, J. Huston, H.-L. Lai, Z. Li, P. Nadolsky, J. Pumplin, D. Stump, and C. P. Yuan, "CT10 next-to-next-to-leading order global analysis of QCD," *Phys. Rev.*, vol. D89, no. 3, p. 033009, 2014.

[112] R. D. Ball, S. C. Valerio Bertone andf, C. S. Deans, L. D. Debbio, S. Forte, A. Guffanti, N. P. Hartland, J. I. Latorre, J. Rojo, and M. Ubiali, "Parton distributions with LHC data," *Nucl. Phys. B*, vol. 867, p. 244, 2013.

[113] GEANT4 Collaboration, S. Agostinelli et al., "GEANT4: A simulation toolkit," *Nucl. Instrum. Meth.*, vol. A506, p. 250, 2003.

[114] `https://twiki.cern.ch/twiki/bin/viewauth/CMS/PileupJSONFileforData`.

[115] CMS Collaboration, "Common analysis object definitions and trigger efficiencies for the H*to*WW analysis with 2015 and 2016 full data," CMS AN CMS-AN-17-082, CMS, 2017.

[116] `https://twiki.cern.ch/twiki/bin/viewauth/CMS/BtagRecommendation80XReReco`.

[117] https://twiki.cern.ch/twiki/bin/view/CMS/JECDataMC.

[118] https://twiki.cern.ch/twiki/bin/viewauth/CMS/
      TopPtReweighting.

[119] https://twiki.cern.ch/twiki/bin/view/CMS/MuonPOG.

[120] https://twiki.cern.ch/twiki/bin/viewauth/CMS/EgammaPOG.

[121] https://twiki.cern.ch/twiki/bin/view/CMS/
      JetID13TeVRun2016.

[122] https://twiki.cern.ch/twiki/bin/view/CMS/
      MissingETOptionalFiltersRun2.

[123] "Measurement of the Top Quark Mass in Dilepton ttbar Decays at
      sqrt(s) = 8 TeV," Tech. Rep. CMS-PAS-TOP-14-010, CERN, Geneva,
      2014.

[124] A. Abulencia *et al.*, "Measurement of the top quark mass using tem-
      plate methods on dilepton events in proton antiproton collisions at
      $\sqrt{s} = 1.96$-TeV.," *Phys. Rev.*, vol. D73, p. 112006, 2006.

[125] C. G. Lester and D. J. Summers, "Measuring masses of semiinvisi-
      bly decaying particles pair produced at hadron colliders," *Phys. Lett.*,
      vol. B463, pp. 99–103, 1999.

[126] A. Höcker, J. Stelzer, F. Tegenfeldt, H. Voss, K. Voss, A. Christov,
      S. Henrot-Versillé, M. Jachowski, A. Krasznahorkay, Y. Mahalalel,
      X. Prudent, and P. Speckmayer, "TMVA - Toolkit for Multivariate
      Data Analysis with ROOT: Users guide," Tech. Rep. CERN-OPEN-
      2007-007, CERN, Geneva, Mar 2007.

[127] S. Ramón y Cajal, *Histologie du système nerveux de l'homme & des
      vertébrés.* 1911.

[128] G. Cowan, K. Cranmer, E. Gross, and O. Vitells, "Asymptotic formulae
      for likelihood-based tests of new physics," *Eur. Phys. J. C*, vol. 71,
      p. 1554, 2011. [Erratum: *Eur. Phys. J. C* **73** (2013) 2501].

[129] ATLAS and CMS Collaborations, "Procedure for the LHC Higgs boson search combination in summer 2011," Tech. Rep. ATL-PHYS-PUB-2011-011, CMS-NOTE-2011-005, CERN, 2011.

[130] T. Junk, "Confidence level computation for combining searches with small statistics," *Nucl. Instrum. Meth. A*, vol. 434, p. 435, 1999.

[131] A. L. Read, "Presentation of search results: the CL_s technique," *J. Phys. G*, vol. 28, p. 2693, 2002.

[132] R. D. Ball, V. Bertone, S. Carrazza, C. S. Deans, L. Del Debbio, S. Forte, A. Guffanti, N. P. Hartland, J. I. Latorre, J. Rojo, and M. Ubiali, "Parton distributions for the lhc run ii," *Journal of High Energy Physics*, vol. 2015, p. 40, Apr 2015.

[133] J. Butterworth, S. Carrazza, A. Cooper-Sarkar, A. D. Roeck, J. Feltesse, S. Forte, J. Gao, S. Glazov, J. Huston, Z. Kassabov, R. McNulty, A. Morsch, P. Nadolsky, V. Radescu, J. Rojo, and R. Thorne, "Pdf4lhc recommendations for lhc run ii," *Journal of Physics G: Nuclear and Particle Physics*, vol. 43, no. 2, p. 023001, 2016.

[134] `https://twiki.cern.ch/twiki/bin/view/LHCPhysics/SingleTopRefXsec`.

[135] `https://twiki.cern.ch/twiki/bin/view/LHCPhysics/DibosonRefXsec`.

[136] "Identification of b quark jets at the CMS Experiment in the LHC Run 2," Tech. Rep. CMS-PAS-BTV-15-001, CERN, Geneva, 2016.